

POLITECNICO di TORINO

Master's Degree in Civil Engineering

Master Thesis

**Flutter instability of
long-span suspension bridges
The case-study of the
1915Çanakkale Bridge in Turkey**



Supervisors:

Prof. Alberto CARPINTERI

Dr. Gianfranco PIANA

Eng. Sebastiano RUSSO

Candidate:

Luca VAILATI

Academic Year 2022/2023



Ringraziamenti

Porgo i miei più sentiti ringraziamenti all'istituzione Politecnico di Torino ed ai docenti che mi hanno accompagnato durante il corso di studi ed hanno contribuito alla mia crescita personale e professionale arricchendo giorno dopo giorno le mie conoscenze. Un ringraziamento speciale va al Prof. Alberto Carpinteri che ha gentilmente accettato l'incarico di essere il mio relatore di tesi di laurea e che mi ha fatto appassionare al mondo dell'ingegneria strutturale, con le sue criticità e innumerevoli sfide, come quelle riguardanti i ponti sospesi. Un sentito ringraziamento va al Dott. Gianfranco Piana, che ha saputo seguirmi con grande professionalità e disponibilità nel tortuoso percorso della redazione di una tesi di laurea magistrale. Si ringrazia l'Ing. Sebastiano Russo per i preziosi suggerimenti forniti nell'utilizzo del programma di calcolo strutturale ANSYS durante alcune fasi del presente lavoro, e per la bella esperienza del convegno IABSE di Istanbul al quale abbiamo preso parte.

Gran parte del merito per il raggiungimento di questo mio traguardo va a tutta la mia famiglia ed in particolare ai miei genitori, Angelo ed Elena, e a mia sorella, Susanna, che mi hanno sempre aiutato e sostenuto nei momenti di difficoltà e hanno gioito con me per i traguardi raggiunti.

Un grazie speciale a Lucia, la persona che ho conosciuto in questa università e che è stata capace di comprendermi, conoscermi e sostenermi in questo percorso e ha saputo regalarmi momenti di grande felicità in questi anni.

Voglio ringraziare i miei colleghi e amici, in particolare Elias e Francesca, con cui ho condiviso giorni di lavoro e fatica sui progetti e lezioni, e fantastici momenti di condivisione, vacanze e svago insieme.

Infine, ringrazio di cuore nonno Filippo e nonna Maria Rosa, che oggi non può essere qui con me.

Vi dedico questa tesi per il vostro sostegno e per aver sempre creduto in me e nel mio obiettivo di diventare un giorno Ingegnere Civile.

“Gutta cavat lapidem, non vi sed saepe cadendo”



Abstract

The Dardanelles and Bosphorus regions have always been considered important cultural, political, demographic and economic hubs first of the Ottoman Empire and then, since 1923, of modern Turkey. The need for rapid movement of people and vehicles by land between Europe and Asia prompted Turkey to build important links along the Bosphorus and the Dardanelles Strait. The construction of a long-span suspension bridge over the Dardanelles Strait in the province of Çanakkale was always considered an important goal for the Turkish government and was completed in March 2022, setting the *current record for the longest span in the world*.

The construction of the *1915Çanakkale Bridge*, an important permanent link between Europe and Asia, has always been regarded as a highly complex structural engineering project. Through the cooperation of the various research and studies, particularly Danish and Chinese, many difficult environmental conditions have been faced and solved: water depth, strong sea currents, high seismic activity and *intense winds* channeling along the Dardanelles Strait contributed greatly to the search for new design and construction techniques, such as specific lifting gantries used in the elevation of deck segments.

After the *collapse of the Tacoma Narrows Bridge in 1940*, a new phase of suspension bridge design opened up, more directed toward understanding the critical aerodynamic phenomena arising from the interaction of the deck with wind action. The *flutter* phenomenon represents an oscillatory-type aerodynamic instability. This thesis focuses on *flutter instability*, one of the most dangerous phenomena that can occur in long-span suspension bridges. The analysis developed aims to clarify how the 1915Çanakkale Bridge responds to dynamic wind phenomena implementing *numerical* and *analytical methods* by using ANSYS and MATLAB software, respectively.

The historical development of suspension bridges is covered in the first introductory section, which includes a brief excursus from the ancient suspension bridges of Peru and Japan to the early 1960s development of long-span suspension bridges with aerodynamic decks, passing through the mid-19th century when *J.A. Roebling* introduced his ground-breaking design method for suspension bridges. The treatment of the aeroelastic instability phenomenon using analytical and numerical methods is then presented. *Steady-state aerodynamics* and *Flutter*, in terms of one and more degree-of-freedom analysis, are described mathematically and the simplified analysis by *A. Namini* and *P. Albrecht* is suggested. The analysis techniques used with ANSYS and MATLAB software are also reported.

Subsequently, the development of the design and realization of the 1915Çanakkale Bridge is presented. The most innovative aspects carried out by the geotechnical and structural engineers for the construction of the foundations, the lifting of the deck and the wind analysis up to the monitoring system, the most modern in the world, are presented. The various effects of wind action on long-span suspension bridges are taken up in this part by deepening the analysis specifically on the 1915Çanakkale Bridge: as this is a project of great significance, many researchers have conducted advanced studies on the overall behavior of the bridge for flutter analyses using wind tunnel on scale models; two of these are reported and their data and results will be compared with those obtained in this thesis.

The modeling concepts on the employed software are introduced in the subsequent chapters of the thesis. The study focuses on the various finite element models created: for the main span, two models, a simpler "fish-bone" model and a more complicated two-axis deck model, are used.

Additionally, the analyses carried out with software are reported, as well as the numerical methods used in this thesis. As the torsional stiffness properties of the deck section change, a preliminary *zero-wind modal analysis* is performed recursively, and the natural frequencies and vibration modes are identified for comparison with the publicly available data.



Then, using the *flutter derivatives* that were specifically included in the various numerical models under consideration, the *flutter analysis* is carried out, which accounts for all the involved aerodynamic loads. The endpoint is to determine the critical flutter couple, which consists of the *flutter frequency* and the *critical wind flutter speed*, which starts the instability. The analyses conducted in the course of the thesis led to the determination of a *critical flutter wind speed* in excess of 84 m/s, which corresponds to approximately 300 km/h, a very high wind speed value (belonging to the V degree of the Saffir-Simpson hurricane scale), which has not occurred historically and is difficult to achieve along the Dardanelles Strait and in the Marmara Sea.

In terms of the critical flutter wind speed and flutter frequency, the results of the flutter analyses carried out with analytical method in MATLAB and numerical method in ANSYS software conform to one another with an relative variance of less than 1%. It is therefore clear that the analytical and numerical approach produce the same result at the engineering level. Furthermore, the results obtained correlate strongly with the range of values found in the literature from authoritative studies conducted in Denmark and China showing a relative variance of less than 5%.

Subsequently, a further method of analysis was introduced on the 1915Çanakkale Bridge, known as the *single-mode criterion*: this is a simplified one-degree-of-freedom flutter analysis criterion that allows the problem to be studied in uncoupled form.

The implementation of *Albrecht's method* enabled a numerical analysis of the design choices and the specific nature of the bridge deck. The aerofoil twin-box section's shape, which is similar to an aircraft wing, gives the structure an exceptional level of stability against one-degree-of-freedom flutter while favoring the appearance of aeroelastic instability phenomena when two or more modes of the structure's vibration are involved. When compared to the long-span bridges of the latter half of the 20th century, the analysis performed using this method demonstrated this advancement in technology and design. In conclusion, it has been found that the numerical and analytical methods used confirm the efficient behavior of the 1915Çanakkale Bridge towards the critical flutter phenomenon.

The perfect combination of design and construction of this important structure laid the foundation for subsequent innovation and research in the field of long-span suspension bridges.



Table of contents

RINGRAZIAMENTI	I
ABSTRACT	II
TABLE OF CONTENTS	IV
LIST OF FIGURES	V
LIST OF TABLES	VIII
THESIS OUTLINE	IX
CHAPTER 1 INTRODUCTION	10
1.1 HISTORICAL DEVELOPMENT OF LONG-SPAN SUSPENSION BRIDGES	12
CHAPTER 2 FLUTTER ANALYSIS OF LONG-SPAN BRIDGES	26
2.1 STEADY-STATE AERODYNAMICS	29
2.2 TWO-DEGREE OF FREEDOM FLUTTER ANALYSIS	32
2.3 ONE-DEGREE OF FREEDOM FLUTTER ANALYSIS	35
2.4 NUMERICAL FLUTTER ASSESSMENT IN ANSYS	37
2.5 ANALYTICAL FLUTTER ASSESSMENT IN MATLAB	41
CHAPTER 3 INNOVATIONS OF 1915ÇANAKKALE BRIDGE	43
3.1 CONSTRUCTION DETAILS AND TECHNOLOGICAL INNOVATIONS	45
3.1.1 Deck design, fabrication and erection overview	45
3.1.2 Soil-structure interaction: foundations, towers and anchor blocks	51
3.1.3 Cable structures: main cable and hangers	58
3.1.4 Structural health monitoring (SHM)	62
3.2 1915ÇANAKKALE BRIDGE'S HYBRID SOLUTION	64
CHAPTER 4 FINITE ELEMENT MODELING	67
4.1 FISH-BONE DECK MODEL	70
4.2 TWO-AXIS DECK MODEL	71
CHAPTER 5 COMPARISON BETWEEN ANALYTICAL AND FE MODELS	73
5.1 LITERATURE STUDIES	73
5.1.1 Chinese study: Liao-Wang	74
5.1.2 Danish study: Rønne-Larsen	76
5.2 ZERO-WIND MODAL ANALYSIS	79
5.2.1 Numerical fish-bone deck model in ANSYS	79
5.2.2 Numerical two-axis deck model in ANSYS	80
5.2.3 Analytical model in MATLAB	82
5.3 FLUTTER ANALYSIS	83
5.3.1 Numerical flutter assessment in ANSYS	83
5.3.2 Analytical flutter assessment in MATLAB	89
5.3.3 Simplified analysis of 1-dof flutter	91
5.4 SUMMARY COMPARISON OF RESULTS	94
CHAPTER 6 CONCLUSIONS	95
REFERENCES	XCVII



List of figures

Figure 1-1: General suspension bridge static scheme (left); Representation of the tensional state on the structure (right) [2].....	10
Figure 1-2: Flutter phenomenon on the SB-9 Glider wings (left); Tacoma Narrows Bridge collapsed by flutter (1940) (right) [5]	11
Figure 1-3: Ancient vines suspension bridges: (a) and (b) Q'eswachaka in Perú (Inka) [6], (c) Iya Kazurabashi Bridge in Japan [7]	12
Figure 1-4: Jacob's Creek Bridge, demolished in 1833 (Finley, 1801) [8].....	13
Figure 1-5: Dryburgh Abbey Bridge (1817), collapsed in 1818 [9]; Rebuilt in 1872 [10]	13
Figure 1-6: Menai Strait Bridge, Wales (Telford, 1826) [4] [11] [12]	14
Figure 1-7: Real Ferdinando Bridge, Italy (Giura, 1828-1832) [13] [14]	14
Figure 1-8: J. A. Roebling Portrait (1847) [5]	15
Figure 1-9: Britannia Tubular Bridge (original, 1850) (left) [4]; Britannia Bridge (rebuilt, 1972) (Stephenson)(right) [15]	15
Figure 1-10: Niagara Falls Bridge (J.A. Roebling, 1855) [4] [16] [17]	15
Figure 1-11: Wheeling Suspension Bridge (Ellet, 1849) [18]; Rebuilt by W. Roebling and Hildenbrand (1872-1874) [4].....	15
Figure 1-12: Brooklyn Bridge, New York (J.A. Roebling, 1883) [19]	16
Figure 1-13: Deflection Theory (Melan, 1888) [4] [21]	16
Figure 1-14: Williamsburg Bridge, New York (Buck, 1903) [4] [22].....	17
Figure 1-15: (a) Bear Mountain Bridge (1924), (b) Benjamin Franklin Bridge (1926), (c) Ambassador Bridge (1929) [5]	17
Figure 1-16: (a) O. Ammann [5]; (b) George Washington Bridge 1 st deck conf. (1931) [23]; (c) double truss deck conf. (1962) [24]	18
Figure 1-17: Golden Gate Bridge (Strauss, 1937) [25]; Bridge in construction (1933) [26].....	18
Figure 1-18: Bronx-Whitestone Bridge, New York (Ammann, 1939) [27] [28].....	19
Figure 1-19: Tacoma Narrows Bridge collapse (Moisseiff, 1940) [5]; Modern Tacoma Bridge (opened in 1950 and 2007) [29].....	19
Figure 1-20: Mackinac Strait Bridge (Steinman, 1957) [30]	20
Figure 1-21: Verrazzano Narrows Bridge, New York (Ammann, 1964) [31].....	21
Figure 1-22: Severn Bridge, England (1966) [4] [32]	21
Figure 1-23: 15 th July Martyrs (First Bosphorus Bridge), Turkey (1973) [33]	22
Figure 1-24: (a) Humber Bridge, England (1981); (b) Humber Bridge in construction [34].....	22
Figure 1-25: Akashi Kaikyo Bridge, Japan (1998) [4] [5]	23
Figure 1-26: Great Belt East Bridge, Denmark (1998) [4] [35].....	23
Figure 1-27: (a) Akashi Kaikyo cross section (American method); (b) Great Bealt East Bridge cross section (European method) [4]	23
Figure 1-28: Jiangyin Yangtze River Bridge, China (1999)(left) [36]; Runyang Yangtze River Bridge, China (2005)(right) [37]	24
Figure 1-29: Xihoumen Bridge, China (2009)(left) [5]; Xihoumen Bridge aerofoil twin box cross section (right) [38]	24
Figure 1-30: Fatih Sultan Mehmet Bridge, Turkey (1988)(left); Yavuz Sultan Selim Bridge, Turkey (2016)(right) [39] [40]	25
Figure 1-31: Ozman Gazi Bridge, Turkey (2016); Ozman Gazi Bridge in construction [41].....	25
Figure 1-32: 1915Çanakkale Bridge, Turkey (2022) [42].....	25



Figure 2-1: Akashi Kaikyo's deck deformations induced by wind [84]	26
Figure 2-2: non-conservative follower loads: (a) $W_{\text{work}} < 0$; (b) $W_{\text{work}} = 0$; (c) $W_{\text{work}} > 0$ [45]	26
Figure 2-3: (a) Static Instability (torsional divergence); (b) Dynamic Instability (flutter) [5] [45]	27
Figure 2-4: Follower force representative of wind action [5]	28
Figure 2-5: Steady aerodynamic model with forces acting on the deck section [46]	29
Figure 2-6: Examples of static aerodynamic coefficients for different deck sections [46]	29
Figure 2-7: Elementary SDOF section model [45]	30
Figure 2-8: Graphical representation of the stability field for torsional divergence [46]	31
Figure 2-9: Two-degree-of-freedom model [45]	32
Figure 2-10: Examples of flutter derivatives [45] [48]	33
Figure 2-11: Definition of flutter critical speed [46]	34
Figure 2-12: Ziegler column (two-degree-of-freedom system) [5]	34
Figure 2-13: Tacoma Narrows Bridge flutter derivatives [46]	35
Figure 2-14: Fundamental modes (1DOF): Torsion, Vertical Bending and Sway mode [51]	37
Figure 2-15: Hybrid finite element model for flutter analysis in ANSYS [53]	38
Figure 2-16: Example of Flutter analysis result [52]	40
Figure 2-17: Perturbated configuration of 1D continuum model [59]	41
Figure 3-1: Gallipoli Campaign (Battle of Çanakkale, 1915) [60]	44
Figure 3-2: Location of 1915Çanakkale bridge [61]	44
Figure 3-3: Representation of 1915Çanakkale bridge dimensions [61]	45
Figure 3-4: 1915Çanakkale bridge's deck cross section	45
Figure 3-5: Local and global analysis FE-model [62]	46
Figure 3-6: Messina's twin-box deck models with different gaps: (a) 26 m; (b) 39 m; (c) 52 m [63]	47
Figure 3-7: Suspended deck fabrication for the 1915Çanakkale Bridge [65]	47
Figure 3-8: Deck lifting gantry general arrangement [42] [61]	48
Figure 3-9: Suspension deck erection scheme [65]	49
Figure 3-10: Single deck segment lift near the tower (a, left); European tower deck block lift (b, right) [61]	50
Figure 3-11: Views of the 1915Çanakkale Bridge's deck from the ferryboat (IABSE Symposium-04.28.2023)	50
Figure 3-12: Geotechnical risks in original alignment [66]	51
Figure 3-13: Original alignment (red) and 4 alternative alignments (purple) [67]	52
Figure 3-14: Cellular caisson with inclusion piles foundation's solution [67]	52
Figure 3-15: Cellular caisson with inclusion piles foundation's depth [42]	53
Figure 3-16: 3D FE-model of piles and caisson [68]	53
Figure 3-17: Ship impact load case on 3D FE-model [68]	54
Figure 3-18: Dynamic soil-structure interaction (DSSI 3D FE-model) [68]	54
Figure 3-19: Tower dimensions [71]	55
Figure 3-20: Full block lifted by offshore floating crane (left); L-shaped half-block lifted by tower crane (right) [70]	56
Figure 3-21: Steps of tower construction by tower crane [69]	56
Figure 3-22: Tower geometry control concept [70]	57
Figure 3-23: European anchor block (left); Asian anchor block with barrettes (right) [66]	58
Figure 3-24: Main cable internal structure (left); main cable installation (right) [72]	59
Figure 3-25: Main cable complete layout (left); Strand erection sequence (right) [69] [73]	59
Figure 3-26: Survey equipment's arrangement for absolute sag [73]	60
Figure 3-27: Temperature measurement points [73]	61



Figure 3-28: Sag adjustment procedure [73].....	61
Figure 3-29: Von Mises stress plot of tower saddle structure (left); Tower saddle installation (right) [72]	61
Figure 3-30: Hangers' installation [72]	62
Figure 3-31: Sensor locations of SHM system of 1915Çanakkale Bridge [71].....	63
Figure 3-32: Deck's SHM system (left) [71]; 1915Çanakkale Bridge's control center (IABSE Symposium-04.28.2023) (right)	63
Figure 3-33: 3D-render of 1915Çanakkale bridge's hybrid solution [75].....	66
Figure 3-34: Views of the 1915Çanakkale Bridge (IABSE Symposium-04.28.2023).....	66
Figure 4-1: 3D representation on CAD software with details of the deck: fish-bone deck model (left); 2-axis deck model (right)	67
Figure 4-2: Meshing procedure: line entities (left) and elements (right).....	68
Figure 4-3: Example of evaluation of the mechanical properties of the section using SDC software.....	69
Figure 4-4: 3D main span fish-bone deck model (left); Fish-bone model constraints (right)	70
Figure 4-5: 3D main span two-axis deck model (left); Two-axis model constraints (right).....	71
Figure 4-6: Matrix27 for flutter analysis in ANSYS model	72
Figure 5-1: Flutter derivatives of Liao-Wang study in China (A1 *, H3 *) [78]	74
Figure 5-2: Flutter derivatives of Liao-Wang study in China (A2 *, A3 *) [78]	75
Figure 5-3: Deck sectional model (scale ratio at 1:130) (left); Full-bridge model (scale ratio at 1:190) (right) [78]	75
Figure 5-4: A1 * flutter derivatives provided by Rønne-Larsen study in Denmark [64].....	77
Figure 5-5: H1 * flutter derivatives provided by Rønne-Larsen study in Denmark [64]	77
Figure 5-6: Sectional model including wind screens (scale ratio at 1:60) [64].....	78
Figure 5-7: Flutter estimated velocities as function of attack angles [64]	78
Figure 5-8: fish-bone deck model: Mode 1, LAT-SYM, $f=0.0416$ Hz (left); Mode 2, VERT-SYM, $f=0.0728$ Hz (right)	80
Figure 5-9: fish-bone deck model: Mode 3, VERT-ASYM, $f=0.0792$ Hz (left); Mode 4, LAT-ASYM, $f=0.1086$ Hz (right)	80
Figure 5-10: fish-bone deck model: Mode 5, VERT-SYM-II, $f=0.1157$ Hz (left); Mode 6, TORS-SYM, $f=0.1474$ Hz (right)	80
Figure 5-11: two-axis deck model: Mode 1, LAT-SYM, $f=0.0489$ Hz (left); Mode 2, VERT-SYM, $f=0.0698$ Hz (right)	81
Figure 5-12: two-axis deck model: Mode 3, VERT-ASYM, $f=0.0782$ Hz (left); Mode 4, LAT-ASYM, $f=0.1002$ Hz (right)	81
Figure 5-13: two-axis deck model: Mode 5, VERT-SYM-II, $f=0.1141$ Hz (left); Mode 6, TORS-SYM, $f=0.1477$ Hz (right)	81
Figure 5-14: 1915Çanakkale Bridge's modal shapes in zero-wind condition (MATLAB)	82
Figure 5-15: Rayleigh coefficients ($\alpha=0.0029$; $\beta=0.0074$ for $\xi=0.5\%$)	84
Figure 5-16: Example of Matrix27 compiling for ANSYS flutter analysis	84
Figure 5-17: Variation of complex eigenvalues' Real part (damping factors) in ANSYS	85
Figure 5-18: Variation of complex eigenvalues' Imaginary part (frequencies) in ANSYS	85
Figure 5-19: Variation of complex eigenvalues' Real part in ANSYS (extrapolation).....	86
Figure 5-20: Variation of complex eigenvalues' Imaginary part in ANSYS (extrapolation).....	87
Figure 5-21: Study of the dependence of critical speed on mechanical damping ξ	87
Figure 5-22: Evolution of torsional modal shape as a function of wind speed (ANSYS)	88
Figure 5-23: Variation of complex eigenvalues' Imaginary and Real part in MATLAB	89
Figure 5-24: 1915Çanakkale Bridge's modal shapes in critical flutter condition (MATLAB)	89



Figure 5-25: Torsional modal shape in zero-wind and critical flutter conditions (MATLAB)	90
Figure 5-26: Tacoma Narrows bridge one-DOF flutter collapse [43]	92
Figure 5-27: 1915Çanakkale Bridge single-DOF flutter analysis	93

List of tables

Table 3-1: Scheme of suspended deck erection [65]	50
Table 3-2: Main cable's composition in main span and side spans [73]	59
Table 3-3: List of SHM system's sensors [71]	64
Table 4-1: Properties of the 1915Çanakkale Bridge fish-bone deck model	70
Table 4-2: Properties of the 1915Çanakkale Bridge two-axis deck model	71
Table 5-1: Mechanical properties provided by Liao-Wang study [76]	75
Table 5-2: Natural frequencies of 1915Çanakkale Bridge provided by Liao-Wang study [76]	75
Table 5-3: Natural frequencies for the 1915Çanakkale Bridge fish-bone deck model	79
Table 5-4: Natural frequencies for the 1915Çanakkale Bridge two-axis deck model	81
Table 5-5: Natural frequencies for the 1915Çanakkale Bridge in MATLAB	82
Table 5-6: Modal frequencies and modal shape comparison in zero-wind condition	94
Table 5-7: Flutter analysis result comparison	94

List of software

- Matlab R2023a, *MathWorks, Inc.*, 2023.
- ANSYS Mechanical APDL 19.0, *ANSYS, Inc.*, 2018.
- F. Algostino, G. Faraggiana, A. Sassi Perino, "Taglio e torsione-sezione sottile" (tool) in *Scienza delle Costruzioni (SDC)*, UTET-Libreria, Torino, Italia, 1998 [software].
- AutoCAD 2023, *Autodesk, Inc.* 2023.
- Microsoft Excel 2021, *Microsoft Office 365*, 2021.



Thesis outline

CHAPTER 1 – Introduction

Suspension bridges represent the cutting edge of structural design and are the focus of important research in deck's shape and slenderness field to limit aerodynamic interactions with the wind. An *historical development of long-span suspension bridges* is introduced in Chapter 1: from the *primitive bridges*, through the mid-19th and early-20th century *technical* and *theoretical revolutions* of J. A. Roebling, O. Ammann, and J. Melan, respectively, to the latest generation of *aerodynamic profile deck suspension bridges*.

CHAPTER 2 – Flutter analysis of long-span bridges

The aeroelastic instability has significant implications for *long-span suspension bridges*. The *Flutter* phenomenon represents an oscillatory-type aerodynamic instability that can occur in a *single modal component* (damping-driven flutter) or, more widely, can result from the *coupling* of two fluctuation modes, flexural and torsional (stiffness-driven flutter). In this chapter, the *theoretical treatment* of single- and multi-DOF flutter is proposed. Then *numerical* and *analytical assessment* of flutter is introduced on the commercial software ANSYS and MATLAB, respectively.

CHAPTER 3 – Innovations of 1915Çanakkale bridge

Chapter 3 focuses on the *historical aspects* that led to the construction of the world record suspension bridge, namely the 1915Çanakkale bridge. A brief cultural introduction enriched with *historical symbolism* of the bridge leads the reader to the more *innovative design and construction aspects* of this impressive structure. These innovations regarding especially the design, construction and in-situ assembly of the *deck*, the design of the *towers* and *foundations* in a highly seismic zone, the *construction of the main cable, the hangers, and the anchor blocks*. Further insight is given into the *bridge monitoring system*, one of the most innovative in the world. In conclusion, the curious *hybrid bridge version* for the 1915Çanakkale Bridge with its advantages and disadvantages is also reported.

CHAPTER 4 – Finite element modeling

The aim of Chapter 4 is to illustrate the construction process of *3D finite element models* calibrated to provide data as similar as possible to other research studies on bridge behavior in *zero-wind modal analysis* and in *flutter analysis*. This provides insight into the *mechanical characteristics* of the deck and its ability to weather dynamic interaction with the wind.

CHAPTER 5 – Comparison between analytical and FE models

Chapter 5 introduces research studies conducted in *China* and *Denmark*, which provided important data for *model calibration*. In the following section, main analyses using commercial software are introduced. The analyses consist of the study of the bridge deck models using *zero-wind modal analysis* to determine the natural frequencies of the bridge. The successive *flutter analyses*, based on *flutter derivatives*, leads to the determination of the *critical flutter speed* U_{CR} and the corresponding *flutter frequency* f_{CR} . The last section of Chapter 5 puts forward the *single-mode criterion*, also known as the simplified one-DOF flutter analysis. This approach, based on matrices and eigenvectors extracted from ANSYS APDL and implemented on MATLAB, allowed the specific nature of the bridge deck to be revealed.

CHAPTER 6 – Conclusions

In conclusion, it was found that the *numerical* and *analytical methods* present very similar results. The *analytical method* is effective as a comparison with complex 3D FE-models, but greatly reducing the computation time. The efficient behavior of the 1915Çanakkale bridge towards the critical flutter phenomenon is confirmed. The aerodynamic deck's shape gives the structure an exceptional level of stability against single-mode flutter, while favoring the occurrence of aeroelastic instability phenomena at very high wind speeds, when two or more modes of the structure's vibration are involved.

CHAPTER 1 Introduction

Othmar Ammann (1879-1965), a renowned Swiss bridge engineer, was a great promoter of bridge aesthetics, arguing that a well-designed bridge had to be functional, safe, and beautiful to look at. His bridges, and particularly his suspension bridges, were often characterized by elegant shapes and flowing curves, making them icons of modern architecture and engineering. *Suspension bridges* represent the cutting edge of structural design and are the focus of important university and other research in the areas of torsional stiffness, slenderness, and deck form to prevent and limit aerodynamic interactions with the wind. Therefore, engineering-wise, understanding suspension bridges can only start with a rudimentary comprehension of their structural underpinnings.

A suspension bridge [1] is a particular kind of structure in which the main cables that support the deck are hung from towers by hangers (or suspenders), which can be either cables or vertical bars.

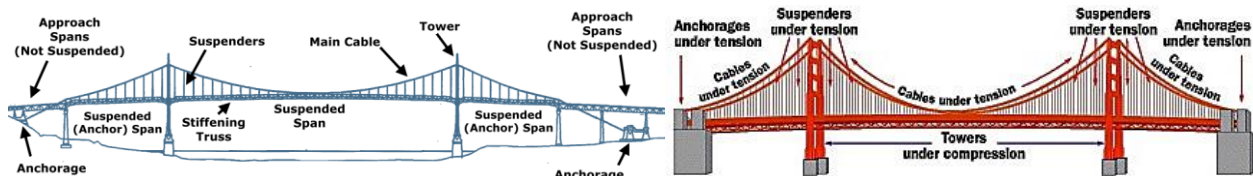


Figure 1-1: General suspension bridge static scheme (left); Representation of the tensional state on the structure (right) [2]

In the case of external anchorages (Figure 1-1 left), the bridge's weight is transferred to the towers and external anchorages via cables; instead in the event of self-anchoring, the structure is self-balancing at the level of the horizontal components of the cable forces beneath the deck. While reinforced concrete or steel are options for the towers, which are largely exposed to compression and bending actions, steel serves as the material for the tension-sensitive cables and hangers. Engineers commonly struggle with aerodynamic instability caused by the impact of wind on the decks because of the importance of the spans on these projects. Due to difficulties with slenderness and weight, aerodynamic steel decks are consequently used.

One of the most important aspects of past structural engineers' research and the evolution of design for suspension bridges is certainly the *deck stiffened system*, which has enabled the transition from suspension bridges that barely exceeded 50 m span in the early 1800s to the present day where the record span exceeds 2000 m.

The historical excursus that is proposed in the introductory part of this thesis allows us to grasp the profound change between the past, present and future of suspension bridge design: from the first vines suspension bridges in Peru and Japan to modern twin-box aerofoil deck solutions, the relentless quest to adopt new techniques to make significant improvements in the stiffening system of the decks is shown, up to the record-breaking span of the present day. Looking at past collapses between the 1800s and 1900s, the importance of a stiff and stable deck in order to span great distances and make the best use of such a static scheme was understood.

The layout of the deck system has without a doubt always been the factor with the greatest influence on suspension bridge design. In particular, two significant theories were created in the middle to late nineteenth century, which had a significant impact on the research of the deck stiffening system: the *linear theory* (Rankine and Steinman, 1858) and the *deflection theory* (Ritter, Lévy, Melan, 1888).

It's important to note that the linear theory on the statics of suspension bridges is a very important starting point in the design of long-span bridges [3]. Numerous advancements have been made since Josef Melan's theory of 1888, which continues to serve as a fundamental cornerstone in the design of long-span suspension bridges, beginning with the linear theory (on which the *Williamsburg bridge* was designed and built in 1903), through Navier's application of the theory of elasticity, as well as with the



help of Castigliano's studies. These theories are the two main theoretical approaches that have contributed to the structural optimization of deck stiffened systems [4]. The deflection theory also provided the starting point for numerous subsequent studies conducted by, among others, *Moisseiff*, *Timoshenko* and *Bleich*. At the same time, with *aeronautical engineering* began to develop the first studies in aerodynamics and the first wind tunnels.

Beginning with *Reynolds'* 1883 studies of laminar and turbulent flows to the development of *Von Karman's theory* (1912) [3], the foundation was laid for the applicability of fluid dynamics for wind.

Josef Melan's theory led in the following years to the first realization of a new generation of suspension bridge: these studies enabled *Ammann* to design the *George Washington bridge* in 1931, which succeeded in doubling the span of the *Ambassador bridge* built only two years earlier and was the first bridge to exceed 1000 m main span.

After the *collapse of the Tacoma Narrows Bridge in 1940*, a new phase of suspension bridge design opened up, more directed toward understanding the critical aerodynamic phenomena arising from the interaction of the deck with wind action. The *flutter* phenomenon proper represents an oscillatory-type aerodynamic instability that arises as a result of non-conservative forces that follow the deformation of the structure (follower-type) as in the case of wind acting on the deformed configuration of the bridge deck [5]. The contribution to the study of flutter made by civil structural engineering and the field of aeronautics has been enormous and has led to the refinement of studies on aerodynamic stability (the subject of this thesis). The study of the shape of the deck, like an airplane wing with pronounced aerodynamic properties, has over the years ensured the use of lighter and more slender superstructures, greatly reducing bridge weights and construction costs.

The great contribution on aerodynamics studies led to the evolution of the stiffness and shape of the deck section. History of suspension bridges goes from the framework deck of the well-known *Brooklyn Bridge* (1883), *Golden Gate bridge* (1937) and *Akashi KaiKyo Bridge* (1998) to the latest generation of suspension bridges characterized by a deck section composed of multiple caissons with aerodynamic shape to ensure low wind resistance and high stability against aerodynamic action.

The *Xihoumen Bridge* (2009) and the *1915Çanakkale Bridge* (2022), with the current longest span in the world (2023 m), are the most recent achievements of the new generation of long-span suspension bridges.

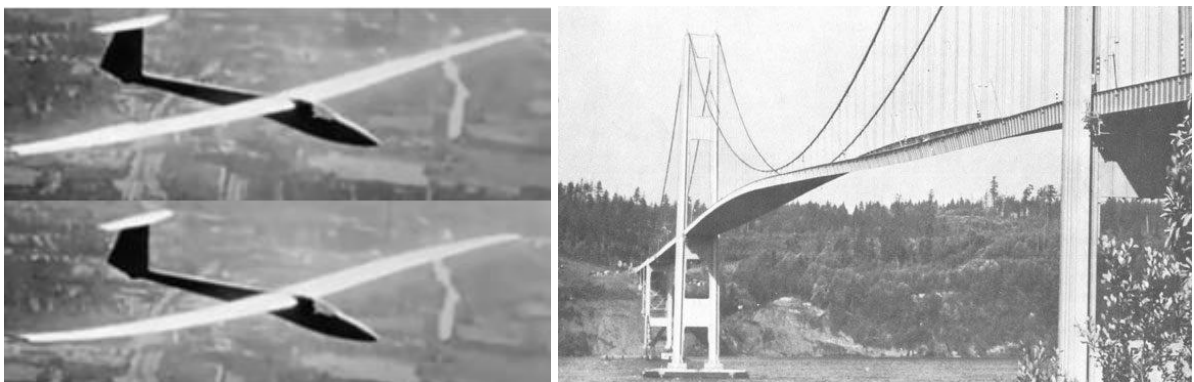


Figure 1-2: Flutter phenomenon on the SB-9 Glider wings (left); Tacoma Narrows Bridge collapsed by flutter (1940) (right) [5]

1.1 Historical development of long-span suspension bridges

Significant progress has been made in recent years in the design of cable-stayed bridges by easily reaching considerable spans, but there is no doubt that suspension bridges represent the most accredited present and future solution for long-span structures. Among the earliest interpreters of bridge building are the Romans: such works represent an invaluable heritage of civil engineering. Even earlier, however, another type of bridge was in use: *the primitive suspension bridge*. The tribes of New Guinea, the Pygmy tribes of Africa, and the Inkas of Peru have always built bridges entirely of vines [4]. The structure of these bridges was intended for the passage of people only: these bridges typically have a main cable running parallel to the bridge, where people walk, and two or more cables hanging from the sides, forming a V-shape that acts as a handrail. One of the best-known examples of this primitive bridge-making technology and one that amazed European explorers who came to Inka territory is the *Q'eswachaka*: this is the last remaining Inka grass suspension bridge of the many that were made to span canyons and rivers. This bridge, still traveled by the native population and in use without interruption for 500 years, spans a narrow canyon above the Apurmac River. The span is 30 meters long and is suspended 15 meters above the river [6]. The disadvantage of V-shaped suspension bridges is that the point of loading significantly bends and lifts the other cables; in fact, when the main cable carries only its own weight, it takes on a catenary shape; however, when vertical loads are applied to it (such as people walking on it), the cable takes on a specific polygonal shape that is determined by the interaction of the loads. These suspension bridges could only be used by one person at a time, so a U-shaped system with a wider bridge was needed. One of the most famous examples of this evolution of suspension bridges suitable for the passage of several people at once and bearing higher loads can be observed in Japan in the Iya Valley. In the past, the main way to cross the river in the Iya Valley was a suspension bridge made of mountain vines. Only three of the original 13 bridges still exist today. The largest and best known of the remaining bridges, *Iya Kazurabashi* [7], spans the Iya River for 45 meters in the centre of the valley (Figure 1-3). Over the centuries the loads acting on bridges and roads became greater and greater, and in Europe and North America the need for innovation arose. Suspension bridges had to innovate significantly from ancient examples in order to support horse-drawn carriages and, later, automobiles in modern traffic. Among the most pressing needs was firstly the flatness of the deck: the catenary shape had to be abandoned in order to achieve a straighter deck. Second, some stiffness had to be achieved to avoid excessive deflection caused by live loads that were beginning to be non-negligible compared to dead load. *Jacob's Creek Bridge* (Figure 1-4) in Westmoreland County, Pennsylvania, was the first suspension bridge to solve these problems in 1801 [4]. The era of contemporary suspension bridges is thought to have begun in this year. *James Finley*, who developed a system for suspending a rigid deck from a bridge's cables in 1808, designed this bridge, which was the first to have all the components of a modern suspension bridge. Finley followed a few rules when maturing his bridge. First, he desired that both the construction and upkeep of the bridge would have reasonable costs. He also wanted his bridge to be unpretentious to build and adaptable to any location so that it could be used all over the state.



Figure 1-3: Ancient vines suspension bridges: (a) and (b) *Q'eswachaka* in Perú (Inka) [6], (c) *Iya Kazurabashi* Bridge in Japan [7]

"The bridge is solely supported by two iron chains, one on each side, the ends being well secured in the ground, and the chains raised over piers of sufficient height erected on the abutments at each side, extended so slack as to describe a curve, so that the two middle joists of the lower tier may rest on the chains," Finley continued in 1810's political magazine *The Port Folio* [8]. Finley's bridge was significantly more robust than the typical wooden truss bridge of the time, which was what made it unique. Finley's bridge could actually support a lot more weight than it did [4].

With Finley's studies there was a major technological advance: one of Finley's bridge's prominent distinctions from historic suspension bridges was that it had a strong, level horizontal deck. The bridge could now easily accommodate wheeled vehicles in addition to just foot traffic. Furthermore, Finley's bridge had two support points for the cables, not just one, at each end, which made it possible for the weight to be distributed more equally, thereby increasing strength.

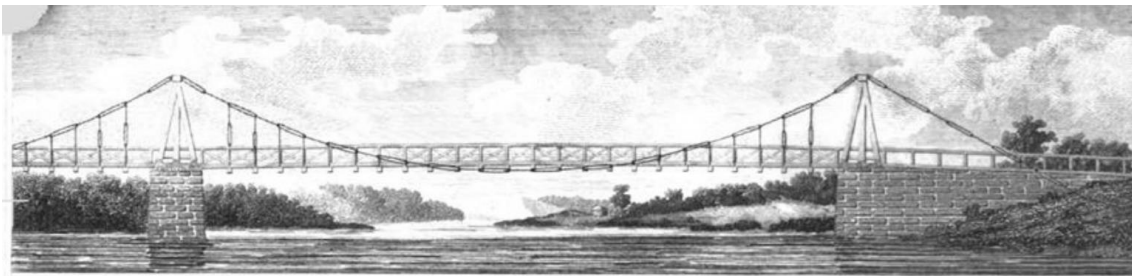


Figure 1-4: Jacob's Creek Bridge, demolished in 1833 (Finley, 1801) [8]

According to his statement [8], the main cable wouldn't deform excessively thanks to the loads being distributed among many hangers. Finley was aware of the technical implications of girder stiffening in suspension bridges: this aspect will be very important in the 900s to achieve longer and longer spans. Finley may in fact be considered one of the fathers of suspension bridges as we know it and the fact that his concepts and creations are still in use today may be one of the greatest memorials to him in the modern era. The same suspension technology that Finley used continues to be utilized in thousands of bridges today. Japan's *Akashi Kaikyo Bridge*, which measures 3911 meters in length with a main span of 1991 meters, was constructed in 1998. Subsequently, the current world record was achieved with the *1915Çanakkale Bridge* in 2022, with a main span of 2023 meters.

New bridges made with Finley's innovative techniques began to appear in the 1820s. The first Finley-type bridge in Europe was constructed by *D. Erskine* in Britain, the *Dryburgh Abbey Bridge* (1817) (Figure 1-5). This slender deck pedestrian bridge, built to cross Tweed River, spanned 79.3m. Unfortunately, the structure immediately manifested deformation problems and excessive vibration as people passed by. In January 1818, a few months after its inauguration, the chain bridge collapsed due to a strong wind.



Figure 1-5: Dryburgh Abbey Bridge (1817), collapsed in 1818 [9]; Rebuilt in 1872 [10]

The *Menai Strait Bridge in Wales* (Figure 1-6), which was designed and constructed by *Thomas Telford* and completed in 1826, was the first significant bridge to use the Finley-invented method. It was the first bridge to surpass the previous record-breaking span length of 150 meters, measuring 168 meters in length. The deck's masonry towers rose 46.60 meters above the water and were suspended 30.50 meters above it. Unfortunately, the bridge became a “victim” of adverse weather events: only the central walkway survived the violent swaying that occurred in January 1839 on the weakened suspension bridge, which caused torsional vibration. The wind permanently damaged over 440 hangers. In the following months, structural rehabilitation work began: the steel chains were installed in place of the wrought iron chains during 1939 repair work, in tandem with a steel stiffening truss.

In the 1830s, the development of suspension bridges became widespread among Italian designers: iron chain suspension bridge over the Garigliano River, popularly known as the *Real Ferdinando Bridge* (Figure 1-7) and designed by *Luigi Giura* (1828–1832), is a remarkable modern example that highlights the importance of stiffened girders in suspension bridges. One of the first in all of continental Europe, it was the first iron suspension bridge constructed in Italy. The deck of the suspension bridge's structural scheme features a span of 85 meters and a width of 5.80 meters.



Figure 1-6: Menai Strait Bridge, Wales (Telford, 1826) [4] [11] [12]

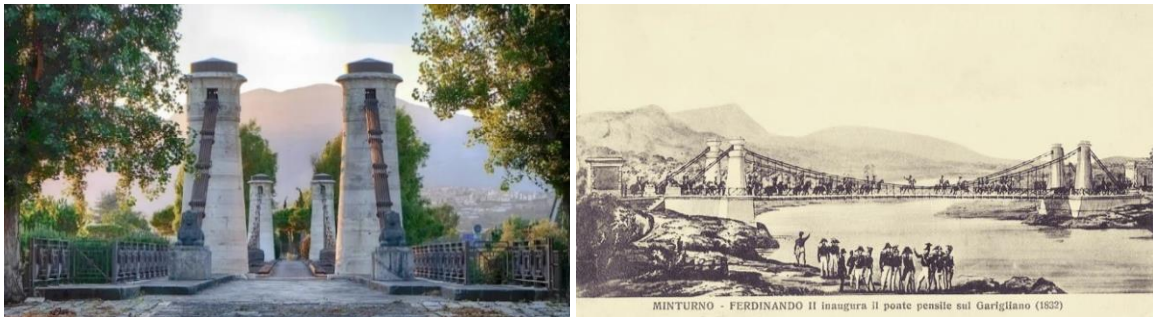


Figure 1-7: Real Ferdinando Bridge, Italy (Giura, 1828-1832) [13] [14]

However, this structure had several design problems. Prominent among them was the inability to take up the asymmetrical vertical actions given by live loads because they resulted in very high deck's deformability [4]. Additionally, because there are no horizontal bracings at all, the bridge is completely inadequate to withstand lateral forces like wind and earthquake, which can result in excessively large horizontal displacements. These evidences support the widely held assumption that 19th-century structures were designed mainly to handle vertical and symmetrical loading conditions while ignoring asymmetrical and horizontal loading conditions [4].

Robert Stephenson took a different approach than Telford and was very interested in the stiffness of suspension bridges. Stephenson favored a more conservative approach to bridge design: in fact, he proposed a massive box with an interior width of 4 meters and a depth of 9 meters to span the 146 meters. It has been known as the *Britannia Tubular Bridge* (Figure 1-9) since it was finished in 1850; During the design it was realized that the excessive deck stiffness provided the suspension system essentially unnecessary. A disastrous fire structurally compromised the central span. Following this nefarious event, the bridge was rebuilt in 1970, making several changes in the following years: initially

constructed as a steel truss arch bridge with a single tier for carrying rail traffic, a second tier was later added and opened in 1980 to accommodate the growth in road traffic. At the turn of the 1850s, a great bridge designer began his career operating in North America. This period is known as the *Roebing's revolution*. *John Augustus Roebing* (1806-1869) (Figure 1-8) expressed his belief that stiffened girder and additional stay cables would make *rigid bridges* to solve problems concerning remarkable collapses of suspension bridges that occurred in the 1810s due to wind oscillations [4]. Two strategies were used to accomplish this goal. He stiffened the beam first with a deep timber truss and then used inclined stays in the outer thirds of the main span. Roebing paved the way toward the modern concept of suspension bridges. He gave birth to major structural works used for years as an example of good suspension bridge technology and stability. The *Niagara Falls Bridge* (Figure 1-10), after four years of construction was completed in 1855 and it was the first example of his technical innovation. This enabled it to achieve the main span record of 251.5 meters.

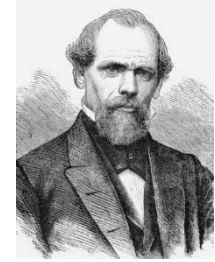


Figure 1-8: J. A. Roebing Portrait (1847) [5]

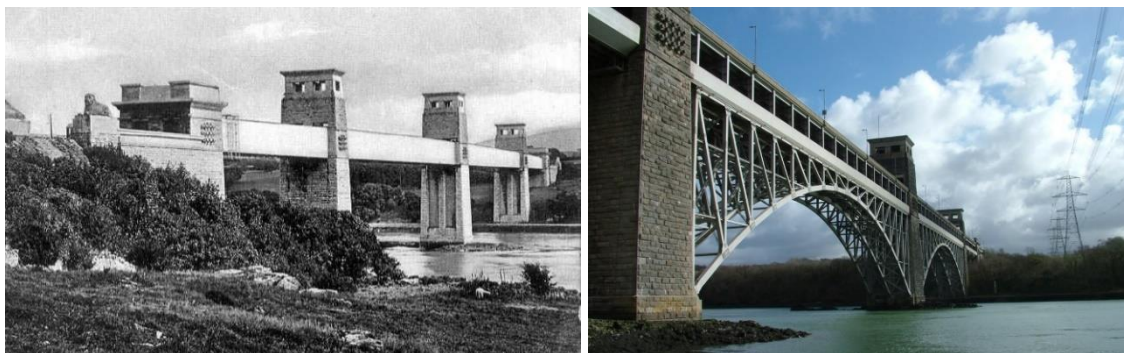


Figure 1-9: Britannia Tubular Bridge (original, 1850) (left) [4]; Britannia Bridge (rebuilt, 1972) (Stephenson)(right) [15]

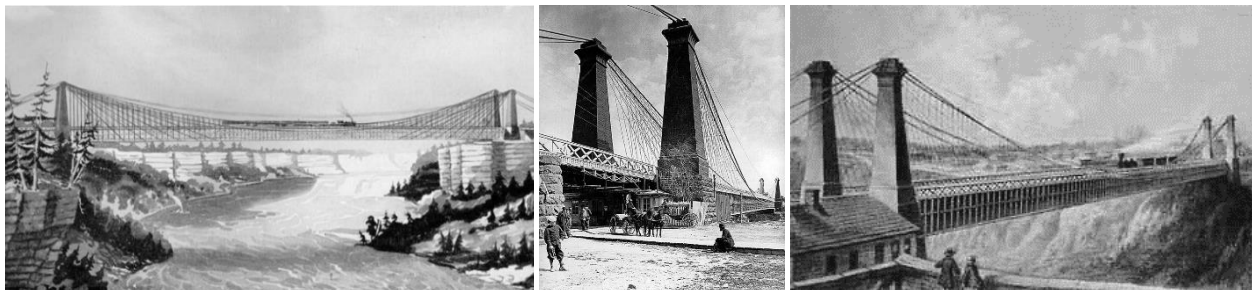


Figure 1-10: Niagara Falls Bridge (J.A. Roebing, 1855) [4] [16] [17]

When the Niagara Bridge was being built, on May 17, 1854, a telegraph announced a major suspension bridge disaster: Roebing rival Ellet's bridge over the Ohio at *Wheeling* had collapsed. The *Wheeling Suspension Bridge*, finished in 1849 as the longest bridge in the world at the time (308 meters main span), was destroyed by a windstorm [4]. Roebing was the only person at the time who fully understood what caused the accident, and he realized the necessity of bracing and stiffening suspension spans to protect them from cumulative oscillations that may be started by the action of wind.

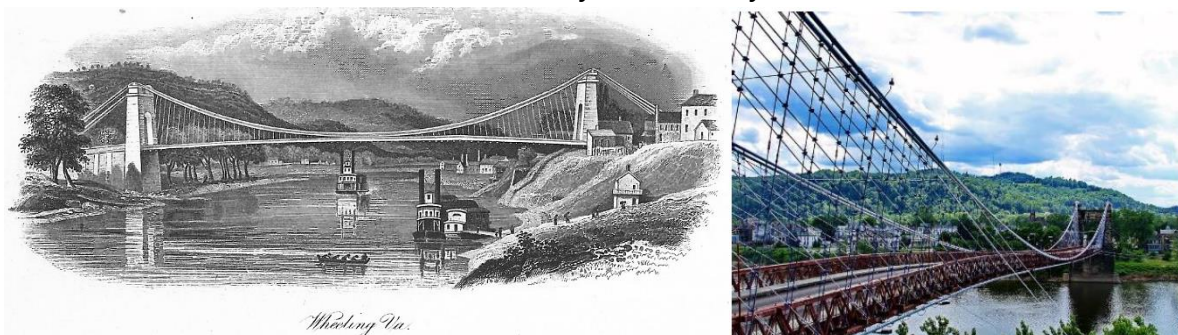


Figure 1-11: Wheeling Suspension Bridge (Ellet, 1849) [18]; Rebuilt by W. Roebing and Hildenbrand (1872-1874) [4]

Following his death in 1869, Washington Roebling and Wilhelm Hildenbrand rebuilt the bridge in 1874 by attempting a “Roeblingizing” operation: the addition of stay cables and deck stiffening truss gave grater structural safety against aerodynamic actions.



Figure 1-12: Brooklyn Bridge, New York (J.A. Roebling, 1883) [19]

The *Brooklyn Bridge* in New York City (Figure 1-12), with a new record span of 486 m, was Roebling's greatest success as a bridge engineer [4]. In 1865, he began work on the design. The system of incline stays that extend downward from the towers is one of its most distinguishing features.

Steel, considered “the metal of the future,” was first utilized by Roebling for the cables: the use of steel rather than cast iron to construct a suspension bridge is one of the most significant innovative aspects. These years saw a significant increase in the main span's length due to the use of this new construction material. In fact, with its deck-stiffened suspension system configuration, this magnificent structure served as the prototype for the first generation of modern suspension bridges.

In the late 1880s bridge engineering started to adopt a new theory of computation. The *deflection theory* (Figure 1-13), which was first presented in 1888 by the Austrian academic Josef Melan [20], explains how the deck and cables deflect as a unit under gravity loads. As a result, as spans lengthen and the weight of the suspended structure increases, the required stiffness of the deck actually decreases. In the 1930s, deflection theory had a particular impact on design as engineers ran for to reduce the ratio of girder depth to span length for a lighter, more graceful appearance without sacrificing safety [21].

Probably the first approach to tackling the issue of the stiffened suspension bridge was *linear theory* [4]. It assumes that the parabolic cable produces an evenly distributed reaction to the girder's bending through the suspenders, with an intensity determined by the entire live load divided by the span.

A stiffening truss was required for the earliest applications to prevent static distortions of the flexible main cable caused by loads transferred by hangers. By adopting a truss that was sufficiently stiff to avoid the deformations of the cable caused by moving loads, Steinman's theory was taken into consideration. Using the premise that the change in geometry brought on by deflections due to the applied traffic load can be neglected. The *deflection theory*, in contrast, uses a nonlinear elastic theory to calculate the bending moments in the stiffening truss while taking into account the displacements of the main cable in a deformed shape, under traffic load. The main cable's geometry will change as a result of the deflection of the deck because hangers connect it to the main cable: in this way the equilibrium must exist in the deflected system.

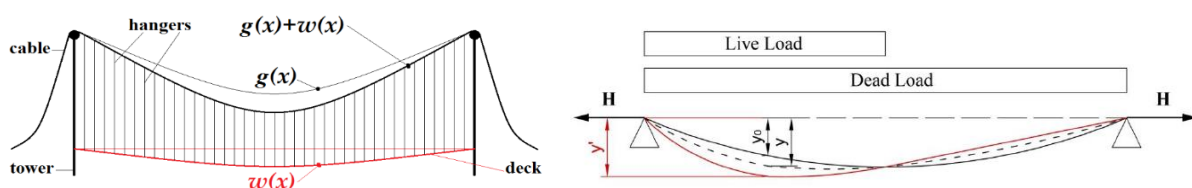


Figure 1-13: Deflection Theory (Melan, 1888) [4] [21]

$g = g(x)$ the displacement of the cable due to the dead load

$w = w(x)$ the displacement of the beam due to the live load

y_0 dead load funicular curve; y' applied live loads funicular curve; y cable deformed shape.

Following the introduction of steel, the first frame towers made entirely of steel began to appear in these years. These began to replace the old masonry towers, which had been widely used in the 1800s (Brooklyn Bridge, Roebling). An early example of this new practice occurs with the construction of a new suspension bridge in the New York City area in 1903: the *Williamsburg Bridge* (Figure 1-14).

It was actually the first bridge to have steel towers rather than masonry ones. Steel towers were put forward by *Buck* because they would make the foundations smaller, could be reinforced if necessary in the future, would be built more quickly, and would be a cheaper option than masonry towers.

Despite Buck's great technological advancement, this massive structure which received severe critique from everyone, seems to have been built with the same caution as the Britannia Tubular Bridge, with its huge, stiffened girder. For 21 years (until it was surpassed by the Bear Mountain Bridge in 1924), its main suspended span, at 488 m, was 1.4 m longer than the Brooklyn Bridge.



Figure 1-14: Williamsburg Bridge, New York (Buck, 1903) [4] [22]

Beginning with the construction of the Williamsburg Bridge in 1903, new suspension bridges occurred in the following years in the North American and Canadian area. The designers of these bridges permanently abandoned cast iron design for a more performance material such as steel. The use of all-steel towers became predominant, progressively moving from a lattice scheme to a frame scheme with St. Andrew's cross bracings, finally abandoning masonry. The theory of deflection allowed the 500-meter maximum span limit to be approached with the *Bear Mountain bridge* in 1924 (497 m) and exceeded it later in 1926 with the *Benjamin Franklin bridge* (533 m). A new record was set in 1929 with the construction of the *Ambassador Bridge* (Figure 1-15) in Detroit with a main span of 564 m: this record lasted only two years until 1931.



Figure 1-15: (a) Bear Mountain Bridge (1924), (b) Benjamin Franklin Bridge (1926), (c) Ambassador Bridge (1929) [5]

Deflection Theory and the development of *Elasticity Theory* with such great exponents as Castigliano, Mohr, and Müller-Breslau led to a major leap forward on new suspension bridge construction.

Othmar Ammann (1879-1965) was one of the great designers of the 1900s. The Swiss engineer and builder emigrated to the United States in 1904 and operated mainly in the New York area where he became famous for the *George Washington Bridge* in 1931 setting a new record for the main span [5].

The *George Washington Bridge* is a key demonstration for figuring out the evolving function of stiffened girder for suspension bridges. The Ambassador Bridge, the longest bridge at the time, *was nearly doubled in length* when the George Washington Bridge's 1067 m main suspended span first opened to traffic on October 25, 1931.

Ammann postulated that this structure showed long-span suspension bridges did not require massive stiffening trusses. In order to achieve a *slender and elegant structure* (Figure 1-16), Ammann's study is considered as revolutionary today as it was for suspension bridge design. His study reveals a new method for designing bridges: in addition to the stabilizing effect of dead loads, the decision to use a thickening hangers system connected to the main cable and the growing number of transverse load-bearing elements allowed for a significant reduction in girder size, creating a pioneering *slender deck*. In 1946, the center median got two more lanes. Although Ammann's original plan called for the addition of a lower deck to house rapid transit was not considered immediately by authorities. Nevertheless, the increasing number of cars, trucks, and buses eventually made it necessary to add more traffic lanes. On August 29, 1962, the George Washington Bridge's lower level became operational.



Figure 1-16: (a) O. Ammann [5]; (b) George Washington Bridge 1st deck conf. (1931) [23]; (c) double truss deck conf. (1962) [24]

Deflection theory was used for the *Golden Gate Bridge's* design, just like it was for the George Washington Bridge. By the time it was finished and began accepting traffic in 1937, the Golden Gate Bridge (Figure 1-17) was the world's longest and largest suspension bridge. The color "International Red" was chosen, and it has since become a landmark and widely recognized symbol for San Francisco and Oakland Bay. A long-span suspension bridge, according to Moisseiff, could cross the strait and be far more functional and attractive than Strauss' original design [4]. Several designs were screened out and a collaboration was established between three distinguished designers of those years.



Figure 1-17: Golden Gate Bridge (Strauss, 1937) [25]; Bridge in construction (1933) [26]

The design of this bridge was carried out by *Strauss, Ammann and Moisseiff* [26]. This collaboration led to the achievement of the new main span record of 1280 m that lasted until 1964.

With this new bridge comes a further evolution of the *towers*: they become extremely tall, easily surpassing 200 m (660 ft) in height. In particular, the towers of the Golden Gate Bridge reach 228 m (746 ft) and feature a new steel structure. The reticular structure is abandoned in favor of a more streamlined, vertical form of multi-story frame. The two main cables leading up the Golden Gate Bridge pass over the tops of the two towers and are fastened at either end by enormous anchorages [4].

The 250 pairs of vertical suspender ropes that span both sides of the Golden Gate Bridge are spaced 15 meters apart. All the ropes were replaced between 1972 and 1976, with the final rope replacement being



finished on May 4, 1976. The Golden Gate Bridge went through modifications in 1953 and 1954 because of a storm that caused it to twist and vibrate enough to cause some minor damage on December 1, 1951. Preventing these flexible structures from moving excessively in the wind has been one of the biggest challenges engineers have faced since the invention of the modern suspension bridge in the early 1800s. The bottom bracing upgrade for the two steel trusses that support the roadway deck is therefore as follows: *It also made the bridge's torsional stiffness greater.*

Golden Gate represents a significant development in cross section, especially in light of the fact that no deck closed sections were utilized prior to 1951.

Ammann's great success due to the George Washington Bridge and his collaboration with Strauss on the Golden Gate Bridge led the Swiss engineer to build a new bridge with a very slender deck and high gantry towers. On April 29, 1939, the *Bronx-Whitestone Bridge* (Figure 1-18) with a span of 701 m was opened to traffic.



Figure 1-18: Bronx-Whitestone Bridge, New York (Ammann, 1939) [27] [28]

Deflection Theory came to an abrupt halt in 1940, however. In this year there was one of the most catastrophic collapses of a suspension bridge: the *Tacoma Narrows bridge* (Figure 1-19).

As a large portion of the acting load was carried by the main cable, Moiseiff designed it using deflection theory principles. As a result, the deck's high deck slenderness and low torsional stiffness were justified by the reduction of bending stress in the flexible deck. The Tacoma Narrows Bridge, with a main span measured 854 meters, was designed to carry both traffic loads and the static impacts of wind; however, the dynamic effects of wind were not taken into consideration. It was a prime example of how aerodynamic stability must be taken into account when designing a bridge.



Figure 1-19: Tacoma Narrows Bridge collapse (Moiseiff, 1940) [5]; Modern Tacoma Bridge (opened in 1950 and 2007) [29]

The bridge occasionally experienced waves moving up and down with extraordinary amplitude even while it was still being built. The side span girders were fastened to large concrete blocks on land with hold-downs after the bridge was opened to traffic. In the side spans but not the main span, these reduced the waves. A motion with no nodes between the towers was the one that was most frequently observed in vertical vibration. On November 7, 1940, early in the morning, the bridge began to exhibit motions of a previously noted kind, but with greater amplitude. The wind speed was higher than anything the bridge had ever experienced, ranging from 65 to 72 km/h. Traffic was suspended. Just after 10 a.m., a crucial event occurred that directly caused the disastrous torsional vibration. Then, the mode was driven by auto-excitation forces, which were powered by the constant wind. As one of the main cables grew longer on one side of the center and shorter on the other, the vertical oscillations soon turned into

rotations, allowing the structure to twist. This torsion mode built up due to the wind velocity, which was high enough that collapse was unavoidable. The wind's subsequent effect tends to cause a buildup of vertical undulations once any small undulation of the bridge has begun. Oscillations presented a tendency to turn into a *torsional motion*, until the *torsional-type oscillations reached destructive amplitudes*. It wasn't the first suspension bridge to fall apart before the Tacoma Narrows Bridge. In fact, a review of suspension bridge history reveals that several of them were destroyed by wind, but the Tacoma Narrows Bridge was by far the longest and most expensive suspension bridge to fall victim to wind interaction. In comparison to other suspension bridges that had been constructed before, the Tacoma Narrows Bridge was unusually long and narrow. The original plan was to use trusses to stiffen the suspended structure, but there were no funds available. Sadly, the stiffening system was quite non-existent. The original tower foundations and anchorages were used to build the new bridge (Figure 1-19). When the new bridge first opened to traffic in the winter of 1950–1951, it was subjected to some of the strongest winds in recent memory and it was a complete success in design.

The towers, main cables, side spans, and anchorages were still present after the center span collapsed into the Tacoma Narrows. The approach spans were unharmed. The bridge's demolition and salvage proved to be as difficult and hazardous as its building. After this catastrophe, the doors opened for a new era of structural design of suspension bridges: the new generation of deck stiffened suspension bridges, a very long period spanning 1940 to 1964. Engineers had to overcome two significant obstacles when building the new Tacoma Narrows Bridge because the topic of aerodynamic stability in suspension bridge design had never been studied before. In order to design a bridge that would not suffer the same fate as the 1940 bridge, they first had to better explain *what happened* to it. Second, they had to decide how to use the old bridge's remains, particularly the piers.

With the least amount of wind resistance, the new Tacoma Narrows Bridge was built. A deep, open stiffening truss with trussed floor beams was the answer. In order to prevent the formation of any large, solid surfaces similar to those responsible for the 1940 Narrows Bridge's failure, the truss members would be designed as shallow. Stiffening trusses that make up the deck system are 10 m high and 18 m wide. Through these important design arrangements, the construction of the second Tacoma Narrows bridge completed in 1950 which led to a major differentiation in deck stiffness from the first 1940 bridge. Among the most useful parameters for identifying bridge deck characteristics are h/L (deck depth-to-span ratio, to define deck slenderness) and w/L (width deck-to-span ratio, to define deck torsional stiffness). The first Tacoma Narrows Bridge of 1940 has an h/L ratio of $1/356$ and a w/L value of $1/65$. The designers of the second Tacoma Narrows bridge, designed 10 years later, preferred a more conservative approach by parameterizing an h/L value of $1/85$ and a w/L value of $1/47$. It is evident from the data how the first bridge compared to the second one is much more slender and less torsionally rigid [4].



Figure 1-20: Mackinac Strait Bridge (Steinman, 1957) [30]

The *Delaware Memorial Bridge* (1951), the *Chesapeake Bay Bridge* (1952), David Steinman's *Mackinac Strait Bridge* (1957) (Figure 1-20) and Othmar Ammann's *Verrazzano Narrows Bridge* (1964) became operational in the United States shortly after the completion of the new Tacoma Narrows Bridge in 1950. Aerodynamic stability requirements served as the foundation for the design of the Mackinac Strait Bridge. After the construction of these important bridges beginning in 1950, the year when the new Tacoma Narrows Bridge was built, there was a period of "apparent calm" in which research and study of aerodynamics of suspension bridges instead never stopped. This research gave rise in 1964 to the birth of the long-span suspension bridges with slender decks.

The *Verrazzano Narrows Bridge* (Figure 1-21) designed by Ammann in 1964 was identified as one of the most noteworthy high deck slenderness suspension bridges. To achieve the new main span record of 1298 m, Ammann introduced a resultant slenderness ratio for the Verrazzano Narrows Bridge of h/L : 1/178 and is significantly lower than that usual for previous U.S. bridges (New Tacoma Narrow - h/L :1/85). The relatively shallow depth of the suspended structure and high aerodynamic resistance are achieved by a novel rigid framing of the entire steel structure.



Figure 1-21: Verrazzano Narrows Bridge, New York (Ammann, 1964) [31]

After the collapse of the Tacoma Narrow Bridge (1940), structural engineering worldwide became aware that the dynamic effects of wind could no longer be neglected, but instead became increasingly crucial to the static and dynamic stability of the bridge. Two different philosophies of long-span suspension bridge design were born: the issue of aerodynamic stability was recognized by *American engineers*, who then looked for novel approaches to improve the performance of bridge decks and achieve longer spans. To increase the stability of the bridge deck, two main strategies were employed: (a) against aerodynamic effects, adopt a stiffening truss and an open-grid deck to prevent the formation of wind vortices; and (b) increase stiffness by giving the bridge more mass (or weight). Stays have occasionally been used since Roebling's first applications, but only as supplemental or emergency measures [4]. *European engineers* adopted box-shaped streamline cross-sections, whose streamlined profile could lessen the effects of wind pressure by suppressing the appearance of vortices, as a completely different strategy. The *Severn Bridge* (Figure 1-22), designed in 1966, was the first suspension bridge to represent this revolution.



Figure 1-22: Severn Bridge, England (1966) [4] [32]

The steel weights of suspension bridges constructed in Europe after the 1960s were significantly lower than those of their American counterparts; this trend was particularly noticeable in the *First Bosphorus Bridge* (Figure 1-23) and the *Humber Bridge*, which share many structural principles with the Severn Bridge. The construction of the *15th July Martyrs* bridge in Istanbul shifted the focus on building record long-span bridges to the Middle East. In the following years a new record-breaking bridge with a span of 1410 m was built in the United Kingdom: the *Humber Bridge*.



Figure 1-23: 15th July Martyrs (First Bosphorus Bridge), Turkey (1973) [33]

The *Humber Bridge* (Figure 1-24) was the first suspension bridge to cross a span of 1400 m and would hold the span record until 1998. The Humber has inclined hangers and aerodynamic steel box girders, just like its forerunners the Severn and Bosphorus. The two main cables are carried by the slipformed reinforced concrete towers, which are 155 m above the caisson foundations.

An important aspect that distinguishes the evolution toward increasingly leaner decks is the h/L ratio: in contrast to the Golden Gate Bridge, which is frequently cited as the most beautiful bridge in the world, which has a h/L ratio of 1/170, the Humber Bridge's deck only serves to distribute localized loads over the few closest hangers and is relatively thin at 1/313 [4].

In the 1980s and 1990s, technological advancement led to the construction of two record-breaking suspension bridges in 1998: the Japanese *Akashi Kaikyo Bridge* (Figure 1-25) and the Danish *Great Belt East Bridge* were built. The first is a symbol of American style, and the second is a representation of the European approach to bridge design.



Figure 1-24: (a) Humber Bridge, England (1981); (b) Humber Bridge in construction [34]

After World War II, Japan faces a difficult and challenging time in the country's reconstruction. The Akashi Kaikyo Bridge's completion served as the ideal representation of Japan's Post-War civil engineering achievements. The design of this impressive structure led to the achievement of a new record-breaking span close to 2000 m. Its main span reached 1991 m making it the longest span bridge in the world. This record will last until 2022 with the completion of the "Dardanelles Strait Bridge".

For the design and completion of the *Akashi Kaikyo* suspension bridge, several novel technologies were created. Long suspension bridges' aerodynamic stability presents formidable challenges to designers. The largest wind tunnel in the world was built by the Public Works Research Institute under a contract with the Honshu-Shikoku Bridge Authority, and full-section models were tested in laminar and turbulent wind flow to validate the design of the longest suspension bridge in the world.



Figure 1-25: Akashi Kaikyo Bridge, Japan (1998) [4] [5]

The “antagonist” European record proposal is the aerofoil-like *Great Belt East Bridge* (Figure 1-26). It was completed a few months before the Akashi Kaikyo Bridge and with its span of 1624 m set a new record for span but would hold only a few months until the Japanese bridge opened to traffic. With a clearance of 65 m below the bridge girder, the East Bridge is a landmark that spans the international shipping channel between the Baltic and the North Seas. The 2700-meter-long suspension bridge's superstructure is a fully welded, aerodynamically shaped closed box girder that runs continuously between anchor blocks.

Thus, comparing the two most important bridges built at the end of the second millennium shows well the difference between the two design models: American and European ones (Figure 1-27).

When comparing the depth-to-span ratio of the Great Belt East Bridge to that of the Akashi Kaikyo Bridge, it can be seen that the difference has a significant impact on the weight of the stiffening girder: thanks to the use of streamlined box girders, the steel deck weight of the Great Belt Bridge is 56% lower than that of the Akashi Kaikyo Bridge. These notable design differences are clearly seen in the choice of deck depth: the Great Belt has a deck height of 4 m while the Akashi Kakyo has a deck height of 14 m. Also notable is the difference in slenderness between the two structural works. The Great Belt achieves an h/L ratio of $1/406$ while the Akashi Kaikyo stops at $1/142$ [4].



Figure 1-26: Great Belt East Bridge, Denmark (1998) [4] [35]

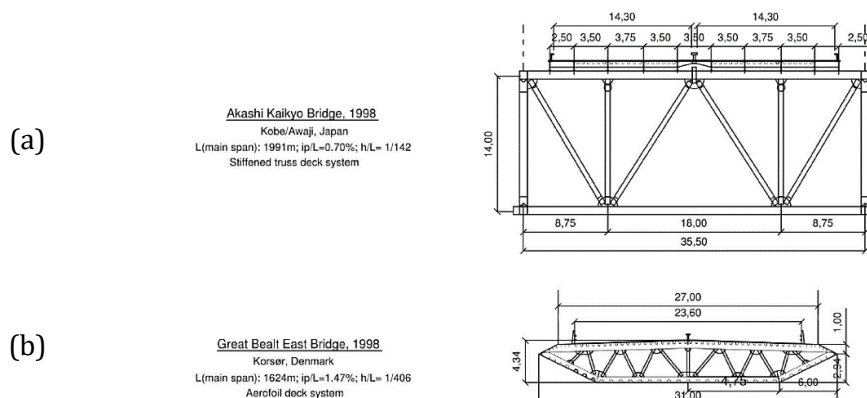


Figure 1-27: (a) Akashi Kaikyo cross section (American method); (b) Great Belt East Bridge cross section (European method) [4]

The evolution of the *European approach* of building new suspension bridges is being carried forward by China. The construction of increasingly slender decks finds fulfillment in the construction of the *Jiangyin Yangtze River Bridge* (Figure 1-28 (a)) in 1999 with a span of 1385 m. Then in 2005 the *Runyang Bridge* (Figure 1-28 (b)) is built with a span of 1490 m. The record according to the method proposed by European engineers comes in 2009 with the construction of the *Xihoumen Bridge* (Figure 1-29) whose main span exceeds by 26 m the record set in 1998 in Denmark by the Great Belt East Bridge. The particularity of the design choices for this bridge involves the use of aerodynamic deck with a 6 meters *air-gap* between the twin-box girders. This design choice stems from the design studies of the *Messina Strait Bridge* and will be repeated in the design and construction of the *1915Çanakkale Bridge* in Turkey.



Figure 1-28: Jiangyin Yangtze River Bridge, China (1999)(left) [36]; Runyang Yangtze River Bridge, China (2005)(right) [37]

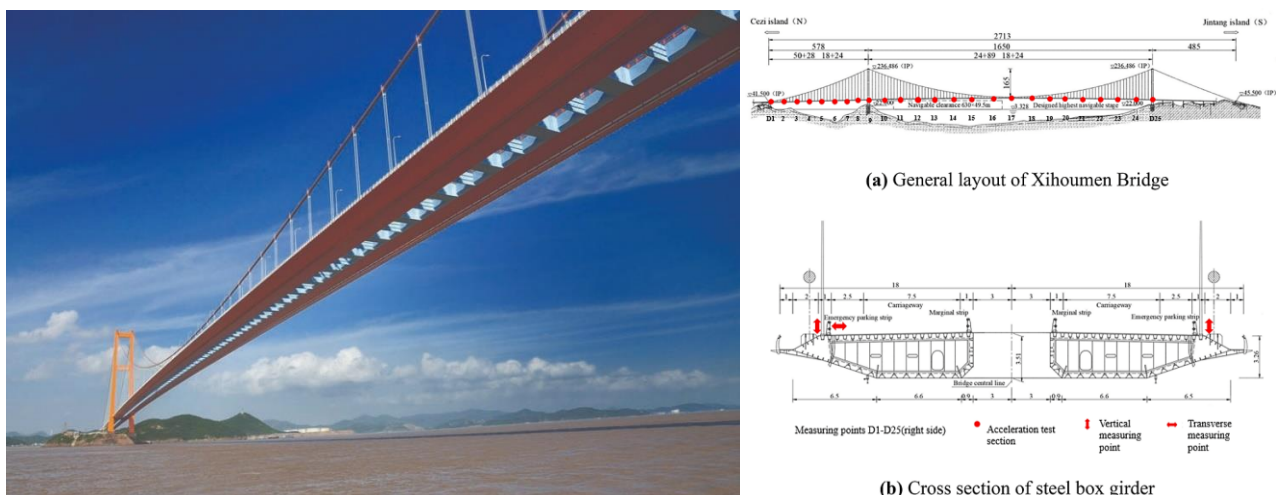


Figure 1-29: Xihoumen Bridge, China (2009)(left) [5]; Xihoumen Bridge aerofoil twin box cross section (right) [38]

The construction of long-span suspension bridges also has its roots in the Arab countries as well as in the Far East. Turkey represents one of the symbolic countries for the construction of long-span suspension bridges, which are key hubs for transportation systems and are necessary in Turkey as a transit country between Europe and Asia. The most crucial links in the transportation system are orthotropic long-span steel deck bridges [39]. From 522 BC to 485 AD, bridge construction on the Bosphorus Straits was widespread. The Bosphorus River long-span bridge was first decided to be built in 1957, though. The *First Bosphorus Bridge* (Figure 1-23) (also known as the *15th July Martyrs*) construction began in 1970, and it was completed in 1973, in time for the Republic of Turkey's 50th anniversary. Up until the Humber Bridge's completion in 1981, the bridge's main span made it the longest suspension bridge in Europe. The Humber and Severn Bridges, which are the first contemporary bridges in Europe with the aerodynamic box deck section, share many structural characteristics and design considerations with this bridge. It represents a novel method of bridge design with a main span of 1074 meters. Second project crossing the Bosphorus Strait was the *Fatih Sultan Mehmet* (Figure 1-30), which is the *Second Bosphorus Bridge*. The bridge was the fifth-longest suspension bridge in the world

when it was finished in 1988 after construction began in 1986. The *Third Bosphorus Bridge* was built over a three-year period, beginning in 2013 and ending in 2016.

At the mouth of the Bosphorus River where it empties into the Black Sea, the Third Bosphorus Bridge, also known as the *Yavuz Sultan Selim Bridge* (Figure 1-30) has a *hybrid* cable-stayed-suspension structural system, is situated. It lies about 5.0 kilometers north of the First Bosphorus Bridge. In the three years between 2013 and 2016, the Osman Gazi Bridge, also known as the Izmit Bay Bridge, was constructed. In the three years between 2013 and 2016, the *Osman Gazi Bridge* (Figure 1-31), also known as the *Izmit Bay Bridge*, was constructed. The bridge was the fourth longest suspension bridge in the world, with a main span length of 1550 m.

Nearly all of the population is concentrated in the area surrounding the Dardanelles Strait. A new long-span suspension bridge, the *1915Çanakkale Bridge* (Figure 1-32), also called *Dardanelles Strait Bridge*, was decided to be constructed due to this significant geographic location.

It was given that name in honor of Turkey's significant victory in this area during World War I. Its 2023 m main span, which was inaugurated in March 2022 after 4 years of construction, now holds the world record.



Figure 1-30: Fatih Sultan Mehmet Bridge, Turkey (1988)(left); Yavuz Sultan Selim Bridge, Turkey (2016)(right) [39] [40]

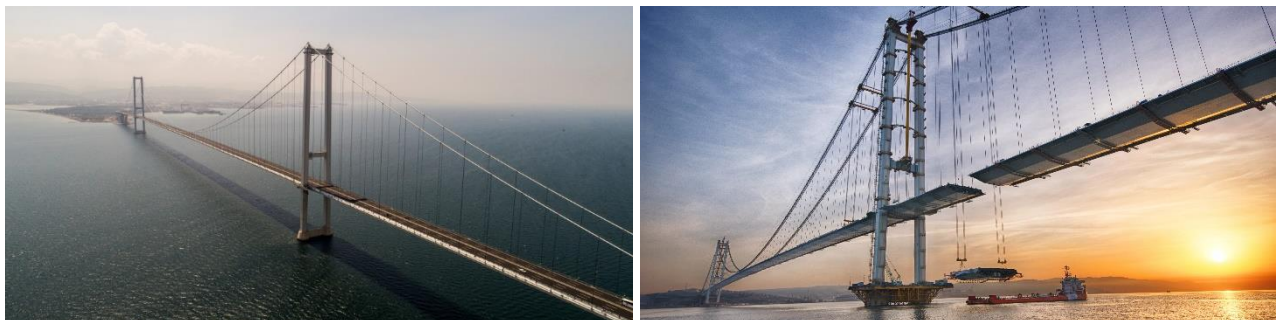


Figure 1-31: Ozman Gazi Bridge, Turkey (2016); Ozman Gazi Bridge in construction [41]



Figure 1-32: 1915Çanakkale Bridge, Turkey (2022) [42]

CHAPTER 2 Flutter analysis of long-span bridges

A series of vertical hangers connect the deck of suspension bridges to the steel cables; this arrangement can cause more serious deck deformations (Figure 2-1). Due to their flexibility, these kinds of structures are frequently subjected to wind action, which could cause long-span bridges to become unstable or vibrate excessively [43]. Aeroelastic instability, which results from the interaction of an air flow and the elastic structure of bridges, is a phenomenon that has significant implications for long-span suspension bridges. It includes torsional divergence, galloping, flutter, and vortex-induced vibrations. *Flutter* is a specific type of aeroelastic instability that can occur in a *single modal component* (one-DOF, damping-driven flutter) or, more widely, can result from the *coupling* of at least two fluctuation modes, flexural and torsional (two-DOF, stiffness-driven flutter), that have similar deformed shapes and act on the deck. The distinctive feature of *coupled flutter* phenomenon is the matching of two degrees of freedom: torsional and vertical motion are timed at the same frequency [44]. The system receives energy from the wind as it approaches relative frequencies. The design prescribes that the maximum wind speed estimated at the bridge site be sufficiently lower than a critical value in order to avoid instabilities. Modern long-span bridge designs involve defining appropriate wind stories, combining experimental testing in a wind tunnel on scaled models of the main structure with computer analysis that relies on analytical or semi-analytical models, as well as numerical procedures that are implemented in computer programs and typically call for experimentally determined parameters, like *flutter derivatives*. These analyses are based on a precise *time domain* analysis evaluation or, as in the case under consideration in this thesis, in a more widespread *frequency domain* of wind effects on the decks. To concentrate on the behavior of the bridge and the local effects, sections of the deck are also studied. Research is increasingly focusing on extremely aerodynamic deck sections, like airplane wings, to lessen these harmful wind effects.



Figure 2-1: Akashi Kaikyo's deck deformations induced by wind [84]

The *flutter* phenomenon, occurred during the *collapse of the Tacoma Narrows Bridge in 1940*, properly represents an oscillatory-type aerodynamic instability that arises as a result of non-conservative forces that follow the deformation of the structure (follower-type) as in the case of wind acting on the deformed configuration of the bridge deck [5]. Figure 2-2 shows an example of a free-standing column subjected to a compressive non-conservative follower (tangential) force at the tip. Cases (a), (b) and (c) are force layouts that perform different work depending on the load history while reaching the same final configuration. These forces are said *follower-type* as they follow the deformation of the structure (Figure 2-4), and *aeroelastic forces* are a case of follower-type forces.

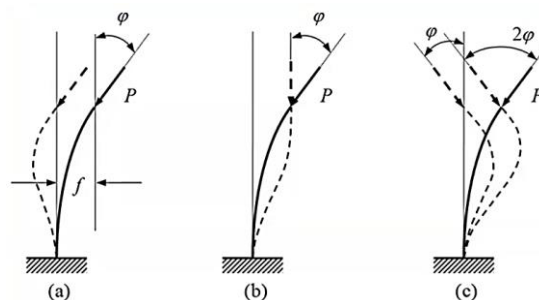


Figure 2-2: non-conservative follower loads: (a) $Work < 0$; (b) $Work = 0$; (c) $Work > 0$ [45]

Elastic stability in the presence of non-conservative forces must, however, necessarily be studied in the dynamic domain in order to correctly predict the instability phenomena that may occur.

Two main types of instability can be identified: *torsional divergence* (Figure 2-3 a), which represents a static phenomenon and can be considered as analogous to Eulerian-type elastic instability (buckling). In particular, the *torsional divergence* phenomenon in long-span bridges subject to wind load, being a *static aeroelastic instability*, occurs in the absence of oscillatory motion of the structure and is governed by a single critical parameter, the *critical wind speed* (U_D), analogous to the *Eulerian critical load* (N_{CR}). This analogy lies in the fact that these are two critical parameters of load acting on the structure. The second instability phenomenon is *flutter* (Figure 2-3 b), i.e. aeroelastic instability, which results in oscillations of increasing amplitude due to nonconservative follower-type forces. In this case there are two critical parameters of flutter: a critical load parameter, i.e. the *wind speed* (U_{cr}) and a *critical frequency* parameter (ω_{cr}).

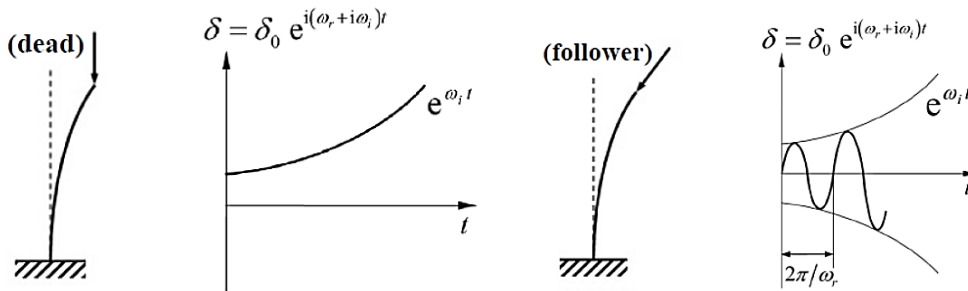


Figure 2-3: (a) Static Instability (torsional divergence); (b) Dynamic Instability (flutter) [5] [45]

The designer can determine the order of magnitude of the critical wind speed at which instability may occur thanks to theoretical models and numerical models created with FEM software, both of which are crucial. By linearizing the phenomenon and introducing coefficients derived from scalar models, analysis in the frequency domain is achievable [44]. Due to the structures' elastic-linear behavior, which has a sinusoidal exponentially damped response, an analytical approach may be considered. Additionally, it is possible because oscillatory motion about equilibrium configuration under average wind conditions causes the transition between stable and unstable configuration to occur.

Based on the above assumptions, it is then possible to introduce the dynamic problem that can be represented, in linearized form, with this equation:

$$[M] \cdot \{\ddot{\delta}(t)\} + [K] \cdot \{\delta(t)\} = 0 \quad (2-1)$$

where:

- $\{\delta(t)\}$: displacements vector, time depending;
- $[M]$: mass matrix;
- $[K]$: stiffness matrix.

The solution of the system is provided by the form $[A]\{\delta\} = 0$ and it actually makes it possible to find the eigenvalues and eigenvectors $\{\delta\}$ in the structure's undeformed configuration. The equation reflects the suspension bridge's stress-free configuration and makes it possible to calculate the mass matrix and system stiffness. Static prestressed configuration could be used to perform accurate modal analyses for these kinds of structures. The satisfy characteristic equation is given by:

$$([K] - \omega^2[M])\{\delta\} = \{0\} \quad (2-2)$$

Continuing the analysis in the discrete field and dealing with n-degree-of-freedom systems such as long-span bridges, it is possible to completely define the *aeroelastic equation of motion*. In reality, the interaction between bridge vibration and wind flow is typically idealized as being divided into two types of forces: *motion dependent* and *motion independent* [5]. The first type vanishes if the structure is rigidly constrained, while the latter is dependent only on the wind characteristics and section geometry and



exists whether the bridge is in motion or not. This schematization suggests the general form in which the equation of motion under the influence of aerodynamic forces can be expressed:

$$[M]\{\ddot{\delta}\} + [C]\{\dot{\delta}\} + [K]\{\delta\} = \{F\}_{mi} + \{F(\delta, \dot{\delta})\}_{md} \quad (2-3)$$

where:

- $[M]$: mass matrix;
- $[C]$: damping matrix;
- $[K]$: stiffness matrix;
- $\{\delta\}$: displacements vector;
- $\{F\}_{mi}$: *motion-independent* wind force vector;
- $\{F(\delta, \dot{\delta})\}_{md}$: *motion-dependent* aeroelastic force vector.



Figure 2-4: Follower force representative of wind action [5]

Thus, the external forces introduced into the equation are representative of conservative forces (independent of motion) and non-conservative forces (dependent on motion). The latter depend on time and structural configuration, which is why they are also referred to as follower-type forces.

The structure of the bridge can deform due to forces that are both motion-dependent and motion-independent, as is well known. The consequences of instability, in particular, varies significantly between the two types of external acting forces: aeroelastic instability is generated only by the motion-dependent part, which is essentially undetectable in short-span bridges, whereas it is essential and the subject of in-depth analysis in flexible structures like long-span bridges.

The particularity of aerodynamic phenomena lies in the combined behavior of two fundamental elements: the elastic slender structure and the action of the wind on the deck. When the two independent systems come into contact, a unique system with different characteristics is created in which bridge and wind interact dynamically. Flutter instability can be analyzed as a fully dynamic phenomenon and differs substantially from other aeroelastic phenomena such as torsional divergence, galloping or buffeting, which can be handled by abandoning the dynamic treatment in favor of a quasi-static approach. The uniqueness of flutter lies in the possibility of studying it in the dynamic domain or with a quasi-static approach, which makes it stand out among aeroelastic phenomena.

Different modes of analysis will be applied on the structure examined in this thesis. However, it is intended to first introduce the basis of theoretical treatment at this phase, to fully analyze the aeroelastic instability of the *1915Çanakkale Bridge*:

- *Steady-state aerodynamics;*
- *two-degree-of-freedom flutter analysis;*
- *one-degree-of-freedom flutter analysis.*

2.1 Steady-state aerodynamics

The analysis is performed considering a *stationary deck condition* arranged with different *attack angles* (α) and the application of the resultant of the pressures generated by the wind on the deck section contour [46]. This resultant of pressures has a point of application outside the section and generic inclination. The resultant is transported to the barycenter of the section and decomposed into plane forces in the x- and y-directions (*Drag* and *Lift Forces*, respectively) and a *moment* component (*Moment*) that is *torsional* on the section. The analysis provides one to assess the stability with regard to the deck's deformed shape due to wind behavior. Furthermore, it is conceivable to think of a laminar flow that produces constant forces in the direction of the bridge. Figure 2-5 illustrates the moment around the z axis, the Lift force in the y direction, and the Drag force in the x direction:

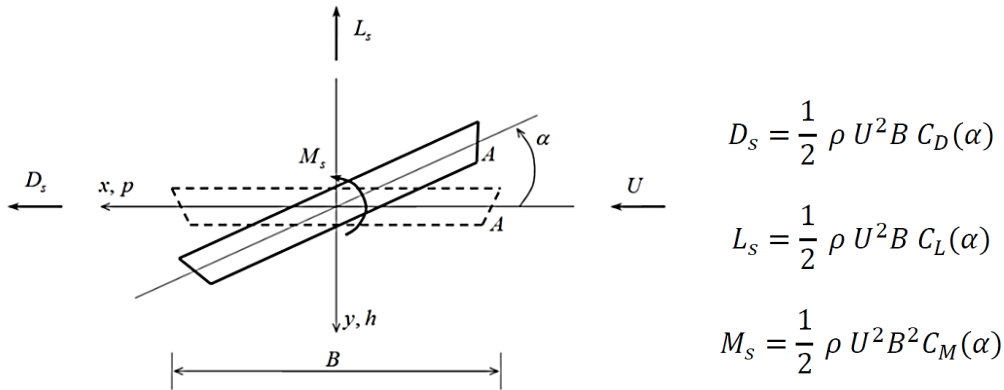


Figure 2-5: Steady aerodynamic model with forces acting on the deck section [46]

where:

- ρ : air density [kg/m^3];
- U : average wind speed [m/s];
- B : deck width [m];
- α : attack angle [deg].
- $C_D(\alpha), C_L(\alpha), C_M(\alpha)$: non-dimensional *static aerodynamic factors* of Drag, Lift and Moment.

In a wind tunnel with a scale sectional model, where variations of α are possible, aerodynamic factors are analyzed to determine forces. By dividing D_s, L_s by $(1/2)\rho B U^2$ and M_s by $(1/2)\rho B^2 U^2$ it is possible to experimentally evaluate the *static polars* C_D, C_L and C_M .

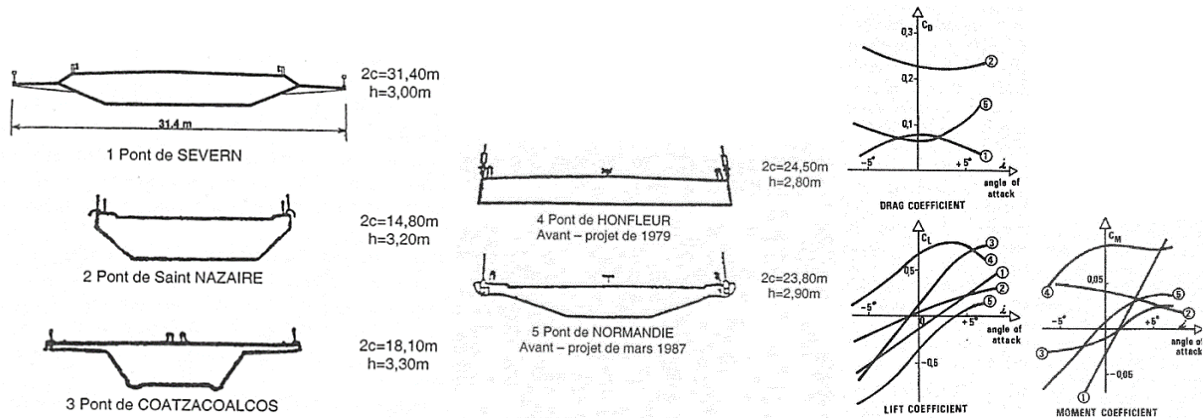


Figure 2-6: Examples of static aerodynamic coefficients for different deck sections [46]



For small angles of attack (α), it is possible to approximate the calculation and linearize the equations of D_s, L_s, M_s shown above in the Figure 2-5:

$$D_s = \frac{1}{2} \rho U^2 B C_D(0) \quad (2-4)$$

$$L_s = \frac{1}{2} \rho U^2 B \left[C_L(0) + \left(\frac{dC_L}{d\alpha} \right) \alpha \right] \quad (2-5)$$

$$M_s = \frac{1}{2} \rho U^2 B^2 \left[C_M(0) + \left(\frac{dC_M}{d\alpha} \right) \alpha \right] \quad (2-6)$$

Torsional Divergence

Torsional divergence is a phenomenon of static torsional instability that occurs due to the loss of total torsional stiffness (elastic + aerodynamic). This phenomenon occurs when the natural frequency of a mode decreases to zero as wind speed increases.

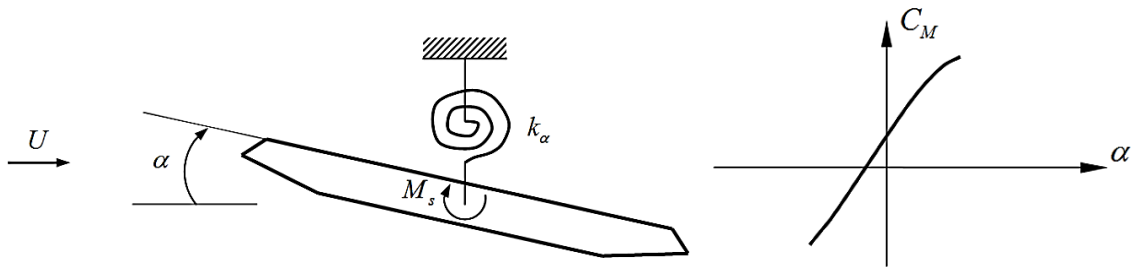


Figure 2-7: Elementary SDOF section model [45]

In general, the wind increasing against the structure causes both forces and aerodynamic moments on it, putting forth an average pressure proportional to the square of the wind speed. At a critical wind speed, a drag force and a wind-induced torque that grows with angle of attack may cause the deck loaded on the contour by the pressure forces to deform out of plane [43]. Torsional divergence can be studied using a simplified sectional model; only the portion of the deck submerged in the two-dimensional flow in the one-degree-of-freedom system, as shown in Figure 2-7, is considered. A torsional effect on the deck occurs because the section is rotated by its own momentum.

Because M_s is stationary, it depends on α but not on time. Considering a small angle of rotation ($\alpha \rightarrow 0$), the components of the equilibrium equation result to be:

Elastic moment per unit length (internal)

$$M_e = k_\alpha \alpha \quad (2-7)$$

where:

- k_α : torsional stiffness per unit length [Nm/m]

Aerodynamic moment per unit length (external)

$$M_s = \frac{1}{2} \rho U^2 B^2 \left[C_M(0) + \left(\frac{dC_M}{d\alpha} \right)_{\alpha=0} \alpha \right] \quad (2-8)$$

It is possible to see that the M_s effect's instability rises with wind speed.

$M_e = M_s$ is necessary for equilibrium, so as a result:

$$k_\alpha \alpha = \frac{1}{2} \rho U^2 B^2 \left[C_M(0) + \left(\frac{dC_M}{d\alpha} \right)_{\alpha=0} \alpha \right] \quad (2-9)$$



Collecting the terms dependent on alpha at the first member, Equation 2-9 becomes:

$$\left[k_\alpha - \frac{1}{2} \rho U^2 B^2 \left(\frac{dC_M}{d\alpha} \right)_{\alpha=0} \right] \alpha = \frac{1}{2} \rho U^2 B^2 C_M(0) \quad (2-10)$$

Aerodynamic stiffness is subtracted from *elastic stiffness*, making the structure more torsionally deformable. The *total stiffness* of the system is therefore expressed as:

$$k_{TOT} = k_\alpha - \frac{1}{2} \rho U^2 B^2 \left(\frac{dC_M}{d\alpha} \right)_{\alpha=0} \quad (2-11)$$

By the critical condition $k_{TOT} = 0$, it is possible to evaluate *critical speed of torsional divergence* (U_D):

$$k_{TOT} = 0 \rightarrow U_D = \sqrt{\frac{2k_\alpha}{\rho B^2 \left(\frac{dC_M}{d\alpha} \right)_{\alpha=0}}} \quad (2-12)$$

This is an approximate evaluation with linearization for the one-degree-of-freedom model.

From Equation 2-12, it is clear how much the width of deck B affects it. The presence of the B value in the denominator affects the critical speed of torsional divergence in an inversely proportional manner. The representation in Figure 2-8 shows the variation of the elastic reaction moment and the aerodynamic moment as a function of wind speed squared [46]. These moment variations are shown as derivatives of M_s and M_e with respect to the angle of inclination α . It is evident how the two values of external and internal moment present different trends: the derivative of M_s with respect to the angle of inclination α presents a linear trend with respect to the wind speed squared ($\propto U^2$), while the derivative of M_e assumes a constant value. This results in two possible cases for the torsional divergence stability:

- When $\frac{dM_s}{d\alpha} < \frac{dM_e}{d\alpha}$ the system is *stable*;
- When $\frac{dM_s}{d\alpha} \geq \frac{dM_e}{d\alpha}$ the system is *unstable*;

The graph illustrates that when two lines of stabilizing and destabilizing moments intersect, M_s grows above M_e , and at this point, the wind speed U^2 is the U_D^2 that causes torsional divergence of the bridge.

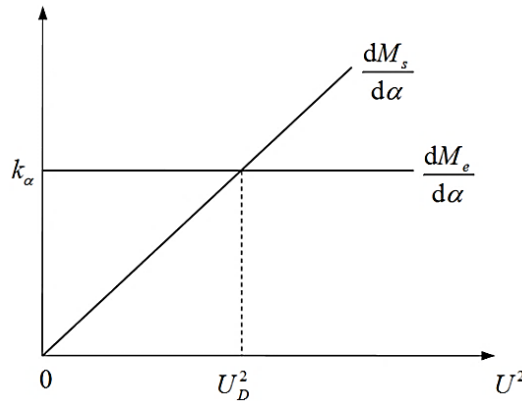


Figure 2-8: Graphical representation of the stability field for torsional divergence [46]

2.2 Two-degree of freedom flutter analysis

The well-known collapse of the Tacoma Narrows Bridge in 1940 undoubtedly served as a catalyst for research into the phenomenon of flutter instability in structural engineering. Experimental and analytical techniques are combined to examine this physical phenomenon, which has its roots in aeronautical engineering. The analysis's goal is to identify the lowest wind speed, which varies with angle of attack, that causes deck instability for the established configuration. This wind speed must be effectively exceeding the wind speeds determined by meteorology at the bridge site to ensure structural safety. Researchers found it possible to apply the analyses created on aircraft wings to the deck sections of suspension bridges to perform aeroelastic instability analyses and comprehend the circumstances under which flutter occurs after conducting numerous studies in the aeronautical field.

The flutter phenomenon is a type of dynamic instability that develops when elastic, inertial, and self-excited aerodynamic forces interact reciprocally. At a certain wind speed, the structure oscillates in a divergent and destructive way.

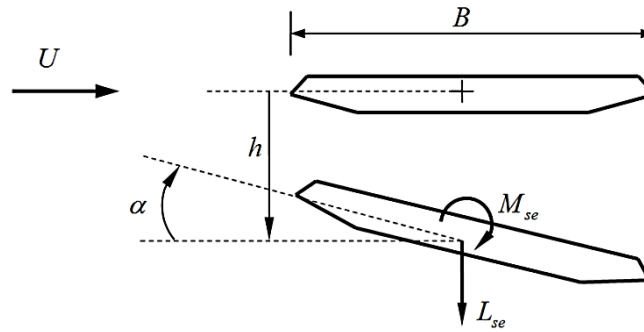


Figure 2-9: Two-degree-of-freedom model [45]

In this simplified two-degree-of-freedom (two-DOF) model, shown in Figure 2-9, only the vertical deflection (h) and the torsional rotation (α) are taken into consideration as they reflect the self-excited aerodynamic forces acting on a deck subjected to a constant wind flow (U). Due to the drag force's connection to the horizontal sway (p), which leads to lateral-torsional instability, this variable is not taken into account. The unsteady aerodynamic forces acting on the oscillating bridge decks cannot be expressed in a closed-form formula. A semiempirical model based on the so-called *flutter derivatives*, which are experimentally established in wind tunnels, was proposed by *Scanlan and Tomko* [47] as a solution to the issue. It is possible to assume that the *self-exciting forces* are linear functions of structural displacements and velocities, parametrically dependent on the *reduced frequency of oscillation* K , and assuming expressions in h and α coordinates:

$$L_{se}(t, K) = \frac{1}{2} \rho U^2 B \left[K H_1^*(K) \frac{\dot{h}(t)}{U} + K H_2^*(K) \frac{B \dot{\alpha}(t)}{U} + K^2 H_3^*(K) \alpha(t) + K^2 H_4^*(K) \frac{h(t)}{B} \right] \quad (2-13)$$

$$M_{se}(t, K) = \frac{1}{2} \rho U^2 B^2 \left[K A_1^*(K) \frac{\dot{h}(t)}{U} + K A_2^*(K) \frac{B \dot{\alpha}(t)}{U} + K^2 A_3^*(K) \alpha(t) + K^2 A_4^*(K) \frac{h(t)}{B} \right] \quad (2-14)$$

where:

- ω : angular frequency of oscillation [rad/s];
- $H_i^*(K), A_i^*(K)$: *flutter derivatives* obtained in wind tunnel ($i = 1 - 4$);
- $K = \omega B / U = 2\pi f B / U$: reduced frequency of oscillation.



Aerodynamic stiffness and *aerodynamic damping* are depicted by coefficients that multiply generalized *displacements* and generalized *velocities*, respectively. Additional mass terms in $\ddot{h}(t)$ and $\ddot{\alpha}(t)$ are implied in Equations 2-13 and 2-14 but are not explicitly included because they are thought to be meaningless in applications for wind engineering studies.

The Figure 2-10 below shows *Scanlan's* experimental data for the determination of flutter derivatives in a wind tunnel for different bridge decks [48].

The *reduced velocity* U_r is typically used to plot the *flutter derivatives*.

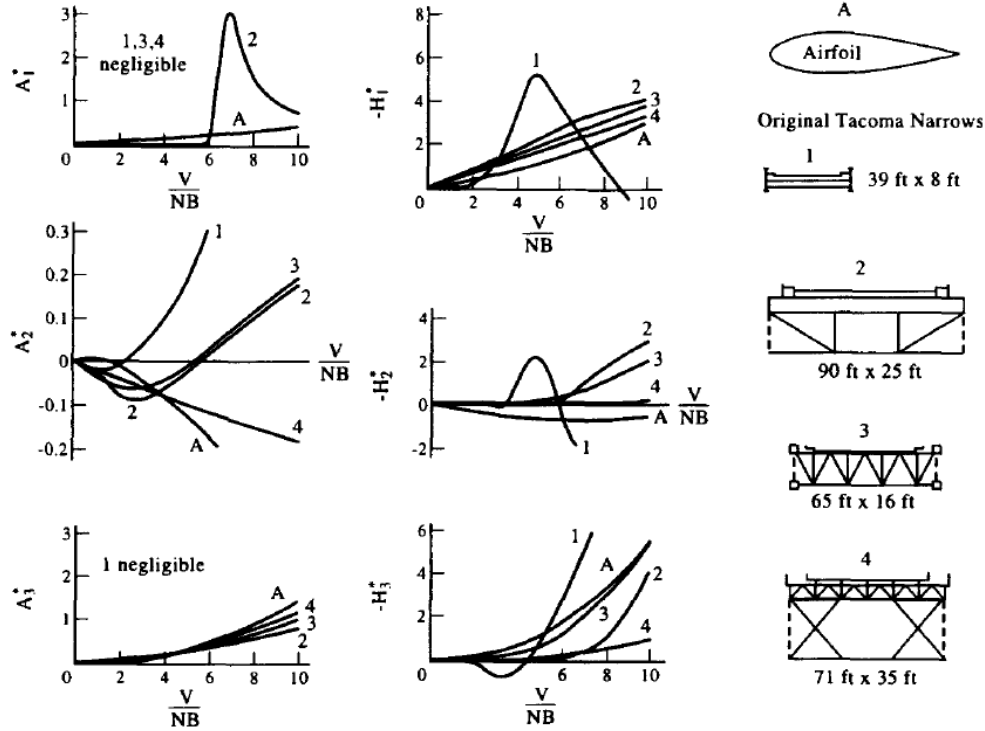


Figure 2-10: Examples of flutter derivatives [45] [48]

$$U_r = \frac{U}{fB} = \frac{2\pi}{K} \quad (2-15)$$

Traditional flutter analysis formulations begin with the premise that bi-dimensional calculations of the transversal section of the deck can be used to evaluate the interaction between wind and structure, making tri-dimensional effects insignificant. Modelling the structure as a damped linear oscillator with two degrees of freedom allows for the assumption that small oscillations will disturb the flow [45]. This means that two degrees of freedom, vertical translation, defined by h displacement, and rotation, defined by α , can be considered in the plane to which the section belongs. The *equations of motion* for the two-degree-of-freedom model can be expressed in the following ways based on these robust calculation assumptions:

$$m\ddot{h}(t) + c_h\dot{h}(t) + k_h h(t) = L_{se}(t, K) \quad (2-16)$$

$$I\ddot{\alpha}(t) + c_\alpha\dot{\alpha}(t) + k_\alpha \alpha(t) = M_{se}(t, K) \quad (2-17)$$

where:

- h and α are the vertical bending and the torsional angle;
- m : deck mass per unit length [kg/m];
- I : deck polar mass moment of inertia per unit length [kgm^2/m];
- c_α, c_h : mechanical viscous damping factors;
- k_α, k_h : elastic stiffness factors in the heaving and pitching modes, respectively.



- L_{se}, M_{se} : self-excited lift and moment per unit length, depending on *time* t and the *reduced frequency* K . Forces that are orthogonal to the direction of the wind and the aerodynamic moment on the section are known to be *unsteady aerodynamic forces*. These variables depend on the section bridge displacement in a flutter analysis.

Knowing the forces L_{se}, M_{se} the flutter critical wind speed can be obtained.

The two-degree-of-freedom aerodynamic instability, or more commonly known as the *classical flutter*, is analytically demonstrated by Equations 2-16 and 2-17. With *Prandtl's treatment of lateral torsional buckling* [49], there is an obvious analogy. Since the two equations are interdependent, the problem is coupled, which is why it is sometimes referred to as *coupled flutter*.

The two-DOF (flexural-torsional) flutter is *primarily governed by stiffness (stiffness-driven)*, and it is the phenomenon that typically may occur in *aircraft wings* and *modern long-span bridge decks*.

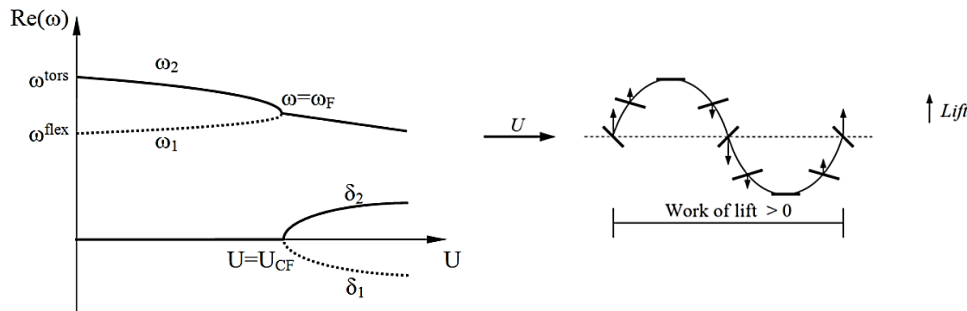


Figure 2-11: Definition of flutter critical speed [46]

As shown in Figure 2-11, the two modes combine to form a single flutter frequency in classical flutter, which causes a motion that provides energy to the system and causes oscillations with a large amplitude. To solve the coupled equations of the system, it is necessary to search harmonic solutions to 2-16 and 2-17 Equations:

$$h(t) = h_0 e^{i\omega t}; \alpha(t) = \alpha_0 e^{i\omega t} \quad (2-18)$$

Using fourth-degree and third-degree polynomial equations with respect to the *reduced frequency* K , whose common solution yields the *critical reduced frequency* for flutter K_F , it is possible to separate the real and imaginary parts of a complex system after the determinant of the system has been set to zero. The frequency ω_F that simultaneously satisfies both polynomial equations in a critical condition is known as the *flutter frequency*. The *flutter speed* can be calculated as follows:

$$U_F = \frac{B\omega_F}{K_F} \quad (2-19)$$

As another option, in analogy with *Ziegler column model* [50], the flutter speed can be calculated using the system's eigenvalues $\omega_n = \omega_{r,n} + i\omega_{j,n}$ (with $n=1,2$) by increasing the wind speed until the damping-related real part reaches zero. The flutter frequency is represented by the real part according to Equation 2-18 [46].

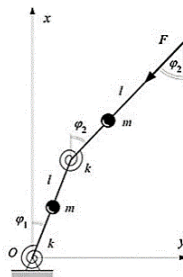


Figure 2-12: Ziegler column model (two-degree-of-freedom system) [5]

2.3 One-degree of freedom flutter analysis

Single-degree-of-freedom flutter (single-DOF), also known as *damping-driven flutter*, is relevant for bridges because it allows for negative damping in a single mode without coupling with any other modes. According to this interpretation, the wind speed needed to produce enough negative aerodynamic damping to cancel out the mechanical damping of the bridge is what causes the first symptoms of the flutter phenomenon [45]. Examining the flutter derivatives, especially A_2^* and H_1^* since they control *torsional flutter* and *vertical flutter (galloping)* respectively, allows one to make an early evaluation of the flutter behavior of the section. These derivatives could be modified to eliminate the positive flutter derivatives as illustrated in Figure 2-10. The total damping coefficients (structural + aerodynamic damping) can be expressed as follows if only the aerodynamic damping terms associated with A_2^* and H_1^* are thought to be significant. Total damping can therefore be written as:

$$c_{h,tot} = c_h - \frac{1}{2} \rho U B K H_1^*(K) \quad (2-20)$$

$$c_{\alpha,tot} = c_{\alpha} - \frac{1}{2} \rho U B^3 K A_2^*(K) \quad (2-21)$$

For vertical and torsional degree of freedom, respectively.

As A_2^* and H_1^* are both negative for every value of K for *aerofoil deck sections*, the total damping is always positive for both h and α . It follows that, in an incompressible flow, the air foil isn't subjected to single-degree-of-freedom flutter in a vertical or torsional mode; in fact, the *classical flutter instability*, which is the critical collapse mechanism, always involves a coupling between these two modes.

On the other hand, the flutter of bridge decks is not always caused by this coupling. *The Tacoma Narrows bridge* (denoted by "1" in Figure 2-13), which collapsed due to a breeze in 1940, has negligible values of the flutter derivative H_1^* (Figure 2-10 and Figure 2-13), which means that vertical flutter (galloping) cannot occur. On the other hand, the value of A_2^* , initially negative, then takes on positive values and as a result the total damping $c_{\alpha,tot}$ becomes negative (dynamic self-excitation) and the torsional flutter phenomenon begins leading to structural collapse. The critical wind speed therefore depends substantially on the value of the mechanical damping c_{α} .

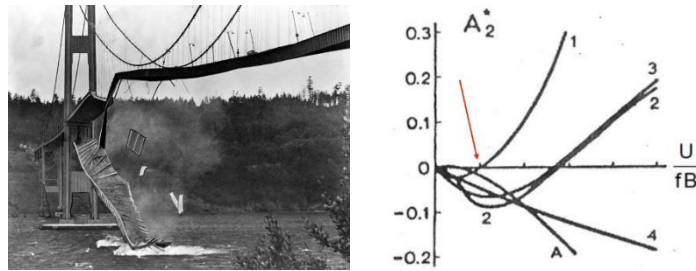


Figure 2-13: Tacoma Narrows Bridge flutter derivatives [46]

Before introducing the simplified resolution of the one-degree-of-freedom flutter, it is necessary to recall the complete *three-degree-of-freedom* sectional model for the bridge deck. In very long-span bridges, the *sway* component of the motion may be relevant for flutter instability [5].

Taking into account the lateral wind force along the longitudinal development of the bridge deck (Drag force, D_{se}) and the associated displacement p , the general aeroelastic motion equation can be written in compact form as:

$$[M]\{\ddot{\delta}\} + [C]\{\dot{\delta}\} + [K]\{\delta\} = \begin{Bmatrix} L_{se} \\ D_{se} \\ M_{se} \end{Bmatrix} = \frac{1}{2} \rho U^2 \left[[F_d]\{\delta\} + \frac{1}{U} [F_v]\{\dot{\delta}\} \right] \quad (2-22)$$



where:

- L_{se}, D_{se}, M_{se} : self-excited lift force, drag force and pitch moment, respectively;

$$\begin{Bmatrix} L_{se} \\ D_{se} \\ M_{se} \end{Bmatrix} = \frac{1}{2} \rho U^2 B \begin{bmatrix} \frac{K^2 H_4^*}{B} & \frac{K^2 H_6^*}{B} & K^2 H_3^* \\ \frac{K^2 P_4^*}{B} & \frac{K^2 P_6^*}{B} & K^2 P_3^* \\ K^2 A_4^* & K^2 A_6^* & K^2 A_3^* B \end{bmatrix} \begin{Bmatrix} h \\ p \\ \alpha \end{Bmatrix} + \begin{bmatrix} \frac{KH_1^*}{U} & \frac{KH_5^*}{U} & \frac{KH_2^* B}{U} \\ \frac{KP_1^*}{U} & \frac{KP_5^*}{U} & \frac{KP_2^* B}{U} \\ \frac{KA_1^* B}{U} & \frac{KA_5^* B}{U} & \frac{KA_2^* B^2}{U} \end{bmatrix} \begin{Bmatrix} \dot{h} \\ \dot{p} \\ \dot{\alpha} \end{Bmatrix} \quad (2-23)$$

- $\delta = \delta(h, p, \alpha)$: displacements vector, function of h , p and α which are the displacements at the center of the deck section in the directions corresponding to L_{se} , D_{se} and M_{se} , respectively;
- $[F_d], [F_v]$: flutter derivatives matrices corresponding to displacement and velocity, respectively.

In liner analysis, the general aeroelastic motion equations of bridge system are expressed in terms of the generalized modal coordinate vector $\{\delta\}$:

$$[M]\{\ddot{\delta}\} + \left([C] - \frac{1}{2}\rho U[C^*]\right)\{\dot{\delta}\} + \left([K] - \frac{1}{2}\rho U^2[K^*]\right)\{\delta\} = \{0\} \quad (2-24)$$

where:

- $[M], [C], [K]$: generalized mass, damping and stiffness matrices, respectively;
- $[C^*], [K^*]$: generalized aerodynamic damping and aerodynamic stiffness matrices, respectively.

Matrix $[C^*]$ and matrix $[K^*]$, which correspond to $[F_v]$ and $[F_d]$ in Equation 2-22, respectively, are assembled from local aerodynamic forces. Matrices $[M], [C]$ and $[K]$ are derived in the same manner as in the classical dynamic analysis.

The subsequent characteristic problem is obtained by assuming harmonic oscillation of the form:

$$\{\delta\} = \{\delta_0\}e^{i\omega t} \quad (2-25)$$

which makes it possible to switch from a differential to an algebraic problem.

$$\left(-\omega^2[M] + i\omega\left([C] - \frac{1}{2}\rho U[C^*]\right) + [K] - \frac{1}{2}\rho U^2[K^*]\right)\{\delta_0\} = \{0\} \quad (2-26)$$

Following the application of the eigenvalues' problem, by setting the determinant of the overall matrix of the system equal to zero, the critical value couple (U_F, ω_F) is achieved. Overall, in a n -degree-of-freedom system, n pairs of values $(U_F, \omega_F)_i$ with $i = 1, \dots, n$ are obtained; the flutter couple (U_F, ω_F) is the smallest one. Dedicated numerical procedure, allows to solve Equation 2-26 efficiently, such as the pK - F method, developed by A.Namini and P.Albrecht [51]. The one-degree-of-freedom flutter method expressed by Equations 2-20 and 2-21, can also be applied in Finite Element Framework, as illustrated in Carpinteri's treatment [45]. The uncoupled single-degree-of-freedom flutter can be analyzed as follows, by pre and post multiplying Equation 2-26 by the eigenvector $\{\delta_{0,j}\}$ related to the j^{th} mode:

$$\{\delta_{0,j}\}^T \left(-\omega^2[M] + i\omega\left([C] - \frac{1}{2}\rho U[C^*]\right) + [K] - \frac{1}{2}\rho U^2[K^*]\right)\{\delta_{0,j}\} = 0 \quad (2-27)$$

which reduces to the following uncoupled equation for mode j to a scalar equation:

$$-\omega^2 m_j + i\omega\left(c_j - \frac{1}{2}\rho U c_j^*\right) + k_j - \frac{1}{2}\rho U^2 k_j^* = 0 \quad (2-28)$$



Equalizing the total damping to zero gives the *critical couple* for the j^{th} mode:

$$U_{F,j} = \frac{2c_j}{\rho c_j^*}; \quad \omega_{F,j}^2 = \frac{k_j - \frac{1}{2}\rho U_{F,j}^2 k_j^*}{m_j} \quad (2-29)$$

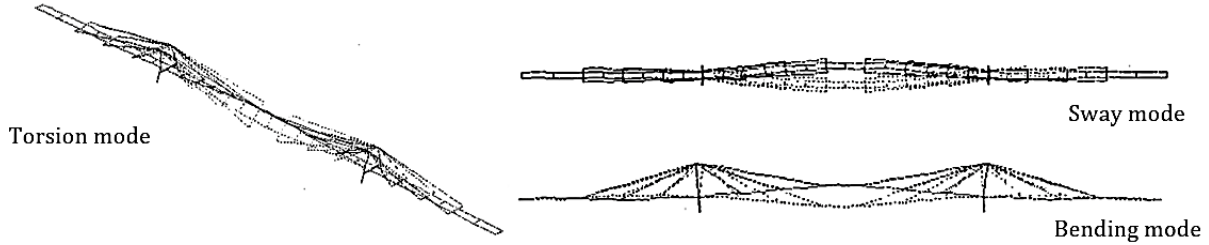


Figure 2-14: Fundamental modes (1DOF): Torsion, Vertical Bending and Sway mode [51]

2.4 Numerical flutter assessment in ANSYS

Flutter, a dynamic instability phenomenon where the bridge oscillates in a divergent and destructive manner at a critical wind velocity, is the most hazardous of the various aeroelastic instabilities.

Flutter instability is prohibitive during the design of long-span bridges, and the critical flutter wind velocity of a bridge must exceed the design value. Flutter analysis is meant to predict the *lowest critical wind speed* that causes flutter instability as well as the associated *flutter frequency*.

The FE ANSYS commercial package offers users particular tools to modify and enhance its preexisting capabilities. The specific tool of the commercial software known as APDL (ANSYS Parametric Design Language), which enables straightforward consideration of several non-linear characteristics of suspension bridges, is used in this thesis to perform flutter analyses with numerical finite element models. Due to hangers and main cables, this type of structure exhibits non-linear geometric behavior: as the load increases, the main cable tension increases and the stiffness increases. Thus, an additional increase in load corresponds to a smaller increase in displacements. Pre-stressing effects from pre-tensioning were incorporated into the modal analyses to account for this non-linear behavior. The software makes it simple to do this by allowing the use of specific calculation requirements.

The model, developed by Chinese researchers *X.G. Hua* and *Z.Q. Chen* in 2008 [52] and first presented in 2007 [53], proposes a first method to analyze *coupled flutter of long-span bridges* and then a full-order approach to analyze coupled flutter by using *flutter derivatives* measured from wind tunnel tests on sectional bridge models. The approach is briefly described below and is based on the definition of aeroelastic loads using a specific user-defined element in ANSYS, namely *Matrix27*.

The *aeroelastic stiffness* and *damping matrices* in *Matrix27* elements are derived and expressed in terms of the flutter derivatives, using either a lumped or consistent formulation. The following two references [54] and [55] provide examples of this developed analysis: In order to identify the real and imaginary components of the complex eigenvalues, analysis of the damped eigenvalues is then carried out with respect to the integrated system of the structure incorporating a set of *Matrix27* elements.

At a certain *wind speed*, the system must have a complex eigenvalue with a *real part that is zero or close to zero* and an imaginary part that is equal to the *flutter frequency* for the first signs of flutter instability. A bridge section's *equation of motion* in a smooth flow is expressed as follows:

$$M\ddot{X} + C\dot{X} + KX = F_{ae} \quad (2-30)$$



where:

- M is the global mass matrix;
- C is the damping matrix;
- K is the stiffness matrix;
- \ddot{X} is the acceleration vector,
- \dot{X} is the velocity vector,
- X is the displacement vector,
- F_{ae} is the aeroelastic nodal forces vector.

The equivalent nodal loading for a bridge girder is calculated by converting the distributed aeroelastic forces acting on a generic element into equivalent nodal loads acting on *the ends of the element*:

$$F_{ae}^e = K_{ae}^e X^e + C_{ae}^e \dot{X}^e \quad (2-31)$$

where K_{ae}^e and C_{ae}^e are, respectively, the *local* aeroelastic stiffness and damping matrices of element e . A lumped formulation of them is as follows:

$$K_{ae}^e = \begin{bmatrix} K_{ae1}^e & 0 \\ 0 & K_{ae1}^e \end{bmatrix} \quad (2-32)$$

$$C_{ae}^e = \begin{bmatrix} C_{ae1}^e & 0 \\ 0 & C_{ae1}^e \end{bmatrix} \quad (2-33)$$

$$K_{ae1}^e = a \begin{bmatrix} 0 & 0 & 0 & 0 & 0 & 0 \\ 0 & P_6^* & P_4^* & BP_3^* & 0 & 0 \\ 0 & H_6^* & H_4^* & BH_3^* & 0 & 0 \\ 0 & BA_6^* & BA_4^* & B^2 A_3^* & 0 & 0 \\ 0 & 0 & 0 & 0 & 0 & 0 \\ 0 & 0 & 0 & 0 & 0 & 0 \end{bmatrix} \quad C_{ae1}^e = b \begin{bmatrix} 0 & 0 & 0 & 0 & 0 & 0 \\ 0 & P_5^* & P_1^* & BP_2^* & 0 & 0 \\ 0 & H_5^* & H_1^* & BH_2^* & 0 & 0 \\ 0 & BA_5^* & BA_1^* & B^2 A_2^* & 0 & 0 \\ 0 & 0 & 0 & 0 & 0 & 0 \\ 0 & 0 & 0 & 0 & 0 & 0 \end{bmatrix} \quad (2-34) \quad (2-35)$$

where $a = \rho U^2 K^2 L_e / 2$ and $b = \rho U B K L_e / 2$; B is deck's width and L_e is the length of the element e .

The ANSYS Matrix27 user-defined element is an adaptable element with two nodes that each have six degrees of freedom and whose local coordinate system matches the global coordinate system. The stiffness, mass, and damping coefficients define the element's properties, while the element's geometric configuration is arbitrary. Due to the motion-dependent nature of aeroelastic forces, the Matrix27 element must be used to represent the fundamental stiffness and damping matrices. As a way to simulate the aeroelastic forces, two Matrix27 elements are attached to each node of a generic bridge deck *hybrid element model*, as shown in Figure 2-15. *The element can only model either an aeroelastic stiffness matrix or an aeroelastic damping matrix, but not both simultaneously.*

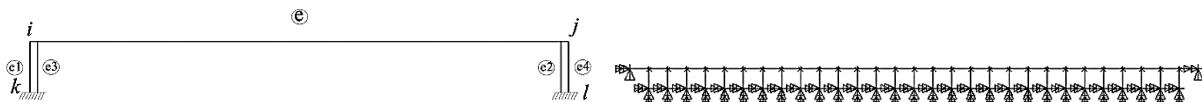


Figure 2-15: Hybrid finite element model for flutter analysis in ANSYS [53]

The aeroelastic stiffness and damping of the node i are represented by the Matrix27 elements e_1 and e_3 after defining the fictitious node k while the node j is represented by the Matrix27 elements e_2 and e_4 after defining the fictitious node l , respectively. The element matrices are made simpler if all of the bridge deck elements have the same length.



In a general case, element matrices are defined as:

$$K^{e1} = K_{ae}^{e-1} + K_{ae}^e \quad K^{e2} = K_{ae}^e + K_{ae}^{e+1} \quad (2-36) \quad (2-37)$$

$$C^{e3} = C_{ae}^{e-1} + C_{ae}^e \quad C^{e4} = C_{ae}^e + C_{ae}^{e+1} \quad (2-38) \quad (2-39)$$

Assembling all elemental matrices into a *global* aeroelastic stiffness and damping matrices leads to:

$$F_{ae} = K_{ae}X + C_{ae}\dot{X} \quad (2-40)$$

where K_{ae} and C_{ae} denote the *global aeroelastic stiffness* and *damping matrices*, respectively.

The mathematical model of an integrated system is obtained by substituting Equation 2-40 into 2-30, with the effect of aeroelasticity parametrized by wind velocity and vibration frequency through the incorporation of Matrix 27 user-defined elements. The *global equation of motion* is expressed as:

$$M\ddot{X} + (C - C_{ae})\dot{X} + (K - K_{ae})X = 0 \quad (2-41)$$

Damped complex eigenvalue analysis can be implemented with Equation 2-41 to identify the properties of the parameterized system. A *superposition* of the first m conjugate pairs of complex eigenvalues and eigenvectors can be used to approximate the dynamic response of the system, as

$$X = \sum_{j=1}^m \phi_j e^{\lambda_j t} \quad (2-42)$$

where $\phi_j = p_j \pm iq_j$ is the j^{th} complex conjugate pair of *eigenvectors*; $\lambda_j = \sigma_j \pm i\omega_j$ is the j^{th} conjugate pair of complex *eigenvalues*; and $i = \sqrt{-1}$.

When all of the system's eigenvalues' real parts are negative, the system is said to be dynamically stable. If any eigenvalues' real parts are positive, however, the system is said to be unstable.

The critical flutter speed U_f is then determined by the wind speed, and the imaginary part of the complex eigenvalue λ_f , which corresponds to the *critical flutter speed*, becomes the *flutter frequency*. This is how the flutter condition is then determined. For large structures with thousands of degrees of freedom, like *long-span suspension bridges*, only the first eigenvalues are necessary for the assessment of complex eigenvalues because flutter always occurs in real structures with the lowest flutter wind speed, which corresponds to the low-order eigenvalues.



Algorithm implementation in ANSYS

The *wind velocity*, *response frequency*, and *reduced frequency* are the three parameters used to express the aeroelastic stiffness and damping matrices in Matrix 27 elements, but only two of them are independent. The complex eigenvalue analysis requires the variation of both wind velocity and response vibration frequency, so a *mode-by-mode tracing method* [56] is used to iteratively search the flutter frequency and the flutter velocity. The ANSYS procedure of flutter analysis is summarized in some steps:

- I. Develop a *finite element model* for the original structure lacking Matrix27 elements, carry out a modal analysis that takes permanent loads into account, and calculate the first m natural modes ω_i^0 ($i = 1, 2, \dots, m$);
- II. Upgrade the FE model to *hybrid* with the *introduction of Matrix27 elements*, in which the flutter derivatives are inputted step by step in ANSYS procedure;
- III. Set an initial wind velocity U_0 and its increment ΔU ;
- IV. Let the initial oscillation frequency ω_0 be the frequency ω_i^0 of each natural mode in turn;
- V. Identify the aeroelastic stiffness and damping matrices in the MATRIX27 elements at the current iteration, as well as the reduced wind velocity U_r , before performing the *damped complex eigenvalue analysis*;
- VI. Compare the imaginary part of the i^{th} computed complex eigenvalue λ_i with ω_0 with each step. If inequality (2-43) is fulfilled repeat step IV to VI, otherwise go to step VII;

$$\left| \frac{Im(\lambda_i) - \omega_0}{Im(\lambda_i)} \right| > \varepsilon \rightarrow \text{let } \omega_0 = Im(\lambda_i) \quad (2-43)$$

- VII. If the procedure reaches convergence ($< \varepsilon$), repeat steps III to VI for all the *range of interest of wind velocity* to obtain the variation of m pairs of complex eigenvalues with wind velocity.

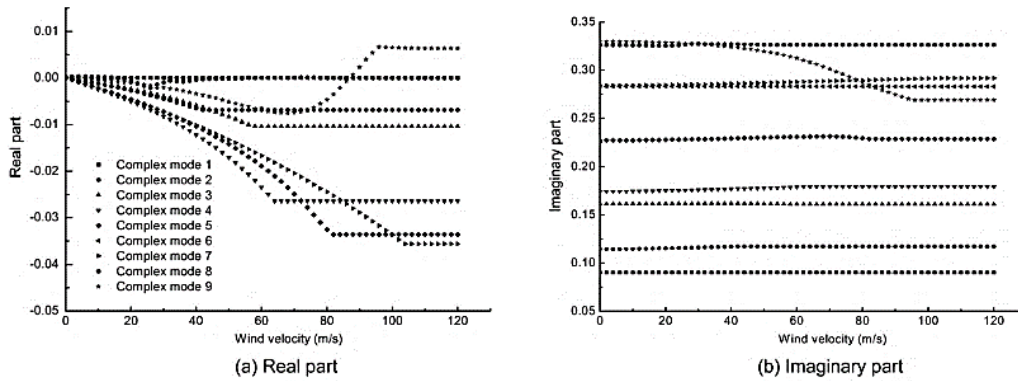


Figure 2-16: Example of Flutter analysis result [52]

Incorporation of mechanical damping

By assuming the Rayleigh damping matrix, the mechanical damping of a structure is typically expressed in terms of modal damping ratios.

$$C = \alpha M + \beta K \quad (2-44)$$

where α and β are proportionality coefficients.

The governing equation of motion for damped flutter analysis becomes:

$$M\ddot{X} + (\bar{C} - \bar{C}_{ae})\dot{X} + (K - K_{ae})X = 0 \quad (2-45)$$

where the *modified damping matrix* \bar{C} and the *modified aeroelastic damping matrix* \bar{C}_{ae} are expressed as:

$$\bar{C} = \alpha M + \beta(K - K_{ae}) \quad \bar{C}_{ae} = C_{ae} + \beta K_{ae} \quad (2-46) \quad (2-47)$$

2.5 Analytical flutter assessment in MATLAB

The dynamic system generated by the interaction between the deck of the long-span bridge and the wind, representing self-excited aerodynamic forces, is identified as a non-proportionally damped dynamic system in which damping and stiffness are influenced by the wind load and oscillation frequency. A *multimodal aeroelastic analysis*, including aerostatic nonlinearities, is performed on a *one-dimensional continuum model* of the suspension bridge for the flutter analysis using MATLAB software.

$$\mu_g \frac{\partial^2 v(z, t)}{\partial t^2} + c_v \frac{\partial v(z, t)}{\partial t} + EI_x \frac{\partial^4 v(z, t)}{\partial z^4} - H \frac{\partial^2 v(z, t)}{\partial z^2} + \frac{\partial^2 (m_y(z) \vartheta(z, t))}{\partial z^2} + \left(\frac{8f}{l} \right)^2 \frac{E_c A_c}{L_c} \int_0^l v(z, t) dz = L_{se} \quad (2-48)$$

$$I_\vartheta \frac{\partial^2 \vartheta(z, t)}{\partial t^2} + c_\vartheta \frac{\partial \vartheta(z, t)}{\partial t} + EI_\omega \frac{\partial^4 \vartheta(z, t)}{\partial z^4} - (GI_t + Hb^2) \frac{\partial^2 \vartheta(z, t)}{\partial z^2} + m_y(z) \frac{\partial^2 v(z, t)}{\partial z^2} + b^2 \left(\frac{8f}{l} \right)^2 \frac{E_c A_c}{L_c} \int_0^l \vartheta(z, t) dz = M_{se} \quad (2-49)$$

Where:

- v and ϑ are the vertical and torsional displacement of the deck cross-section;
- μ_g and I_ϑ are the bridge mass and mass moment of inertia per unit length;
- $c_v = 2\mu_g \xi_v \omega_v$ and $c_\vartheta = 2I_\vartheta \xi_\vartheta \omega_\vartheta$ are *damping coefficients*, being ξ_v, ξ_ϑ and $\omega_v, \omega_\vartheta$ damping ratios and angular frequencies;
- EI_x, EI_ω, GI_t are the *vertical bending rigidity, warping and primary torsional rigidity*, respectively;
- H is the horizontal component of the main cables tension; l is the main span length; b is half the distance between cables;
- f, A_c, L_c and E_c are the cable sag, cross-section area, length and Young modulus;
- L_{se}, M_{se} are the *aeroelastic self-excited lift and moment*;
- $m_y(z)$ is the horizontal bending moment due to the steady drag force.

Equations 2-48 and 2-49 [57], which are based on classical linearized theory but are improved by including wind-related geometric nonlinearities, such as stiffening/softening caused by the lift force and a second-order Prandtl-like effect caused by the drag force, govern the vertical and torsional oscillations of a suspension bridge subjected to aeroelastic loads. In [58] and [59], this procedure was first implemented.

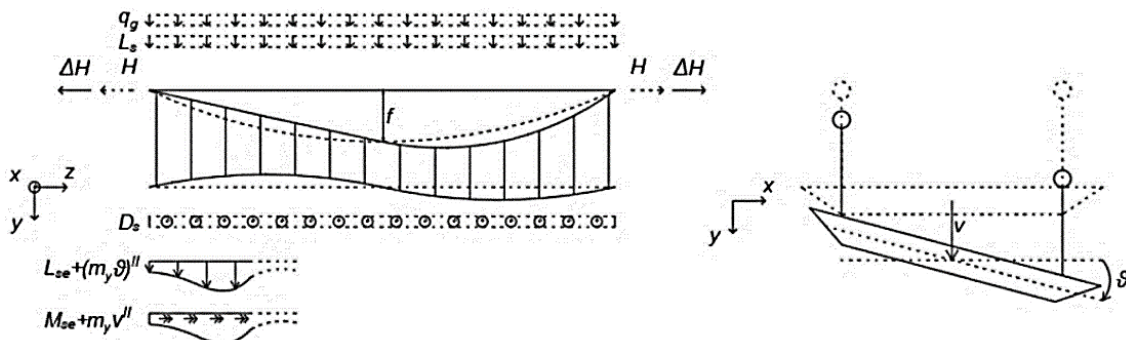


Figure 2-17: Perturbated configuration of 1D continuum model [59]



Differential Equations (2-48, 2-49) account for aeroelastic nonlinearities. These equations state that the projection of the horizontal bending moment in the perturbed configuration results in additional (2nd order) terms that have geometric nonlinearities and affect the vertical and torsional equilibrium (Figure 2-17). Analyzing the multimodal framework, the solution of differential equations can be considered in *harmonic form*.

$$v(z, t) = \bar{v}(z)e^{\lambda t}; \quad \vartheta(z, t) = \bar{\vartheta}(z)e^{\lambda t} \quad (2-50)$$

Weighted sums of sinusoids with varying wavelengths are used to represent the spatial functions:

$$\bar{v}(z) = b \sum_{j=1}^n a_{v_j} \sin\left(\frac{j\pi z}{l}\right) \quad (2-51)$$

$$\bar{\vartheta}(z) = \sum_{k=1}^m a_{\vartheta_k} \sin\left(\frac{k\pi z}{l}\right) \quad (2-52)$$

A quadratic eigenvalue problem, of $N = n + m$ equations, is obtained for the unknowns a_{v_j} and a_{ϑ_k} , by applying *Galerkin method*:

$$[A(\lambda, U)]\{a_{v,\vartheta}\} = \{0\} \quad (2-53)$$

The eigenvalues and eigenvectors of the quadratic eigenvalue problem represented by Equation 2-53 with the notation $r \in [1; 2N]$ are the eigenvalues λ_r and eigenvectors $\{a_{v,\vartheta}\}_r$ identifying various vibration modes.

When the $2N$ independent eigensolutions are combined linearly, the answer to Equation 2-53 can be written as follows:

$$V(x, t) = \sum_{r=1}^{2N} v_r(z) e^{\lambda_r t} \quad (2-54)$$

$$T(x, t) = \sum_{r=1}^{2N} \vartheta_r(z) e^{\lambda_r t} \quad (2-55)$$

where, for each of the different eigenvectors, Equations 2-54 and 2-55 are used to calculate the vertical and torsional components ($v_r(z)$ and $\vartheta_r(z)$, respectively) of the r^{th} eigen-solution. It is also possible to write the corresponding eigenvector components in polar form by defining the pair of complex conjugate eigenvalues as $\lambda_r = \mu_r + i\omega_r$.

The sum of r modal contributions, each of which is defined by the sum of $N = n + m$ harmonic functions, is used to express the vertical and torsional displacements. The modal frequency is represented by the imaginary part of the eigenvalues, while the real component controls the exponential trend of the modal contributions. The system is unstable and will diverge exponentially with increasing time if the real part of an eigenvalue becomes positive.

A complex eigenvalue analysis is carried out for each step of the wind speed, taking into account the step value, to examine the variation in natural frequencies and the corresponding modal shape. The eigenvalue violates the stability condition when the *real part is null*, and the corresponding wind speed is the *critical velocity*.



CHAPTER 3 Innovations of 1915Çanakkale bridge

Knowing some elements of contemporary Turkish history and the symbolism the structure conceals in its parts with significant historical allusions to the past of the Ottoman Empire will help in better understanding the design choices made for the record suspension bridge over the Dardanelles Strait.

More than 3000 kilometers separate Belgrade from Baghdad, but at the start of the 20th century, traveling between those two cities via Constantinople, now Istanbul, allowed travelers to stay within the same vast empire, the Ottoman Empire. But by the middle of the 19th century, it started to lose territory and show signs of crisis, and by the start of World War I, it was in serious trouble. Following the war against the Russian Tsarist Empire that began in 1878, some European nations that had been ruled by Turkey gained their independence, including Serbia, Montenegro, and Bosnia-Herzegovina. This significant territorial loss did not stop at the close of the 19th century; rather, it picked up again and got worse at the start of the 20th. The war with Italy for control of Libya in 1911 further weakened the Ottoman Empire, which lost further territories and by the end of 1913 its territorial extension had shrunk by a third compared to the territories it controlled at the beginning of the 20th century.

In the early years of the 20th century, the 'Young Turks' came to power with the aim of modernizing and completing the westernization process of the empire that had begun in the late 1700s [60]. This movement intended to revolutionize the entire alliance system of the empire's old system of government. By August 1914, the Great War had already begun in Europe. The Ottoman Empire had long been on very good terms with Great Britain, which had helped the sultan in 1839 to contain the revolts in Egypt and to limit the entry of the tsarist empire into the Mediterranean territories. The new Turkish government began to forge relations with the German Empire, which had expansionist aims in the East and would help the Ottoman Empire contain Russian expansion to the West. In October 1914, the Ottoman Empire abandoned neutrality in the global conflict and sided with the Germans. On 28 October 1914 Turkish ships began the bombardment of the Russian port of Odessa: Ottoman Empire officially entered the war with Great Britain, France and Russia and was forced to wage war on several fronts against these three great industrialized nations.

The *Gallipoli campaign* (Figure 3-1), also known as the *Battle of Çanakkale*, was a military campaign conducted by the Triple Entente to reinforce the Dardanelles Strait and occupy Constantinople via the Sea of Marmara. The first amphibious landing in history was a military failure of the alliance of Britain and France who were repeatedly defeated by the Ottoman Empire between February and April 1915 on the shores of Çanakkale. The *victory of Çanakkale* on 18 March 1915 and the resistance of the imperial army, led by *Mustafa Kemal*, is regarded as the event that would give rise to the Turkish nationalist renaissance and lead to the birth of modern Turkey in the following years. In 1918, the empire emerged heavily defeated and reduced in size from the world conflict, but for the Turks the war will not end in 1918 but only in 1923. Nationalist revenge began with the entrusting of the army to General Mustafa Kemal, who liberated the Turkish territories occupied by Greece between 1921 and 1923. In October 1923, the sultanate was abolished and the Republic proclaimed: Kemal was appointed president with the nickname *Ataturk*, i.e. 'father of the Turks'. Thus, Turkey was born, a national, non-religious and republican state.

For these purely cultural reasons related to Turkey's modern history, it is possible to find in some aspects of the bridge's design and dimensions a *strong symbolism* and sense of mutual belonging between this important structure and the Turkish nation.

This historical link between the *1915Çanakkale Bridge* and Turkey's history can be seen in the timing of construction, the towers' height, and the record size of the main span.



The 1915Çanakkale Bridge is inaugurated in March 2022, after about 4 years of intensive construction work, bringing forward by more than a year the bridge's completion date, which was set for October 2023, the date on which it would commemorate 100 years of the Turkish Republic. Specifically, the opening to traffic takes place on March 18, 2022 (3.18) reminding the nation of one of the historic dates for the country, namely the victory over Britain and France on March 18, 1915 (a year also captured in the name of the bridge itself). The date 3.18 is also carried over into the height of the towers: with 318 m, the world record for tower height for suspension bridges is won.

The province of Çanakkale in northwest Turkey is home to the 1915Çanakkale Bridge, which is also the country's first suspension bridge over the Dardanelles Strait. It is close to the cities of *Gelibolu (Gallipoli)* in Europe and *Lapseki in Asia*, which are 10 kilometers south of the Sea of Marmara (Figure 3-2) [61]. Two of Turkey's most significant geographic regions, the Aegean and Marmara, can be connected to numerous harbors, railways, and air transportation systems through the suspension bridge project [39]. The bridge is *the longest suspension bridge in the world* with a main span of 2023 meters and two side spans of 770 meters (Figure 3-3). A pair of preformed parallel wire strand (PPWS) cables with a nominal diameter of 0.9 m and vertical hangers spaced every 24 meters make up the cable suspension system [61]. The 318-meter-tall steel towers and the slender deck create a feeling of an extremely light and flexible structure: the deck is composed of two 15 m wide aerofoil orthotropic steel box girders that are separated by a *9 m wide air-gap space*, with a nominal structural depth of 3.5 meters. Full-depth transverse box girders connect them at regular intervals at the hangers' position (24 m) (Figure 3-4).



Figure 3-1: Gallipoli Campaign (Battle of Çanakkale, 1915) [60]

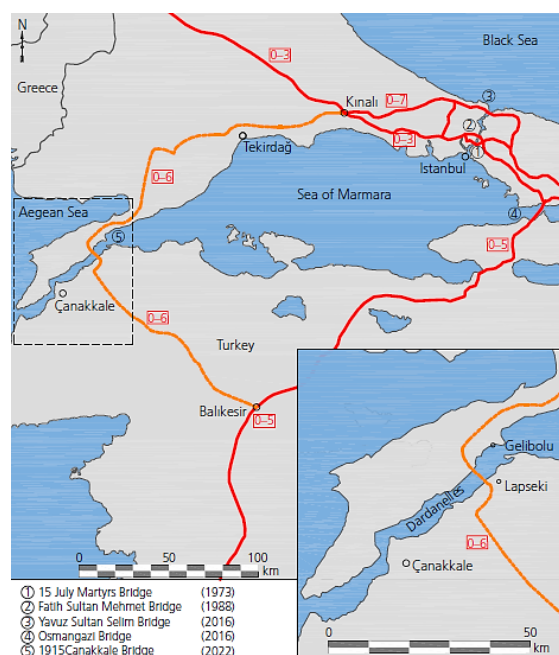


Figure 3-2: Location of 1915Çanakkale bridge [61]

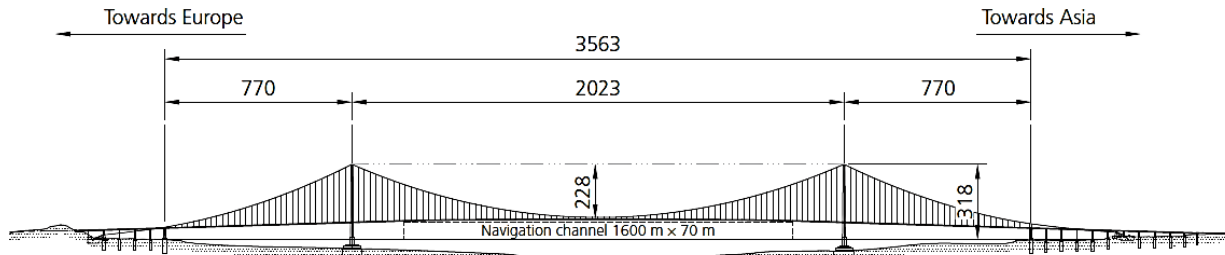


Figure 3-3: Representation of 1915Çanakkale bridge dimensions [61]

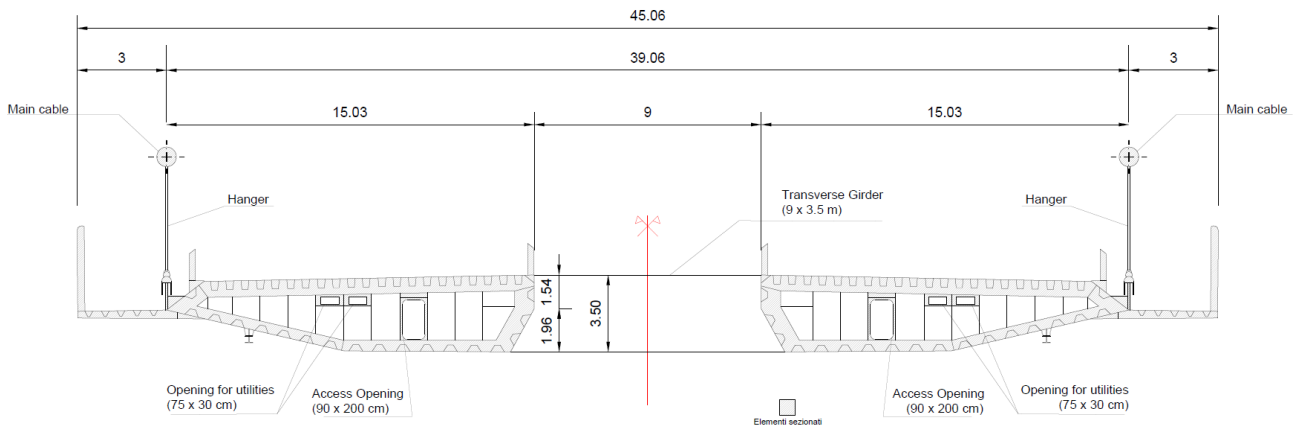


Figure 3-4: 1915Çanakkale bridge's deck cross section

3.1 Construction details and technological innovations

This section of Chapter 3 aims to introduce some innovative aspects of bridge construction and design, which aroused the author's curiosity and desire for further research. These innovations regarding especially the design, construction and assembly of the in-situ *deck*, the proposed peculiarities in the design of the *towers* and *foundations* in a highly seismic zone, the *construction of the main cable*, the *hangers*, and the *anchor blocks*. Further insight is given into the bridge *monitoring system*, one of the most innovative in the world. In conclusion, the curious *hybrid bridge version* of the 1915Çanakkale Bridge with its advantages and disadvantages is also reported.

3.1.1 Deck design, fabrication and erection overview

As indicated in the work of *V. Boteanu* and *J. W. Sørensen* [62], the design of the deck resulted in determining an overall width of the twin-box girder of 45 m with the individual main cables positioned at a distance from each other that includes the two caissons and the air-gap of 9 m.

To reduce the weight of the deck and the space between the main cables, as well as the width of the towers and tower foundations, it is shown in Figure 3-4 that the two maintenance walkways are situated on the exterior of the hangers. The hangers are situated in the same location as the cross beams joining the two longitudinal beams and are spaced 24 m apart in the longitudinal direction.

The twin-box beam's and the connecting transverse beams' suitable depth is 3.5 m. The impact barriers are additionally positioned on devices outside the deck plate, and the hangers' anchors are positioned at the tip of the beam, all of which help to reduce the width of the deck. The box girders have longitudinal stiffeners inside that distribute the load locally between the 4.2 m apart transverse diaphragms. To account for the distance between the webs, this spacing is decreased to 3.0 m at the transverse beams. A "Vierendeel" girder's structural behavior has been shown by the double box girder. The two box girders work only partially together. The tower and cable designs are also affected by this effect [62],



which has an overall impact on the deck deformations. The interaction of the bridge's transverse beam and longitudinal beam also played a role in the necessity of using high-strength S550 steel locally to manage localized stress concentrations.

The deck plate uses a variety of *structural steel* types and ranges in thickness from 8 to 15 mm, depending on the deck's component parts and the *fatigue* verifications carried out during the design phase. S460 steel is used in the tower areas and at the ends of the bridge, where the forces are greatest, to reduce the weight of the twin-box girder. The quality of longitudinal girder steel is typically S355 at other points in the structure.

Through an in-depth fatigue verification fully integrated in IBDAS (COWI's in-house software), using Fatigue Load Model 4 and a locally improved FE model for stress concentration calculations, the bridge deck was optimized while ensuring a 100-year fatigue life. A *semi-local deck model* that was fed into the *global* FE model of IBDAS included the locally refined details for fatigue verification. This enabled the investigation of local effects in particular areas of the deck, such as towers and bridge ends. The Figure 3-5 displays the local model in the semi-local and global models.

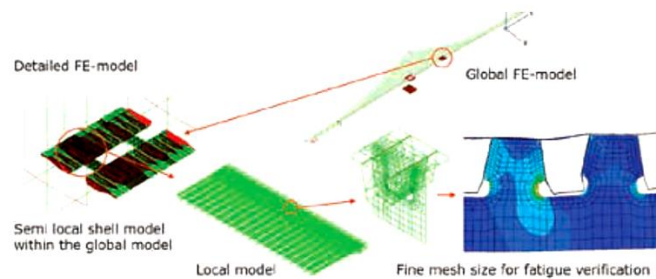


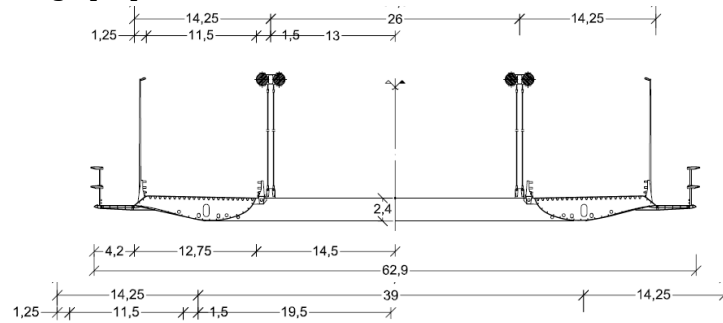
Figure 3-5: Local and global analysis FE-model [62]

The long-discussed design of the Messina Strait Bridge highlighted the great advantage brought by introducing a *wide air-gap* between the deck box girders. This topic is particularly highlighted in the research work of *G. Bartoli* and *P. D'Asdia* [63], which proposes a novel method for designing super long-span suspension bridges. It is possible to develop structural layouts for multi-box decks with ratios between torsional and flexural frequencies (R_{F1}) susceptible to coupling that are less than one, as reported in Equation 3-1. A bridge with these features highlights the possibility of achieving significant construction *cost savings*, which is of primary importance for such structures, in addition to being able to avoid instability phenomena caused by *classical flutter*.

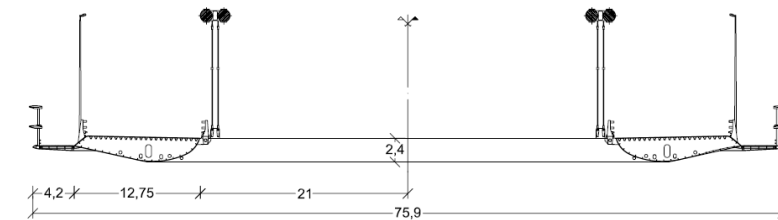
$$R_{F1} = \frac{f_{TORS-SYM}}{f_{VERT-SYM}} \quad (3-1)$$

The stiffness of the suspension cables contributes more as the bridge's span increases than the stiffness of the deck, so the relationship between the first torsional frequency and the corresponding vertical bending frequency tends to a value close to unity. Therefore, where the aerodynamic properties of the section lead to the exclusion of the one-DOF flutter, a classical two-DOF flutter phenomenon may occur. The Italian research group conducted the study of air-gap variation by leaving the design philosophy of the 1992 Messina Bridge unchanged but considering for simplicity only the part of the deck intended for vehicular traffic. As shown in Figure 3-6, three cases are studied with the variation of the distance between the main cables: (a) 26 m, (b) 39 m, (c) 52 m. Examination of the results of R_{F1} shows that, in the absence of wind, bridges with deck (a), (b) and (c), exhibit a frequency ratio of slightly more than one. According to this *G. Bartoli's* paper [63] this circumstance is an advantage of safety against aeroelastic instability due to classical flutter since, as is well known, in the presence of wind, the frequency of the first torsional mode tends to decrease while the flexural mode tends to increase, reducing R_{F1} to values less than one. This is an *idealized* form that prevents classical flutter. Instead, in

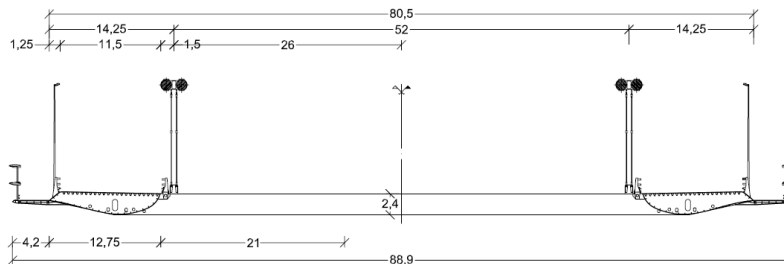
(a)



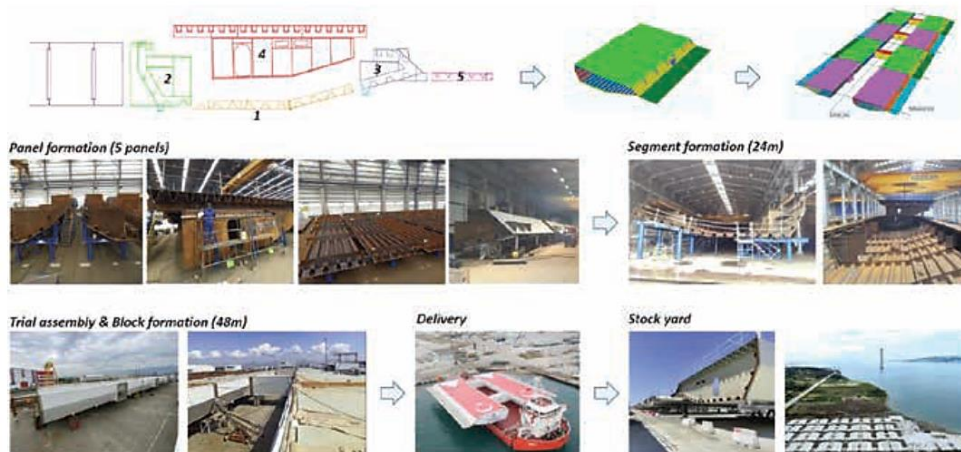
(b)



(c)



Following the design of the aerodynamic shape of the deck, it is beneficial to familiarize oneself with its *fabrication* and subsequent *placement* on the Dardanelles Strait.

Flutter instability of long-span suspension bridges. The case-study of the 1915Çanakkale Bridge in Turkey
Master's Degree in Civil Engineering – Politecnico di Torino – October 2023

A deck structure was developed as an orthotropic steel box, as seen in Figure 3-7. It was divided into five panels in the longitudinal direction, separately manufactured, and finally put together as a single 24-m-long box segment inside the production establishment. Each individual box segment was then painted before being moved to the outdoor yard for block formation and test assembly.

To ensure the necessary geometry, considering the horizontal and longitudinal curvature along the bridge axis, a total of eight 24 m segments and four 9 m transverse beams were placed and aligned on the fabrication yard for a length of 96 m [65].

The deck segments have been manufactured in *Gölcük*, by *Çimtas*, then barged across the Sea of Marmara to the bridge site, where they were stored until the deck was assembled about 4 km from the European cable anchor block. There were *153 deck segments in total*, the majority of which were 24 m long to fit the hanger spacing and ranged in weight from 300 t to 420 t. Ten segments were brought up by a *floating crane* close to the side span piers, and 143 by *lifting gantries* [61].

The main cables support the *lifting gantries*, which are movable devices (Figure 3-8). The *modular truss* between the main cables, a *movement system* supported by the main cables, and a *lifting beam* that attaches to the hanger anchors on the bridge make up the *main components* of the gantries. In particular, 132 bridge segments were welded off-site in pairs, totaling 48 m in length, barged under the lifting gantries, and *lifted in tandem system*. For the *deck erection procedure*, *eight gantries* were needed: two for each side span and four for the main span. Additionally, a single *computerized control system* managed all of the gantry equipment, enabling the simultaneous operation of two to four gantries.

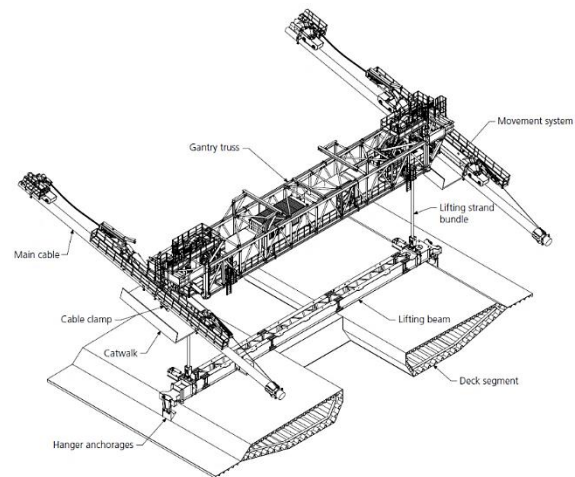
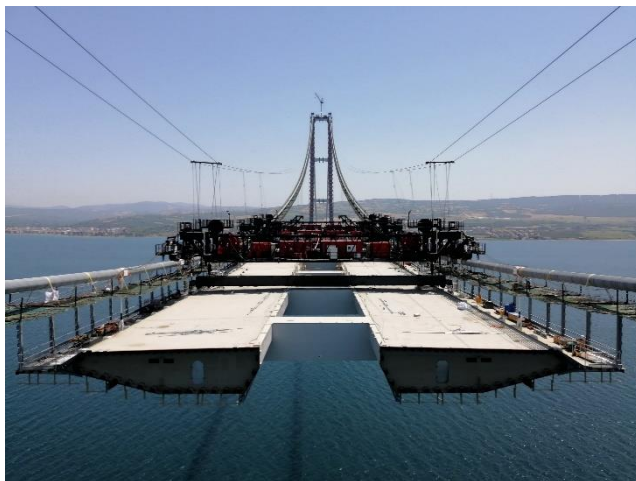


Figure 3-8: Deck lifting gantry general arrangement [42] [61]

The site where the 1915Çanakkale Bridge is located is exposed to *strong winds*. Therefore, the lifting gantries were designed to operate in wind speeds up to 20 m/s to minimize the impact of high winds on the construction program. They are also capable of withstanding wind stresses up to 57 m/s in unloading conditions, defined as parking conditions.

In the work exhibited by *M. Ascaso Til* and *A. Sancho Santamaria* [61], it is highlighted that traditional techniques such as the use of floating cranes for lifting gantries on the main cables have not been used for the lifting stage, but instead an innovative technique called as *self-erection method* is adopted. This newly adopted method brings with it several advantages over traditional techniques.

The self-erection method shows several benefits comparing to the conventional ones: the lifting gantries can be pre-assembled concurrently with cable construction, erected at any time along the main cable, and lifted off the navigation channel in a matter of hours. The self-erect system is a mechanized system made up of a lifting beam assembly that supports two trestles and four jack carriages that are placed at the corners and contain *self-erect strand jacks*. The cable anchors installed on the main cable are connected to the fixed anchor housings of the strand jacks.

The computer control system synchronizes the self-erect strand jacks to within millimeters in order to minimize the difference in elevation between the strand jacks that could result in load variations.

The gantry parts were installed after the self-erect system was assembled at the site stockyard and raised by a crawler crane onto the supports on the barge. After that, the barge was moved below the erection position to start the self-erect process. Large horizontal forces brought on by temperature changes and self-erect system deflection needed to be avoided during assembly because they would compromise the supports' design. The self-erect system interface with the supports was lubricated to reduce friction to mitigate these horizontal forces.

The *self-erect sequence* can be broken down into the following steps: installing the self-erect system on the barge; transporting the barge to the self-erect position during a sea crossing; lifting off from the barge and lifting the self-erect system until main cable level; assembling the gantry; transferring the load to the main cable; and lowering the empty self-erect system to the barge before transporting the barge to the assembly yard [61].

During *site operations*, two self-erect systems were used to speed up the process of installation of the gantries on top of the main cables. To prevent the barge from pitching and rolling excessively due to waves created by passing vessels, the main span navigation channel was closed before the self-erect system was lifted into the air. During the lift-off from the barge procedure, some issues occurred. Depending on the environmental factors, a *dynamic positioning (DP) computer control system* actively corrected the barge position to maintain it stationary within at least a 1 m tolerance. The barge's control system and the self-erect system hanging from the main cables interacted, causing the two objects to move significantly in space and collide until the stabbing guides cleared the bumpers.

The main span was where the deck erection process began, and it moved forward quickly at a rate of up to four tandem lifts per day. The lifting and relocation operations could be carried out in wind speeds of up to 20 m/s and 16 m/s, respectively. High winds in the strait and the operational wind speed limit (16 m/s) for workers on the catwalk-imposed restrictions that slowed down the deck erection process. The *deck erection cycle* could be finished in about 10 hours. The key stages are:

(a) lifting the deck segment off the barge up to final level; (b) temporary connection to the previously erected deck and load transfer onto the hangers; (c) relocating lifting gantries to next lifting position.

The cutting-edge design and control system optimized the movement operations. Between July 20 and September 21, 2021, nearly 3.3 km of deck, including all deck segments save for the tower deck blocks, were built. After welding every joint in the previously constructed deck, the tower deck blocks were constructed in December 2021. A floating crane and temporary hangers were initially intended to be used to erect five deck segments at each tower. However, for these lifts, specialized plans utilizing lifting gantries were developed to do away with the requirement for a floating crane.

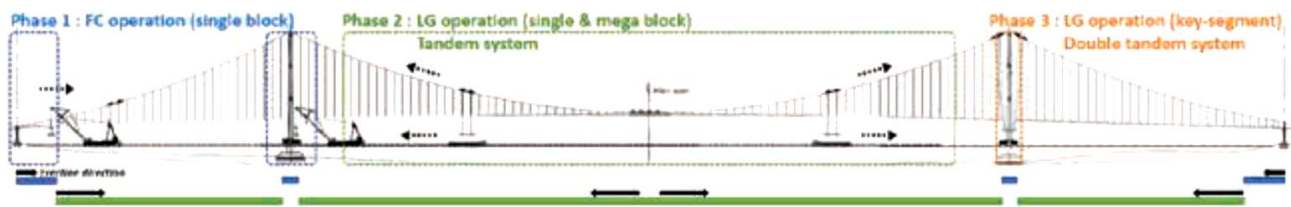


Figure 3-9: Suspension deck erection scheme [65]




<i>Phase 1-Single Block</i>	<i>Phase 2-Double Block</i>	<i>Phase 3-Triple block</i>
15 blocks (L= 24m) Wt. = Max 470 Ton Asian Hercules III (Cap. = 5000 Ton)	66 blocks (L= 48m) Wt. = Max 840 Ton Lifting Gantry (Cap. = 540 Ton) 2EA/block	2 blocks (L= 43.6m) Wt. = 1210 Ton Lifting Gantry (Cap. = 540 Ton) 4EA/block
		
Side spans at bridge ends, Blocks at each tower	Total 8 LG were operated simultaneously	Key-segment lifting 4 LG were operated for 1 key-seg

Table 3-1: Scheme of suspended deck erection [65]

Four gantries were used in a complicated plan to lift the tower segment along with the two adjacent ones as a single block (Figure 3-10 a). Given the close proximity of the tower leg (Figure 3-10 b), particularly as the tower deck block reached its highest level, an in-depth workspace study along with careful monitoring and control during the lift were performed, resulting in a successful operation. A modified sequence with fewer weather window requirements was created and put into use to reduce construction delays. It made it possible to lift each tower deck block independently. Each block was welded to the side span deck only once it had reached its final level. Once both tower deck blocks were in place, the main span deck was welded.



Figure 3-10: Single deck segment lift near the tower (a, left); European tower deck block lift (b, right) [61]



Figure 3-11: Views of the 1915Çanakkale Bridge's deck from the ferryboat (IABSE Symposium-04.28.2023)



According to what is stated in the article's concluding section previously reported, deck erection over the Dardanelles presented specific challenges due to *currents* and *winds* in the strait [61].

Among the most important aspects, the innovative solutions adopted to deal with the various problematic situations during the construction of the aerodynamic deck are emphasized: especially the self-erection system, which is presented as a proven technology and could be used in future as a fast, versatile, safe and economical method to install deck lifting gantries on suspension cables. The Figure 3-11 highlights the *final construction of the bridge deck*.

3.1.2 Soil-structure interaction: foundations, towers and anchor blocks

An attempt is also made to understand the decision-making and design process in reference to the location of the massive structure in connecting the two ends of the Dardanelles Strait. Among the most indicative aspects of this design phase is intended to highlight the aspect of the geological framework of the area and the influence made on the adoptable solutions for the foundations of the structure.

The research and project work proposed by V. Boteanu, J. S. Steenfelt, M. Schunk, and B. Zhao [66] shows a feasibility study that included three land boreholes at 150 m depth and a comprehensive geophysical survey in the alignment corridor in the Dardanelles Strait between the Biga Peninsula on the Asian side and the Gallipoli Peninsula on the European side. The overall surface geology manifested several critical issues that led the designers to diversify the decision-making process and make careful assessments for the *placement of the tower foundations*.

The analysis of local rock outcrops helped in the early stages of geotechnical design to gain insight into Miocene deposits. To take advantage of better ground conditions and avoid establishing the anchor blocks in Holocene deposits, the structure was placed at approximately 450 m and 250 m to the southwest, on the European and Asian sides, respectively. However, implementing certain structural changes, such as extending the distances between side span piers and relocating the main cable anchor blocks, was the only way to reach the ideal outcome. The towers were positioned to roughly correspond with the same water depth (about 40 m) as the seafloor, which exceeded 80 m at the center of the Strait. This was made possible by the new positioning of the anchor blocks, which allowed the foundations of the towers to be moved to a lower level on the seafloor. Although there is a *high risk of earthquakes* in the region, the geophysical investigation suggested no active faults along the original alignment, as shown in Figure 3-12. The geotechnical difficulties with the original alignment are also depicted in this figure, including the *risk of liquefaction, erosion, and slope stability*.

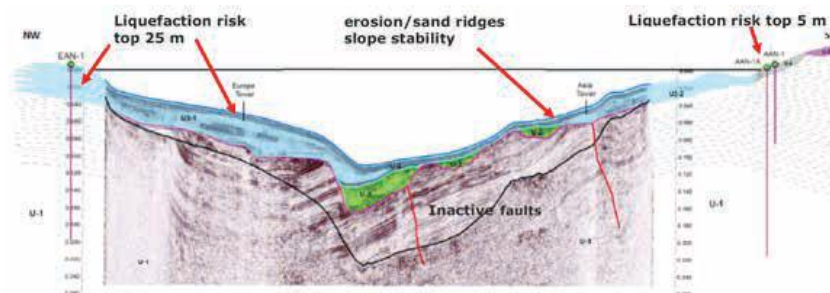


Figure 3-12: Geotechnical risks in original alignment [66]

A very large area was considered for the study of the bridge's original alignment and subsequent evaluations [67]: the "use belt" of the Strait of Dardanelles under consideration is equivalent to a corridor of about 500 m around the original alignment. Only the main span of 2023 m was kept fixed in the design of the bridge's alignment and rectilinear configuration for well-known reasons related to historical symbolism associated with the Turkish Republic. On the other hand, to find the best position, the length of the side spans and the placement of the anchor blocks are both adjustable.

Studying the alignment, from the original position seen above, required complying with the principal criteria listed below:

- *Soil conditions*
- *Water and ground water depth*
- *Interaction with existing infrastructure*
- *Ship impact*

To position and arrange the bridge in the best possible way (Figure 3-13), *five different bridge alignments were studied*:

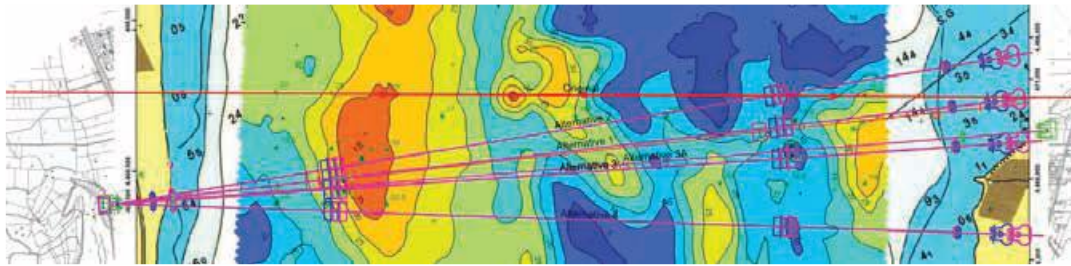


Figure 3-13: Original alignment (red) and 4 alternative alignments (purple) [67]

Utilizing advanced three-dimensional numerical simulations with *Plaxis* and the loads from the internal *IBDAS* (COWI's in-house software) *structural model* for all pertinent limit states, the geotechnical design was verified. The *final positions* [66] have been established shortly after extensive geotechnical and structural studies. The anchor blocks and side span piers, which were sharply visible on *Google Earth* during construction, were defined in their final locations. The following were the *main advantages* of the new alignment: as the *gravity-based anchor blocks* in European and Asian shores due to a shortage of very soft and liquefiable top layers. In addition, due to shallower excavation depth, anchor block construction required fewer resources and less time. The European anchor block was positioned in the hillside so that soil could be added on top of it, acting as a counterweight and lowering the amount of concrete needed. Additionally, because of the location, the first approach bridge piers were on the anchor block, which helped the counterweight. In conclusion by placing bars under the block to support the horizontal load of the cable rather than the anchor block's weight, a significant reduction in the concrete volume of the Asian anchor block was made.

There is also a desire to focus on what *T. Löhning* and *U. Ravn* [67] mentioned regarding the design and construction of the tower foundations and the towers themselves once the final alignment of the bridge was established. As mentioned, four different concept solutions to the tower foundations were studied: *An open dredged well foundations*; a *steel space frame foundation*; a solution with *large diameter vertical steel foundation piles connected to a pile cap* placed slightly above the water level; a *cellular caisson structure with ground improving inclusion piles*. A *cellular caisson structure with ground-improving inclusion piles* was picked as the concept for the detailed design of the *tower foundations*, as shown in Figure 3-14 and Figure 3-15:

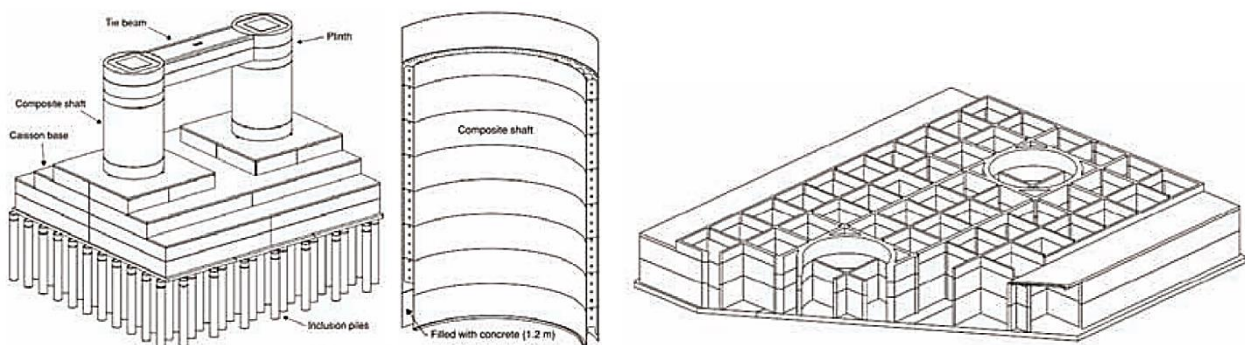


Figure 3-14; Cellular caisson with inclusion piles foundation's solution [67]

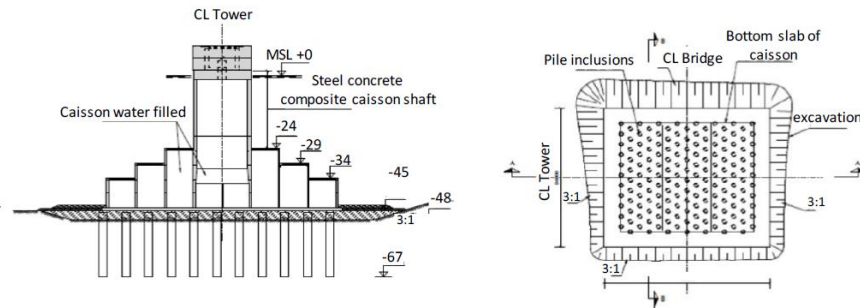


Figure 3-15: Cellular caisson with inclusion piles foundation's depth [42]

As previously mentioned, the design solution adopted by COWI closely resembles the one created in 2016 for the *Osman Gazi Bridge* in Turkey [68]. It consists of infilled steel tube inclusion piles supporting a precast concrete caisson via a gravel bed. The benefits of this choice, which was made for the *1915Çanakkale Bridge*, are then listed:

- The capacity to handle various ground conditions (variably soft material below the seabed) using a general solution modified as necessary for site-specific conditions.
- The driven inclusion piles are manufactured and built concurrently with the caissons, allowing for a condensed construction schedule.
- The caisson's ability to "slide" (an energy dissipation mechanism) a short distance during *seismic* and *ship impact events* prevents the failure of supporting piles.

The *static analysis* [68] of the overall performance of the piling system, as seen in Figure 3-16, is what prompted the designers to come up with this optimized solution. Here, the inclusion piles (brown tubes) can be distinguished from the caisson (green and blue) by a layer of gravel (light blue) that surrounds the pile head and acts as a "cushion" between their tops and the base of the caisson. Due to different soil conditions and pile layouts, 3D finite element analyses were conducted for both towers; these provided results of static axial gravitational loading along the piles. Due to the low strength and compressibility of the European tower stratum, which is the primary difference between the two towers, the following important observations were made:

- *European tower* load mobilized to the peak of the pile: the load is moved directly from the caisson to the pile. Although the in-situ soil below the gravel does not significantly contribute to the load transfer capacity, this is a *relatively brittle system* that relies on the gravel at the top of the pile to carry the majority of the load.
- At the *Anatolian tower*, only a small amount of load is mobilized at the pile's top, with most of the load being transferred from the in-situ strata to the pile by shear friction. The lower section of the pile serves as where the load is transferred into the mudstone. In accordance with the intended results and expected outcomes, *this system is relatively ductile*. through which "inclusion piles" are used in place of regular piles [68].

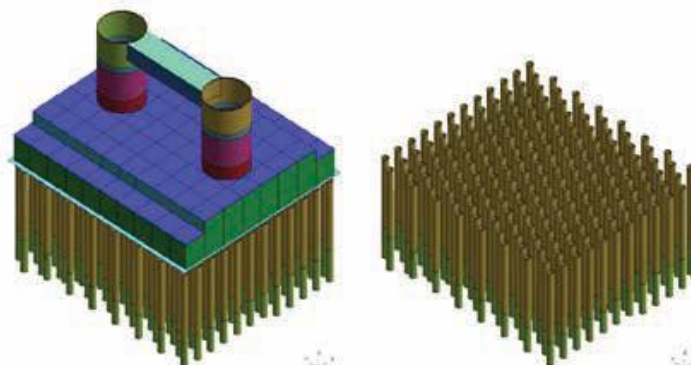


Figure 3-16: 3D FE-model of piles and caisson [68]

Ship impact analysis is also analyzed by P. Morrison and L. H. Kaasa [68], providing calculations of pile forces and caisson displacements for the final foundation design, as shown in Figure 3-17. the caisson moves in rotation around an eccentric vertical axis with a maximum movement of about 270 mm; most importantly, it can be seen that the pile heads do not move as the caisson moves, demonstrating that the gravel "cushion" works as intended.

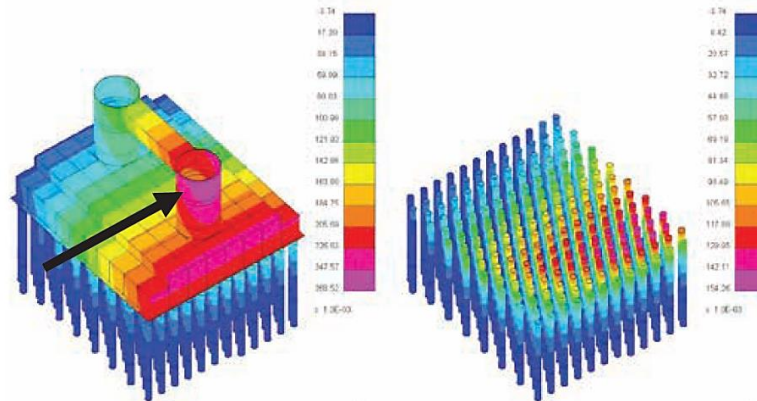


Figure 3-17: Ship impact load case on 3D FE-model [68]

Also reported is the *dynamic soil-structure interaction analysis* [68] that has *seismic analysis* as a reference point. The tower foundation made it challenging to precisely evaluate how well each component performed under the load prompted by the seismic event, even though the bridge is situated in a region with a *high seismic activity*. The infilled steel inclusion piles must be able to withstand inertial loads from the tower superstructure and kinematic bending moments due to ground deformation. In addition, the effect of the inclusion piles and gravel mat on the response of the tower during seismic excitation had to be evaluated. The presence of the inclusion piles will cause the ground motions below the tower to be isolated from the surrounding free field. In addition, the presence of the gravel "cushion" under the caisson generates discontinuities and a substantial reduction in the seismic input force applied to the structure itself, similar to seismic isolators in buildings. To efficiently design the tower foundation, the *direct method* was implemented to determine *dynamic soil-structure interaction* (DSSI) occurring at the tower caisson, gravel mat, inclusion piles, and soil interfaces (Figure 3-18). The tower was modeled using beam elements, shells, and concentrated masses to capture the inertial response while the soil was modeled using a nonlinear model that captures the degradation of soil stiffness with increasing deformation and hysteretic damping. Time histories of shear stresses contributed by the earthquake were applied to the base of the foundation-tower system to propagate shear waves to the surface, simulating seismic excitation.

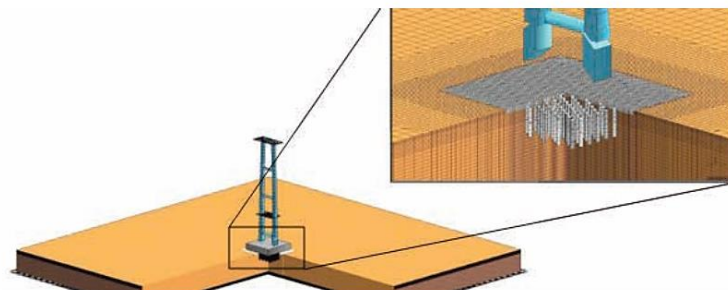


Figure 3-18: Dynamic soil-structure interaction (DSSI 3D FE-model) [68]

Following the above discussion on design, it is considered interesting to focus on the *construction* and assembly of the components of this structure, such as *tower erection* and *cable structures installation*. The paper presented by L. H. Kaasa, R. Hornby and K. Aas-Jakobsen [69] concentrates on analyses of these *temporary works*.



The *tower design* of 1915Çanakkale Bridge put forward by S. Park and H. Paik [70] introduces the use of steel to reduce the inertial force caused by the earthquake and shorten the construction period. The tower has a cross section of 11.0 m by 10.5 m at the base and 8.0 m by 7.5 m at the top, and three crossbeams were installed between each leg of the tower. It is 318 m high above sea level and 315 m from the foundation dock, as shown in Figure 3-19.

The *tower assembly verifications* have been revealed in the paper submitted to the IABSE Symposium in Istanbul [69]. The 31 assembly steps indicated included verification of the structural integrity of the tower legs, temporary transverse beams, and permanent transverse beams. Additionally, calculations for wind-induced vibration as well as the evaluation of the necessary weld ratio for each joint at all stages of the erection process were reported. At each stage of construction, the tower model was completed with components that represented temporary cross beams, a climbing tower crane, and a smaller crane used to assemble the cable and bridge at the top of the tower. Since the tower crane has a sizable impact on wind dynamics, it was first meticulously modeled, with beam elements standing in for each distinct tower truss. Then, an equivalent string of beam elements was used to replace the complex tower model, greatly reducing model complexity and computational time. According to the requirements of the contractor, rigid beam elements with mass distribution and wind areas were used to model the tower crane's top. Additionally included during construction were *active mass dampers*, which are modeled as point masses. By enhancing the structural damping of the tower's first longitudinal mode, the damping effect was added to the wind analyses. Along with the usual analyses of wind and temperature, the seismic response of the structure was also examined, which turned out to be crucial for some temporary structures. To evaluate the structural integrity of the latter, seismic response spectra were obtained using local finite element analysis. Displacements were imposed at each end to examine how each *temporary cross beams* (TCB) interacts with the rest of the structure.

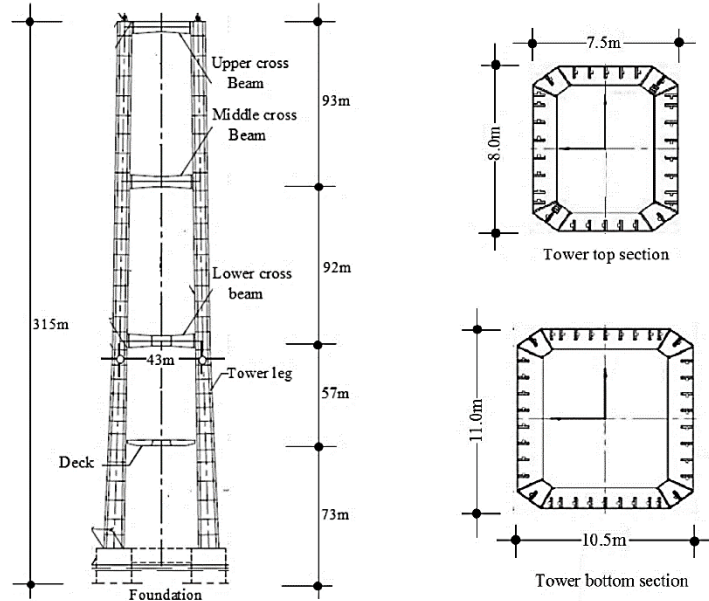


Figure 3-19: Tower dimensions [71]

Considering the lifting equipment's capacity [70], the structural stability in the tower's independent state, and the construction schedule, the steel structures of the tower were manufactured and erected by subdividing a total of 32 blocks for each leg (Figure 3-20). The tower was initially constructed as a "full-block" using an offshore floating crane with a 2200-ton capacity. In particular, anchor tie-rods were used to install the first block into the concrete dock at the top of the tower foundation caisson. To be lifted by a tower crane, the following blocks were originally intended to be *half-blocks*. However, due to the site's constraints, the halved blocks were assembled on land and put up by floating cranes at sea. As a result of the additional diaphragm reinforcement within the block, the blocks close to the suspended

steel deck and the three cross beams connecting the tower were made of a quarter panel. *L-shaped half-panels* made up the remaining blocks. Before putting in the permanent crossbeams for the tower, a total of eight temporary crossbeams had been installed in to support each leg. The distance between the legs was accurately determined before closing the permanent crossbeam, and it was subsequently adjusted using a hydraulic jack on the temporary crossbeam to the desired distance.

High-strength bolts connecting the vertical stiffeners inside the blocks and welding the facing plates were used to create a *hybrid connection* between the blocks. The steps of tower construction by tower crane are also shown in Figure 3-21.



Figure 3-20: Full block lifted by offshore floating crane (left); L-shaped half-block lifted by tower crane (right) [70]

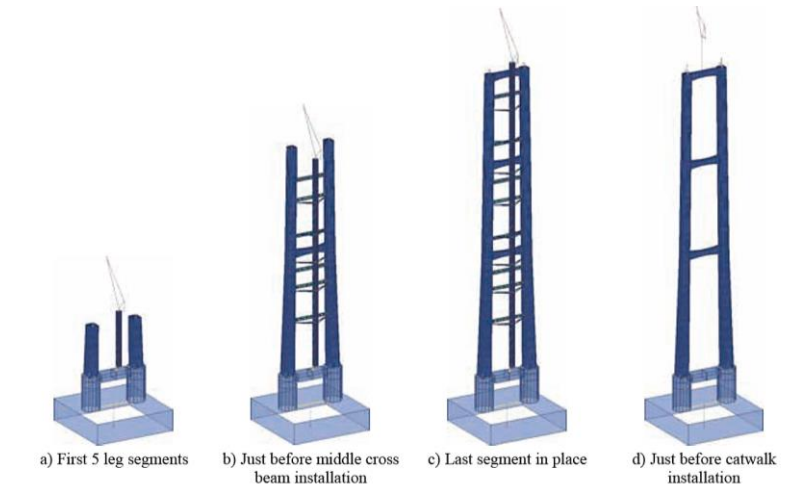


Figure 3-21: Steps of tower construction by tower crane [69]

Geometry control criteria [70] had to be put in place while the towers' building blocks were assembled. A slender steel tower of more than 300 m needs precise verticality controls, so the installation of B01 (the full block) was carried out under close supervision with a position error of 20 mm and a verticality error of 5 mm. Figure 3-22 illustrates the fundamental idea of managing the steel tower's geometry during construction.

Through a variety of sensors installed on the structure, such as a GNSS receiver for the tower's three-dimensional coordinates, a thermometer for the blocks steel surface, an anemometer for wind speed and direction, and an inclinometer for slope and settlement data, assessment information relating to the surrounding environmental conditions are obtained in real time. To lessen the impact of solar heat on the steel material, these data were collected at night. The GNSS receiver records displacements caused by environmental factors like temperature, wind direction and speed, and the impact of site work like tower cranes and temporary crossbeams. Eliminating these environmental influences on tower displacement is crucial.

This process was required to analyze the pure construction error in an environment as close to the factory preassembly environment as possible (inside, at a temperature of about 15°C, with no wind). A 3D analysis model of the construction phase was used to apply the errors to external forces at this stage of evaluating the erection error, environmental effect (wind and temperature picked up overnight), and site activities (tower crane movement). The pure construction error of the tower can be found, and the geometry (linearity) of the structure up to the corresponding block height can be established, once the displacement computed from the prior model is subtracted from the coordinate values obtained from the GNSS receiver [70]. By adding an adjustment plate to the connection before mounting the subsequent block, the construction flaw that was outside of the permitted margin of error could be repaired.

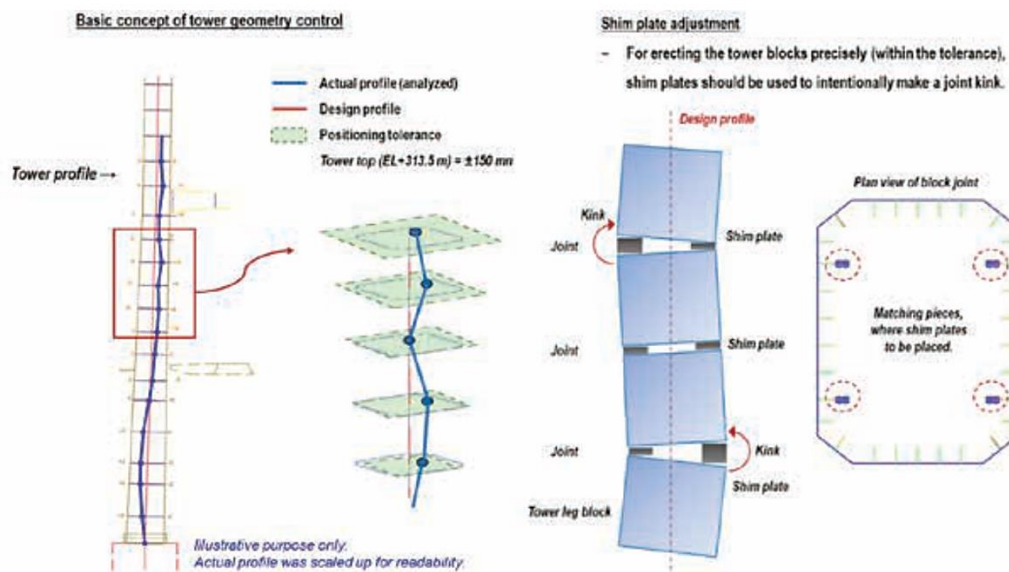


Figure 3-22: Tower geometry control concept [70]

T. Löhning and U. Ravn [67] (cited earlier) also introduce the *design choice of anchor blocks* that was closely related to the alignment of the bridge given the geological conditions encountered.

Anchorage blocks for suspension bridges must safely transfer forces from the main cable to the ground. In a seismic area such as the Çanakkale site, the large mass of the anchor blocks can generate significant reaction forces in addition to the cable forces. The ground conditions at the anchor blocks are the main factor in choosing the most favorable concept. The authors of the paper being reported indicate how for the 1915Çanakkale Bridge *four main concepts* were considered during the initial design phase: (a) *Circular massif*; (b) *Dual circular massif*; (c) *Tunnel anchorage*; and (d) *Flat foundation slab*.

The placement of anchor blocks can be optimized with a large flat and different foundations for the two front legs based on the modified alignment, resulting in better ground conditions. Excavation is done without using substantial temporary supports. Concrete is poured directly against the rock surface for parts buried in rock without formworks. The back portion of the *European anchor block* is set inside the outcrop of rocks and the backfill serves as a counterweight. The same logic holds valid for the *Asian anchor block*, but due to the higher ground level, the anchor block is situated higher as well.

In addition, the weaker soil under the Asian anchor block compared to the European anchor block requires some additional measures, such as the use of diaphragm walls to increase the shear capacity of the anchor block. The use of innovative features greatly reduces construction time, material quantities and excavation, which leads to a sustainable project. Looking at the design concepts of the anchor blocks in more detail, it is possible to see how the *European anchor block* [66] is a rigid concrete structure that is intended to act as both a foundation for the approach bridge abutment and an anchor for the

suspension bridge. Backfilling was done later to lessen the overturning moment because the original rock outcrop was present and had been partially removed for the construction of the anchor block massif. The European anchor block is made up of two front pads that are 18 m by 17.5 m in plan and 5 m high, as well as a rear massif that is 16 m high, 50.2 m wide, and 74.4 m long when measured from the top. A connecting beam joins each front pad to the back massif. Advanced three-dimensional numerical simulations using *Plaxis* for loads determined by the *IBDAS* (in-house COWI's software) model for seismic, ultimate, and serviceability limit states were used to confirm the geotechnical stability of the anchor block. On the other hand, the *Asian anchor block* [66] includes three parts, the rear massif and two front pads. The massif is a concrete block that is 56 meters wide by 80 meters long by 16 meters high. As shown in Figure 3-23, *eight diaphragm panels* with a thickness of 1.2 m each were excavated and cast underneath the massif to increase the sliding capacity of the structure. These eight panels made up *seven barrettes* with a height of 13.5 m and a length of 51.5 m. These were angled in the alignment's direction and offer further friction resistance. This particular design, which results in significant savings in concrete and reinforcement volumes, is based on research findings of reduced undrained shear strength in Miocene summit deposits with ductile behavior under the anchor block.

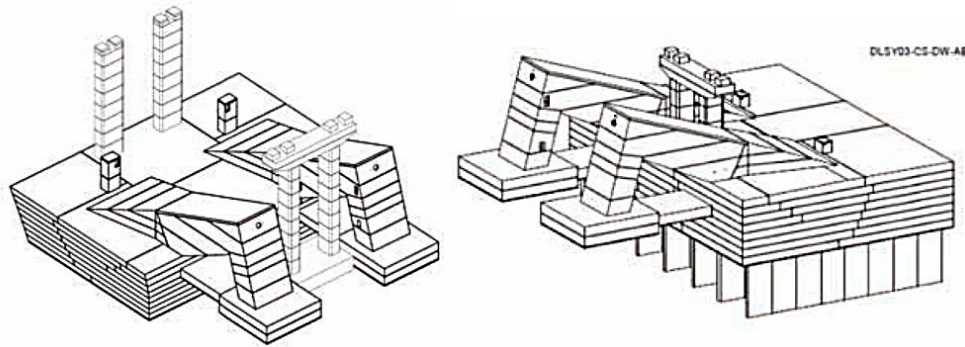


Figure 3-23: European anchor block (left); Asian anchor block with barrettes (right) [66]

3.1.3 Cable structures: main cable and hangers

Due to poor soil conditions at the shorelines, the 1915Çanakkale bridge's anchor blocks have been located 250m and 350m onshore in relation to the end of the suspended deck. This is done by introducing a *tie-down arrangement* [72] at the expansion joint that prevents vertical movements of the main cable at that position. The tie-down system includes a long tie-down clamp on the main cable, anchored to the ground by four large cables. At the top of the tower, the main cables are at a height of +318 m (symbolizing the naval victory at the Battle of Gallipoli on March 18, 1915). The lowest point of the main cable is at 228 m from the top of the towers (*sag*), such as to give a sag-to-span ratio of 1/8.87. Longitudinal movements of the bridge deck, on the other hand, are controlled by *hydraulic buffers* and end stops on the towers.

The *main cable* is one of the primary structural components of the suspension bridge typology. The *main span's cable* of the 1915Çanakkale Bridge is made up of 144 prefabricated parallel wire strands (PPWS) [72] that run continuously over a distance of 4400 m from one anchorage to the next. There are 148 wire strands in total as a result of the installation of four more strands in the *side spans*. Due to the higher force in the side spans compared to the main spans, which results from the ratio of side span over main span length, these side spans' strands are provided and are anchored at the tower saddles. The main cable's ULS force is 502 MN for the side span and 491 MN for the main span, respectively. A total of 127 wires with a 5.75mm diameter and a tensile breaking strength of 1960MPa make up each strand (Figure 3-24). Two threaded rods with a 64 mm diameter are then used to secure the strands to the anchor plate, also known as *cross-head slab*.

Each anchor plate holds four strands and is consequently protected to the anchorage chamber by two post-tensioning cables in order to minimize the footprint of the anchorage structure and the cost of anchorage blocks. Thus, all 148 strands can be secured in a 10 x 7 m area [72].

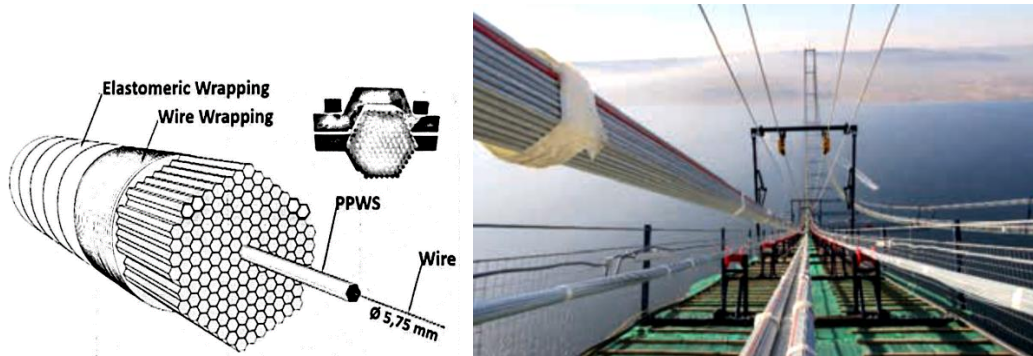


Figure 3-24: Main cable internal structure (left); main cable installation (right) [72]

As previously indicated, the *main cable's composition* is displayed in Table 3-2, and it weighs a total of 33108 tons. The saddle section was pre-shaped into a rectangle at the factory and brought to the construction site to reduce the on-site shaping work program. The strands of the general section are arranged in a *conventional hexagonal layout* [73].



Item	Main Span	Side Span
Strand Arrangement		
Strand composition	1 strand = 5.75 mm wire × 127 nos	
No. of strand (/cable)	144 nos	148 nos
Diameter of cable	869 mm (void ratio: 20%)	881 mm (void ratio: 20%)

Table 3-2: Main cable's composition in main span and side spans [73]

The *strand erection sequence* is highlighted by researchers *J. Kim* and *H. Choi* [73] and illustrated in Figure 3-25. The following considerations were considered when determining the sequence.

- I. to maintain free-hanging condition of the reference strand.
- II. to prevent deformation of the spacers in the saddles.
- III. to minimize galloping of erected strands

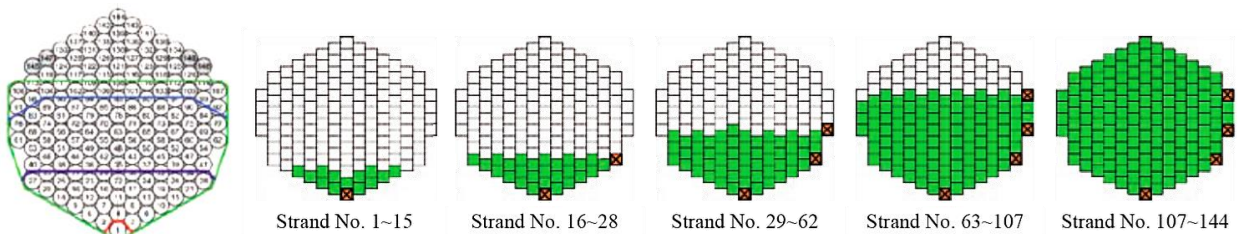


Figure 3-25: Main cable complete layout (left); Strand erection sequence (right) [69] [73]

The importance of maintaining an adequate vertical distance between the strands is emphasized in the proposed paper. The allowable temperature difference and tolerance for the reference strand's free suspension state increase with increasing distance between the reference strand and adjacent strands, which is advantageous for geometry control. However, during strand assembly, the stress difference between the cable diameter and the strands increases, making assembly work challenging. The minimum vertical spacing between the strands in this project was found to be 10 mm.



The construction sequence was chosen to keep the top layer of the installed strand group horizontal to *reduce galloping* [69] caused by the site's high wind speed. Additionally, it was thought that the saddle spacer might deform because of the strands' lateral pressure if they were erected with a slight slope to one side. 1, 28, 62, 107, all 144 strands (148 for the side spans), and finally the connections of suspension cables and clamps were all examined as *construction stages* (Figure 3-25). All catwalk components were turned off after cable assembly in order to speed up calculations for the bridge's assembling, and cable mass and wind area were replaced with equivalent combined values for the catwalk and cable.

The *Prefabricated Parallel Wire Strand* (PPWS) erection [73] was speeded up considerably through the installation of two *un-coilers* on each cable line. A strand's tensioning for the first 10 strands took 24 hours to complete. However, as the project moved forward, the stringing process was improved, and after the installation of 40 strands, the slope adjustment and stringing operations produced *1 strand in just 4 hours*. The main challenge is that *the strand tends to twist* because of a combination of factors including temperature differences brought on by the variations in the pulled strand, the weight of the pulled strand itself causing the catwalk to slope, the displacement of the carrier due to wind, and the friction between the rollers and the strand on the catwalk. A *manpower-controlled anti-rotation tool* was installed to stop the strands from twisting. It should be remembered that after the strand installation was complete, the entire section was visually inspected to see if the strand was twisted before the saddle and socket anchorages.

As with the geometric control of towers, it is also necessary to accurately *inspect cable structures* [73]: in particular, the monitoring system using GNSS receivers and rover total stations for *absolute* and *relative sag* of strands is presented.

The bottom-most strand, No. 1, was put in place first and designated as the *starting point reference strand*. By measuring the height of the *sag point* for each span, the geometry of this strand was established. Both the GNSS method and the traditional surveying method with EDM (total station) were used as the measuring methods. As depicted in Figure 3-26, GNSS receivers were installed on the reference strand at each sag point and the top of each tower curvature. By measuring the relative elevation in relation to the reference strand (*relative sag*), the geometry was modified for subsequent strands. Vernier caliper type instruments have been used in earlier projects to measure relative sag. However, when using this kind of instrument on strands with a large diameter, productivity suffers, and accurate measurement is challenging because of the weight of the measuring tool. This issue was resolved by measuring the *relative sag* with a *laser level*.



Figure 3-26: Survey equipment's arrangement for absolute sag [73]

One of the most critical procedures is the *measurement of strand temperature* due to the high sensitivity of sag value to strand temperature. Even if the temperature of the strand stabilizes in the early morning, the location-dependent temperature difference cannot be avoided because the distance between the locations where the installed strand is located can only be up to 300 m. As a result, data on temperatures were taken at the locations denoted by the *red dots* in Figure 3-27; of special note are the sag points of each span. The representative temperature for each span was taken to be the average value.

It was demonstrated, particularly in the *temperature study*, that the tower tends to move about 10 mm per hour during the warmer sunset hour. Every 15 minutes, the tower displacement monitoring was checked, and once it was determined that the tower displacement had sufficiently converged, the absolute sag survey was carried out [73].

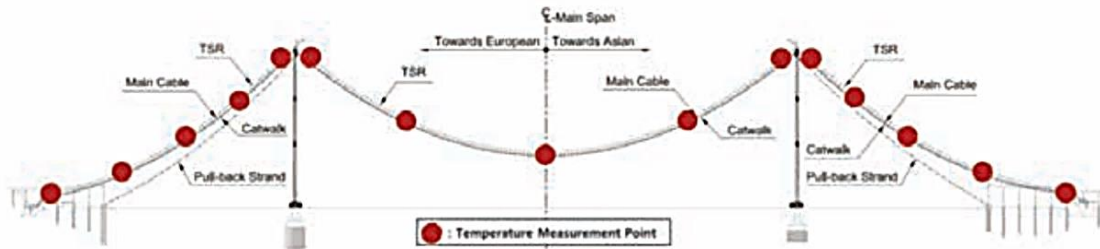


Figure 3-27: Temperature measurement points [73]

The *sag adjustment procedure* is shown in Figure 3-28. The strand at the sag point of all spans was set to be higher than the target after each strand had been established. As shown in figure below, the European side tower saddle served as the *fixed point*, and the Asian side tower saddle was used to move the strand into the main span direction to adjust the main span sag. As a result, the sag was adjusted for each side span by releasing the strand at each anchor block.

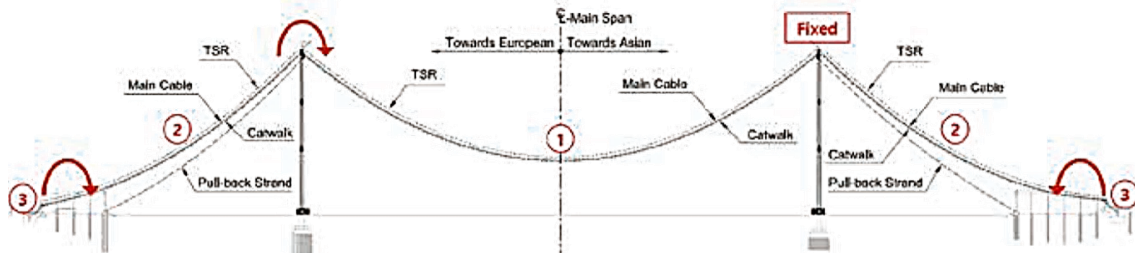


Figure 3-28: Sag adjustment procedure [73]

The *saddle* was mentioned in this section: *tower saddle design* is of undisputed importance because it is an integral part of the cable-tower system. The design process for these crucial main cable laying components is described in the paper put forth by *J. Pihl* and *H. Choi* [72]. The saddles are designed to *support the main cable*. In a tank with a vertically curved surface that has a radius of 8.0 m, the tower saddle supports the main cable and transfers the force from the main cable to tower. This radius was chosen to prevent the main cable wires from experiencing excessive transverse stresses. It is also demonstrated as the saddles are welded to the tower's top to give it enough stiffness to transfer loads. The tower saddle and top of the tower are significantly twisted as a result of the deformation of the bridge *aerodynamic deck* because the bridge girder is made up of twin boxes spaced 9 m apart. For this load combination, the main cable remains straight, which places a significant amount of transverse stress on the saddle's sides, as shown in Figure 3-29.

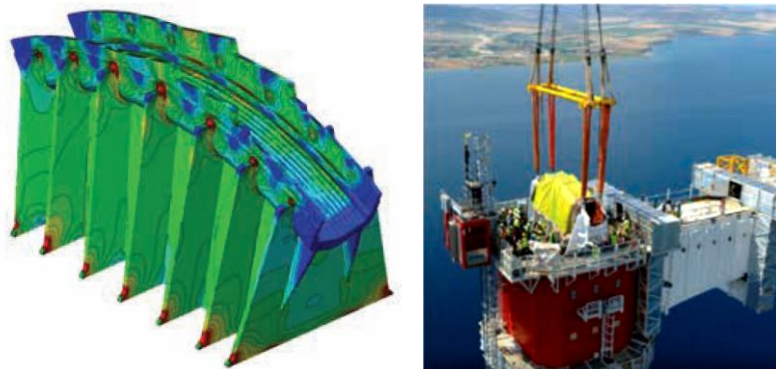


Figure 3-29: Von Mises stress plot of tower saddle structure (left); Tower saddle installation (right) [72]

Following the introduction of some constituent elements of the bridge structure, it is also considered important to report some information regarding *hangers* and their design. The suspended deck is supported by 141 pairs of hangers on the 1915Çanakkale Bridge. There are 83 pairs of hangers in the main span and 29 pairs in each side span [72]. Due to the higher load in these locations, the first four hangers at the ends of the suspended deck and the first two hangers on each side of the towers were designed as double hangers. The hangers are made of 139 or 151 7-mm wires with a 1770 MPa yield strength. In a Prefabricated Parallel Wire Strand (PPWS) procedure, the wires are assembled. To make it easier to wrap the strand, the wires are twisted just 3.5° to form a spiral structure. Additionally, four larger cables using 367 numbers of 7mm wires are used for the *tie-down cables*. Because of the ULS load combination, the hangers have been designed to withstand loading. However, a lot of the hangers' designs are dictated by *accidental load combinations*. Two adjacent hangers are expected to be removed in these scenarios because it is not possible to design a hanger to withstand a *vehicle collision* or the *heat radiation from a fire* on the bridge deck. The remaining hangers are then made to support the redistributed loads. The hanger rupture is modelled using time history analysis to produce precise results. Moreover, specific analyses are made to determine the exact rotation for selected hangers for both *traffic loading* and *during a seismic event*. When a spherical bearing is introduced in the hangers, the PPWS will be able to untwist when loaded as the wires are not fully parallel. The wires are coated with a 9-mm-thick HDPE coating to increase the hangers' durability. Suitable barges were used to lift the hangers beneath the cable clamps and mounted to the cable clamps from the catwalk (Figure 3-30). The setting up of the deck segments began with the installation of the first hangers.



Figure 3-30: Hangers' installation [72]

3.1.4 Structural health monitoring (SHM)

One of the most important aspects of modern engineering concerns the built environment. It is very important, now more than ever, to provide for new and older structures a monitoring system to ensure their *structural safety* to preserve human life (ULS) and *functionality* as the structure itself maintains over time the characteristics for which it was designed (SLS).

Figure 3-31 and Figure 3-32 show the sensor configuration for the 1915Çanakkale Bridge's Structural Health Monitoring (SHM) system, including the positions of various sensors on the bridge's *longitudinal layout, deck, and towers*. Regarding the variety and quantity of sensors, the SHM system shown in Table 3-3 is the *most advanced system for a long span suspension bridge in the world*.

As reported in the paper by M. N. Apaydin, A. C. Zulfikar and O. Cetindemir [71], following the construction of the bridge, *several new types of sensors* were introduced, different from the early examples of SHM applications in the past. Unlike other long-span bridges built in Turkey, the innovative SHM system confers several benefits on the structural monitoring of the bridge, ensuring its structural safety and continued serviceability: to *maintain structural integrity*, *air temperature sensors* measure temperature changes on the deck and towers. *Barometric pressure sensors* are used to predict weather conditions by

detecting changes in atmospheric pressure for traffic safety. *Cable thermometer sensors* measure the temperature of the main cable to prevent extreme conditions and *asphalt temperature sensors* measure the surface temperature on the top of the steel deck to ensure traffic safety.

Also present are *sonic distance sensors*, which are placed in mid-span to detect any objects approaching the bridge to ensure monitoring of the environment, *steel temperature sensors* used for various components of the bridge to monitor temperature changes for the safety of people, *pyrometric sensors* which measure the temperature of distant objects, *corrosion sensors* used to detect deterioration caused by the environment to help assess the safety and predict the service life of the bridge, *road weather measuring station* which can interface numerous types of dataloggers and sensors that measure, calculate, and process various meteorological quantities such as temperature (air and road), wind speed and direction, atmospheric pressure, relative humidity precipitation (indicator and amount), visibility, road conditions (ice, snow, wet and dry) and freezing point. Another innovative aspect is brought by the *weight-in-motion system sensors* used to measure traffic volume, load, total weight, and speed of vehicles to monitor traffic conditions. The purpose of monitoring the weight of vehicles approaching or crossing the bridge is to avoid extreme loads to improve structural safety. Efficient management of bridge structures requires a thorough understanding of traffic conditions. Therefore, these new types of sensors can provide additional information on an automated basis that SHM systems can offer [71].

Two *seismic data acquisition units* (DAUs) were installed on the European and Asian sides, respectively, close to the anchor block and the approach bridge piers, in addition to the structural monitoring system, to track the geotechnical response to a seismic event in the bedrock and soil. Three force-balanced triaxial *accelerometers* were installed at each location, in the bedrock and ground level [74].

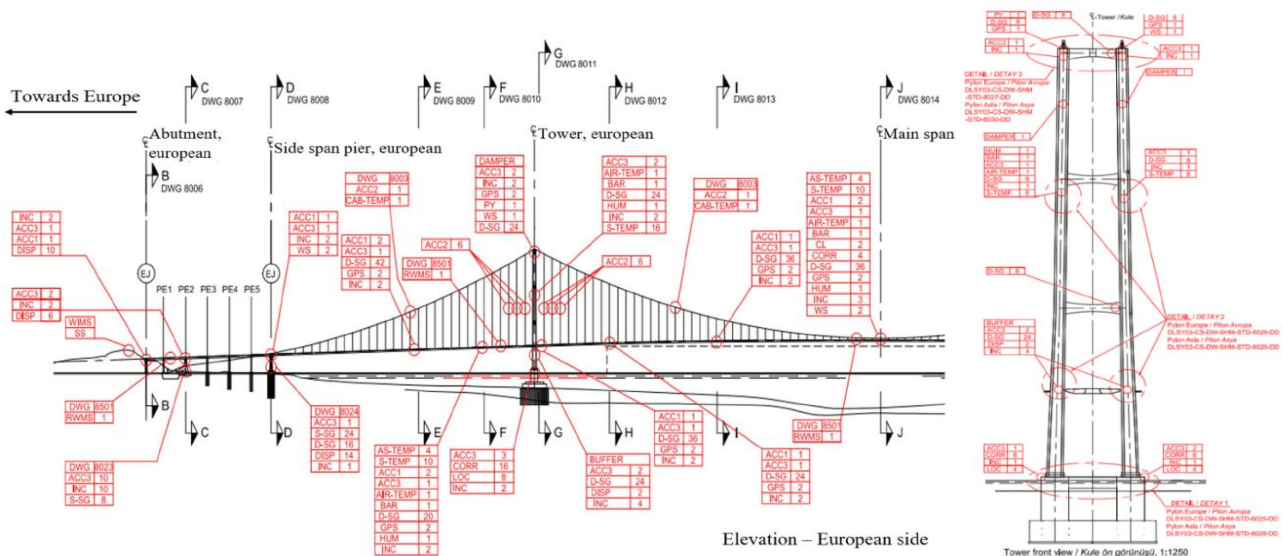


Figure 3-31: Sensor locations of SHM system of 1915Çanakkale Bridge [71]

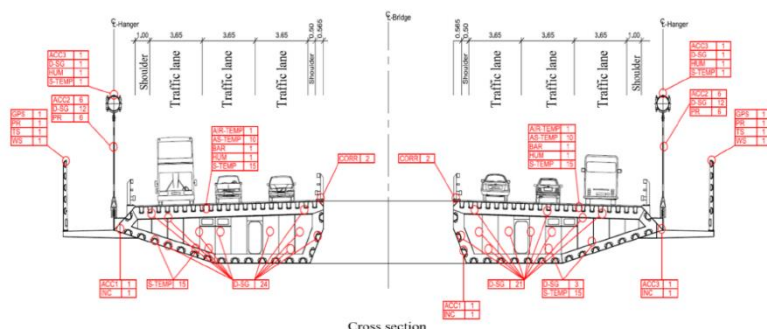


Figure 3-32: Deck's SHM system (left) [71]; 1915Çanakkale Bridge's control center (IABSE Symposium-04.28.2023) (right)



Sensor tag	Sensor name	Quantity
ACC1	Uniaxial accelerometer	18
ACC2	Biaxial accelerometer	28
ACC3	Triaxial accelerometer	57
AIR-TEMP	Air temperature	4
AS-TEMP	Asphalt temperature	8
BAR	Barometric pressure	4
BUFFER	Sensor in the buffer	2
CAB-TEMP	Cable thermometer	4
CL	Clearance-sonic distance sensor	2
DAMPER	Sensor in the damper	4
CORR	Corrosion sensor	36
DAU	Data acquisition unit	34
DISP	Displacement sensor	64
D-SG	Dynamic strain gauge	508
GPS	GPS receiver	26
HUM	Humidity	4
INC	Biaxial inclinometer	74
PY	Pyrometer	2
LOC	Load cell	16
RWMS	Road weather measurement station	4
S-SG	Static strain gauge	88
SS	Seismic station	2
S-TEMP	Steel temperature	52
WIMS	Weight in motion system	2
WS	Weather station	6
Total		1049

Table 3-3: List of SHM system's sensors [71]

3.2 1915Çanakkale Bridge's hybrid solution

The term "hybrid bridge" applies to bridges that are *a combination of a suspension system with parabolic main cables and hangers, and a cable-stayed system*. This idea comes from J. A. Roebling, one of the most revolutionary bridge designers of the mid-1800s. As reported in Chapter 1, the *Niagara Falls bridge*, the first hybrid bridge in history, was completed in 1855. Adopting a hybrid technique for the bridge, J. A. Roebling found that placing the stays near the towers made them very efficient by providing high stiffness to the main cable and deck system, which were underperforming for the high railway loads of the time. In subsequent years this structural scheme was repeated on several occasions. One of the most famous examples is the *Brooklyn Bridge* (1883) in New York, designed by J. A. Roebling himself and completed by his son Washington. A more recent application is the *Yavuz Sultan Selim Bridge* (2016), better known as the *Third Bosphorus Bridge*. This section presents an interesting assessment of the possible use of a hybrid structural scheme for the *1915Çanakkale Bridge*, predating the actual construction of the world record suspension bridge.

The paper proposed by M. Virlogeux and J-F. Klein [75] introduces the preliminary design phases of the bridge and what was highlighted in the competition phase of the contract award in 2017. The contractor asked for a preliminary design for a *hybrid solution* to compare it with the suspension solution in terms of quantity, price, and time. The main results (advantages and drawbacks) of this preliminary design are presented below.

Advantages of the hybrid bridge

- *Reduction of the anchorage forces on the anchorage blocks.* The horizontal and uplift forces caused by the main cables directly affect the required weight and, consequently, the volume of concrete for the anchor blocks. Based on the same structural design of anchor blocks for both suspended and hybrid bridges, the *hybrid solution* would save about 82600 m³ or 26% of the concrete needed.
- *Reduction of the main cable size.* The installation of stay cables, the removal of hangers in the cable-stayed areas, and the increased sag of the main cable reduce the loads carried to the main cables, allowing a reduction in their size and a transfer of loads to the stay cables. The reduction in the weight of the main cables is considerable, about 35 %, but the impact of the weight of the hangers (decreasing) and the stay cables (increasing) must be considered: overall, the savings on the entire cable system is 9130 tons, namely 24% of the total cable weight.



- *Increased rigidity of the bridge.* The Third Bosphorus Bridge's main span has had a significant portion of its vertical deflections reduced by the addition of stiffening stay cables. This significant reduction was also a result of the short length-induced high vertical rigidity of side spans. Vertical deflections are significantly decreased and loads are directly transferred from application points to the head of the corresponding tower by the stay cables. *A hybrid bridge with long side spans* that are partly suspended and partly cable stayed presents a very different set of conditions. Tensile forces increase in the main span's suspension cables and stay cables when the main span is loaded. As all stay cables anchored in side spans are far from the abutments, side spans will move upwards, and tension variations in the side span stay cables will be low. However, the hybrid solution has reduced the vertical displacements of the deck by 40% at the critical areas, which are the edges of the 1600 m wide navigation clearance.
- *Reduction of the erection time.* One of the main advantages of the hybrid solution is the reduction in construction time, mainly due to the fact that, unlike a suspension bridge, all operations are not on the *critical path*. For a classical suspension bridge, the critical path is quite clear: the tower foundations, piers, and anchor blocks must be completed on both sides before starting the installation of the temporary elements needed to install the main cable. After that, the deck assembly can start and the main cables, whose installation time is directly inversely proportional to their size, can be installed. The installation of the strands themselves results in a 35% reduction in construction time for a hybrid bridge. There is no need to hold off on erecting and installing the initial bridge segments until the towers, anchor blocks, or main cable or cable bands have been installed. Even before the upper portion of the towers is finished, it is possible to erect the first segments and install the first stays, as was done, for instance, for the *Normandy Bridge* [75].

Drawbacks of the hybrid bridge

- *Increase of the deck steel quantity.* Due to the weight of the anchorage components used to secure the stay cables to the deck and the normal force caused in the deck by the horizontal component of the tensile force in stay cables, the steel weight of the deck in the hybrid bridge option will be slightly higher than in the suspended bridge. 10% of the total deck steel weight has been estimated as the additional steel weight needed to cover the effects mentioned above.
- *Increase of the towers steel quantity.* The amount of steel needed to anchor the stay cables in the towers, the requirement to increase the strength of the transverse beams supporting the deck, and the additional transverse bending moments caused by wind forces on the stiffening cables, half of which is transferred to the towers, are some of the factors that contribute to the increase in steel in the towers. Contrarily, it is important to note that the *vertical load entering the towers is essentially the same in all solutions and is roughly equal to the weight of each tower's main span, including the cables*. In fact, the hybrid option is beneficial because, in a traditional suspension bridge, the load is applied directly to the tower top, whereas in *hybrid solutions*, only a portion of the load is applied there, with the remainder being distributed almost uniformly in the tower section where the stay cables are anchored. The additional steel weight of the towers to cover those effects is 13% of the total towers' steel weight, but it *significantly reduces second order effects*.
- *Erection method.* To reduce the construction time, it is necessary to erect the cable-stayed sections of the deck by the *balanced cantilever method*. Of course, it is necessary to ensure the required stability of the cable-stayed cantilevers during their erection. Therefore, it is necessary to install temporary longitudinal deck supports on the tower and a temporary support in each side span to limit wind-induced vertical and transverse displacements [75].



It is then possible to conclude that a *hybrid solution for the 1915Çanakkale Bridge is feasible offering some important advantages over a classical suspension bridge* (Figure 3-33). A hybrid bridge saves significantly on the quantities of main cables and anchor blocks, but it brings with it an increase in the quantities of material needed for the stay cables, deck and towers. The *main advantage of the hybrid solution is a shorter construction time and a more flexible critical path*, but the costs of this structural solution is slightly higher. The contracting authority's choice subsequently fell on the *suspension bridge solution*.



Figure 3-33: 3D-render of 1915Çanakkale bridge's hybrid solution [75]



Figure 3-34: Views of the 1915Çanakkale Bridge (IABSE Symposium-04.28.2023)

Many of the geometric features and construction details were researched at the *IABSE Symposium on Long-span bridges* held in April 2023 in Istanbul (Figure 3-34), where it was possible to interact with the designers of the *1915Çanakkale bridge* and many experts in the field of wind and structural engineering.

CHAPTER 4 Finite element modeling

Research studies carried out in the years prior to the construction, and upon completion, of the 1915Çanakkale Bridge produced several results with analytical, semi-analytical and numerical approaches regarding the problem of aeroelastic instability. The posed objective of the thesis was to construct 3D finite element models that were calibrated to provide data as similar as possible to that of other research regarding the behavior of the bridge in *modal analysis* in the absence of wind and in *flutter analysis*. This provides insight into the mechanical characteristics of the deck and its ability to withstand dynamic interaction with the wind. In addition, considering the complex availability of data about the geometric and mechanical properties of the structure of a very recent bridge, the models developed and verified in ANSYS APDL are the result of an *iterative process of calibrating* some important parameters governing the proper behavior of the structure, such as moments of inertia, torsion modulus of the deck section, and elastic modulus of the main cable.

For the development of the analyses on the bridge, the choice was made to focus on the construction of two models of the *main span*, the constituent element for which a greater amount of data was found, and the main element of the bridge affected by flutter instability phenomena.

In particular, the following were used: a uniaxial main span model with application of specific rigid links in the deck cross-section plane, called fish-bone deck model, and a main span model consisting of two axes including rigid links in the deck cross-section plane. This "design" choice involved specific modeling of the external constraints of the deck with towers with rigid behavior and calibration with reduction of the main cable steel's elastic modulus to account for the absence of side spans in the developed models. Following the CAD representation (Figure 4-1) of the models and export in specific format (.IGES) to ANSYS, it was appropriate to define the types of elements used within the modeling. Different types of finite elements were used for numerical simulation of mechanical behavior in ANSYS APDL [55]:

- **BEAM188 element:** Timoshenko beam theory, which considers shear-deformation effects, serves as its foundation. It is a two-node, one-dimensional beam element in 3D space with six degrees of freedom at each node for three-dimensional translations and rotations. Proposed element for modeling the *main cable*, *main deck segments*, and *rigid links* at the ends of individual deck segments in transverse direction to the longitudinal development of the deck;
- **LINK180 element:** it is a 3D element that can be used for modeling cables and rigid connections in the structure. It is a uniaxial tension-compression element with three degrees of freedom per node related to translation. In particular, it is used in the proposed models for modeling *hangers* that transfer tensile stresses between the deck and the main cable;
- **MASS21 element:** it is a mass point element with a maximum of six degrees of freedom and is used to model the properties of structural mass. It allows a mass and moment of inertia to be arbitrarily assigned to a point. This element was used to properly calibrate the moment of inertia and mass of the deck by redistributing the mass density from uniform over the entire deck to discretized at the ends of the deck segments along the axis.

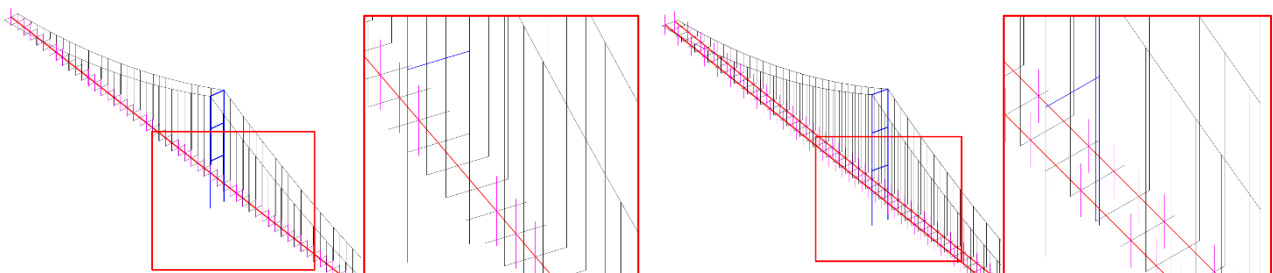


Figure 4-1: 3D representation on CAD software with details of the deck: fish-bone deck model (left); 2-axis deck model (right)



Following the definition of *material properties*, with the introduction of specific parameters such as Young's modulus, Poisson's transverse expansion coefficient and mass density, the *cross sections* of the structural elements of the bridge are introduced, such as the main cable's cross section and the dimensions of the deck through user definition of the cross section.

The most important specification that can be used in ANSYS APDL is the definition of *Real Constants*, which allows the introduction of mass and moments of inertia in MASS21 elements and the coefficients of aeroelastic matrices consisting of *flutter derivatives* within Matrix27, which are specifically defined in the dedicated section "Modeling for flutter analysis" and in Chapter 5 on analysis results.

The next phase of model building is mainly concerned with the *Meshing procedure*, within which are encompassed the definition of the subdivision size (*size controls*) of the individual finite element and the attribution of specific characteristics of the individual element subjected to the procedure (*Mesh attributes*). At the end of this process the *line entities* of which the model was composed become *elements* endowed with specific geometric and mechanical properties.

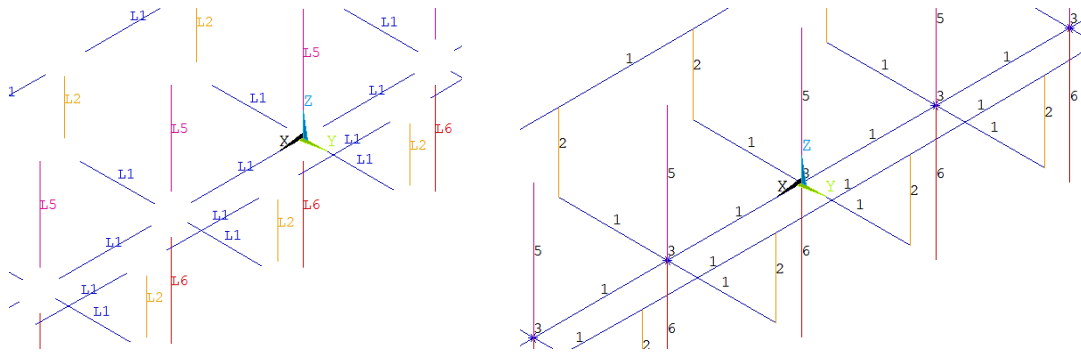


Figure 4-2: Meshing procedure: line entities (left) and elements (right)

The Meshing procedure is closely followed by the procedure for defining the structure's *external constraints*. Constraints are placed as boundary conditions on the displacements and rotations of the considered nodes: at the end nodes of the barycentric axes of the deck and at the ends of the main cable representative of the cable-tower connection (Figure 4-4, Figure 4-5). For both models developed, displacement cancellation in the three orthogonal directions is imposed and rotation around the longitudinal axis along which the bridge span is developed is cancelled. These constraints and the introduction of the MASS21 elements allow verification for the *static analysis* of the structure. To best understand the *zero-wind modal analysis* evaluations discussed in Chapter 5, it is worth considering what was said earlier about the complexity in obtaining data regarding the deck section. The procedure used to determine the mechanical characteristics of the deck section is *iterative*: following an initialization of the data [76], to determine the mass moment of inertia of the section, it was necessary to define the relationship between the torsional inertias of the *model*, *deck*, *cable*, and *mass point elements*.

$$I_{\vartheta model} = I_{\vartheta deck} + I_{\vartheta cable} + I_{xx(mass21)} \frac{n_{21}}{L} \quad (4-1)$$

The Equation 4-1 can be expressed in different form:

$$I_{xx(mass21)} = (I_{\vartheta model} - I_{\vartheta deck} - I_{\vartheta cable}) \frac{L}{n_{21}} \quad (4-2)$$

Where:

- $I_{xx(mass21)}$: mass moment of inertia which is attributed to MASS21 elements.
- $I_{\vartheta model} = 6.215 \cdot 10^6 \text{ kgm}^2/\text{m}$: model mass moment of inertia.
- $I_{\vartheta cable} = 2\rho_c A_c b^2$: it is the torsional inertia of the cables, where ρ_c is the mass density, A_c is the nominal cross-sectional area of the main cable including the wrapping, and b is the distance between the barycenter of the deck section and the barycenter of the cable section.
- $L = 2023 \text{ m}$: it is the main span length.
- n_{21} : number of MASS21 element applied in main span nodes along the axis.
- $I_{\vartheta deck} = I_{\vartheta deck}(I_{yy}, I_{zz})$: it is the (polar) mass moment of inertia of the deck. A specific tool for equivalent thin sections called "Shear and Torsion - thin section" of the *commercial software SDC* was used for this purpose.

This specific function allowed a *recursive study* of an *equivalent thin section* to identify the specific mechanical characteristics of *moments of inertia* and *torsion modulus* (I_{yy}, I_{zz}, J_t) of the deck section and then allowed the model to be calibrated in order to determine vibration frequencies as close as possible to the values found in the research literature [76].

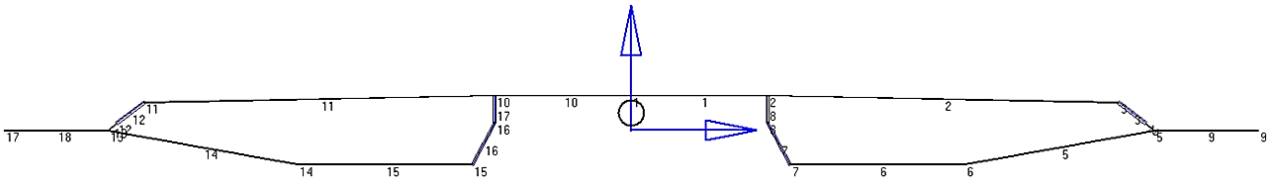


Figure 4-3: Example of evaluation of the mechanical properties of the section using SDC software

In the iterative procedure, the thicknesses of the equivalent elements forming the aerodynamic section of the deck are varied at each calculation step using the SDC software, and at the same time a change in the *cable's "equivalent" elastic modulus* is made (Figure 4-3). Having modeled only the central span, the contribution of the side spans is considered through a reduction in the elastic modulus. The equivalent modulus is thus one of the parameters used to fit the natural vibration frequencies of the bridge.

The *convergence* of the method resulted in correctly fitting the natural frequencies for both models and thus reliably determining the mechanical characteristics of the deck section.

4.1 Fish-bone deck model

This model is named "fish-bone" because it presents the modeling of the deck concentrated along a *barycentric central axis*, which is assigned equivalent properties for the two twin-box girders. The centroidal axis is thus connected to the *hangers* by the introduction of *transverse beams* that serve as rigid connections between these main structural elements. The *main cable* was modeled with a system of multiple beam element segments to form a catenary one on each side of the deck, with a nominal diameter of 869 mm, including the 144 wire strands and wrapping.

The representative stiff elements of the transverse beams, which are defined with high inertia to achieve rigid bending behavior and have weight set to zero, as well as the deck segments and main cables are all modeled using BEAM188 elements. The LINK180 elements used to model the hangers, on the other hand, only transmit the tensile forces between the deck and the main cables. The mass moment of inertia of the deck is lastly represented using the MASS21 element, placed at the intersection points between the barycentric axis and the transverse rigid links ($n_{21} = 83$).

The deck is further restrained by hinges, which allow rotation in all directions other than around the longitudinal axis, where it is prohibited, but which prevent displacements in the x, y, and z directions.

The model's geometrical and mechanical characteristics are displayed in the Table 4-1 and the graphical representation of the model built on the ANSYS software is shown in Figure 4-4.

Fish-bone deck model

Span length (m)	2023
Total deck width (m)	45.06
Sag (m)	228
Main cable area ($\Phi_{nom} = 869 \text{ mm}$) (m^2)	0.593
Distance between hangers (m)	24
Cable Young modulus (N/m^2)	$2.83\text{E}+10$
Poisson coefficient	0.3
Equivalent vertical moment of inertia, I_{zz} (m^4)	419.6
Equivalent lateral moment of inertia, I_{yy} (m^4)	5.7
Equivalent torsion modulus, J_t (m^4)	15.21
Deck mass per unit length (kg/m)	28853
MASS X, Y, Z (mass values for MASS21 elem.) (kg)	466367
I_{xx} (MASS21) (kgm^2)	$6.34\text{E}+07$

Table 4-1: Properties of the 1915Çanakkale Bridge fish-bone deck model

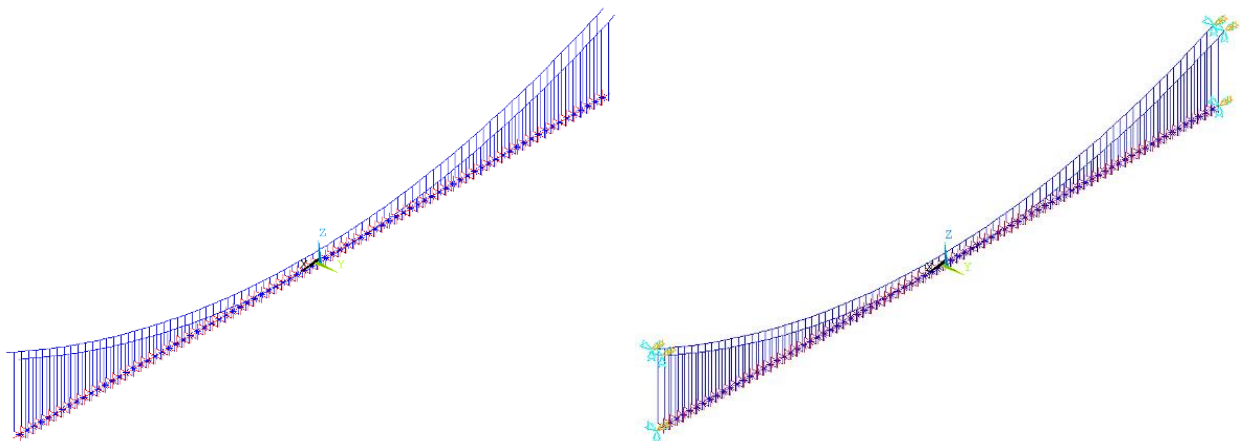


Figure 4-4: 3D main span fish-bone deck model (left); Fish-bone model constraints (right)

4.2 Two-axis deck model

In analogy with the fish-bone model introduced in the previous section, this model respects the discretization of the deck along the barycentric axis but subdivides the masses symmetrically (in this case it is a symmetrical section) by concentrating them at the barycenter of the two individual box girders constituting the twin-box deck section. In this case, the two centroidal axes are interconnected and connected to the hangers by the introduction of transverse girders that act as rigid connections between these main structural elements. Also, for this model, the main cable was modeled with a system of segments of multiple beam elements to form a catenary one on each side of the deck, with a nominal diameter of 869 mm, including the 144 wire strands and wrapping.

BEAM188 elements are used to model the representative stiff elements of the transverse beams, defined with high inertia to achieve rigid flexural behavior and with weight set to zero, as well as the deck segments and main cables. The LINK180 elements used to model the hangers, on the other hand, transmit only the tensile forces between the deck and the main cables. Finally, the mass moment of inertia of the deck is represented with the MASS21 elements, placed at the intersection points between the barycentric axes and the transverse rigid links ($n_{21} = 166$).

Additionally, hinges that permit rotation in all directions except around the longitudinal axis, where it is prohibited, but prevent displacement in the x, y, and z directions further restrict the deck's movement. Table 4-2 displays the model's geometrical and mechanical characteristics, and Figure 4-5 displays a graphic representation of the model created using ANSYS software.

Two-axis deck model

Span length (m)	2023
Total deck width (m)	45.06
Sag (m)	228
Main cable area ($\Phi_{nom} = 869 \text{ mm}$) (m^2)	0.593
Distance between hangers (m)	24
Cable Young modulus (N/m^2)	2.43E+10
Poisson coefficient	0.3
Equivalent vertical moment of inertia, I_{zz} (m^4)	0.24
Equivalent lateral moment of inertia, I_{yy} (m^4)	0.89
Equivalent torsion modulus, J_t (m^4)	0.079
Deck mass per unit length (kg/m)	28853
MASS X, Y, Z (mass values for MASS21 elem.) (kg)	233184
I_{xx} (MASS21) (kgm^2)	-1.96E+06

Table 4-2: Properties of the 1915Çanakkale Bridge two-axis deck model

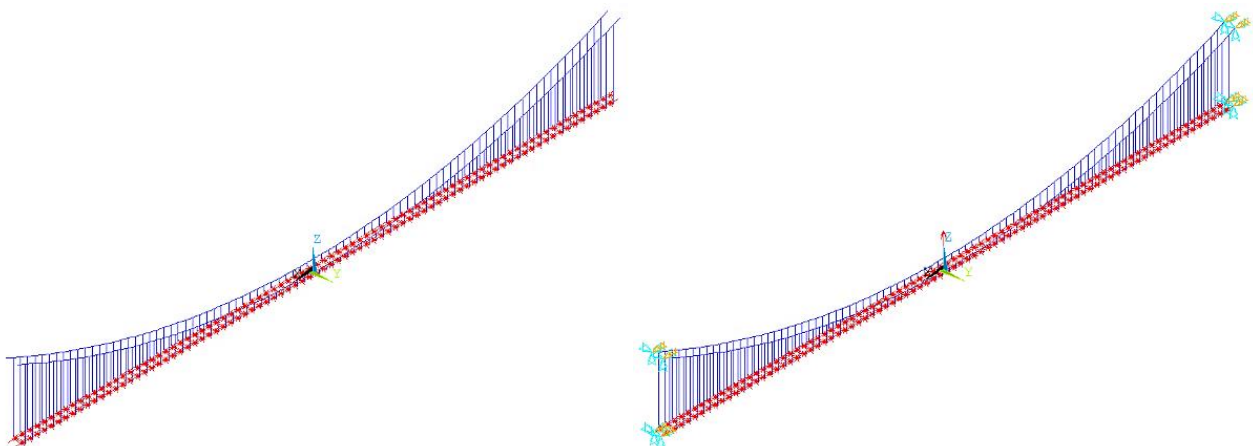


Figure 4-5: 3D main span two-axis deck model (left); Two-axis model constraints (right)



Modeling for flutter analysis

The results of the *modal analyses* performed on the two developed models (results available in Chapter 5) showed higher modeling accuracy for the fish-bone deck model than for the two-axis deck model.

This can be ascribed to the fact that the *model calibration* is easier when the number of free parameters is lower (non all data were available). The fish-bone model was therefore selected to be tested with aerodynamic forces, since the relative error found in natural frequencies was lower than the results obtained with the second model, especially in the torsion (TS) and vertical bending (VS) modes, since they are more representative of the *classical flutter*. Prior to the flutter analyses, it was necessary to introduce *Matrix27 elements*. As seen previously in Chapter 2, ANSYS Matrix27 user-defined element is an adaptable element with two nodes that each have six degrees of freedom and whose local coordinate system matches the global coordinate system. The stiffness, mass, and damping coefficients define the element's properties, while the element's geometric configuration is arbitrary. Due to the motion-dependent nature of aeroelastic forces, the Matrix27 element must be used to represent the fundamental *stiffness* and *damping aeroelastic matrices*. As a way to simulate the aeroelastic forces, two Matrix27 elements are attached to each node of a generic bridge deck *hybrid element model*, as shown in Figure 2-15 and Figure 4-6. The element can only model either an *aeroelastic stiffness matrix* or an *aeroelastic damping matrix*, but not both simultaneously.

The aeroelastic stiffness and damping of the node i are represented by the Matrix27 elements e_1 and e_3 after defining the fictitious node k while the node j is represented by the Matrix27 elements e_2 and e_4 after defining the fictitious node l , respectively [53].

Accordingly, the two hybrid Matrix27 elements defined in ANSYS, separately for aeroelastic stiffness and aeroelastic damping, are introduced at each of the nodes located on the central axis of the bridge and are fully constrained at the ends. Figure 4-6 shows a portion of the bridge deck for the fish-bone model and the graphical representation of the introduced Matrix27 [43].

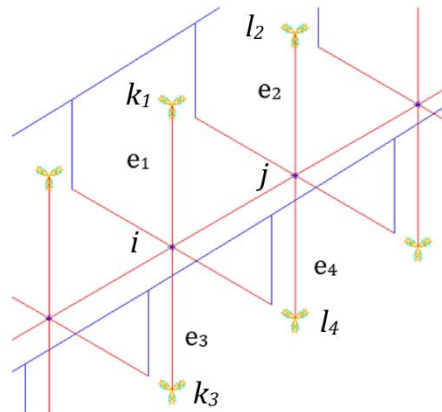


Figure 4-6: Matrix27 for flutter analysis in ANSYS model

To calculate the *flutter velocity* and corresponding *flutter frequency*, *flutter derivatives* obtained experimentally in wind tunnel tests on appropriate scale models of the deck or complete bridge are needed. Data provided by research conducted in China and Denmark allowed partial retrieval of the most relevant flutter derivatives and are reported in Chapter 5.



CHAPTER 5 Comparison between analytical and FE models

The concept of *flutter instability* has been introduced on several occasions, and this chapter includes an overview of the analyses conducted on the 1915Çanakkale Bridge concerning this key theme of structural and wind engineering.

The first part of this important chapter introduces two influential research studies conducted in academia and business in *China* and *Denmark*, respectively. These studies provided important data necessary for model calibration to ultimately understand the dynamic wind-structure interaction for this important structural artwork.

In the following section, some specifics of the analyses conducted using two well-known commercial software, such as ANSYS APDL and MATLAB, are introduced. As anticipated in Chapter 2, the analyses consist of the study of the bridge deck using *zero-wind modal analysis* to determine the natural frequencies of the bridge and understand its behavior and calibration in relation to the studies conducted by the other research groups.

The successive *flutter analyses* are based on data from the *flutter derivatives* that have been appropriately calibrated to account for the different adimensionalizations adopted in order to make the values obtained from the studies in the literature comparable, and interpolated as a function of *reduced velocity* to determine the precise values of the flutter derivatives in relation to a predetermined wind speed. For both the case of zero-wind modal analysis and flutter analysis, the comparison between the data obtained (in ANSYS and MATLAB) and the values found in the literature is proposed.

The last section of Chapter 5 puts forward an additional calculation method. This is the *single-mode criterion*, also known as the simplified one-DOF flutter analysis, originally proposed by *Scanlan* [77] and later extended by *A. Namini* and *P. Albrecht* [51] to a finite element framework. This approach, based on matrices and eigenvectors extracted from ANSYS APDL and implemented on MATLAB, allowed the specific nature of the bridge deck to be revealed.

5.1 Literature studies

The most relevant literature data concern *flutter derivatives* that are provided by the studies mentioned above and taken up in detail in the following sections. Flutter derivatives, obtained in the wind tunnel in experimental form, provide insight into the behavior of the bridge deck. The historical evolution of long-span suspension bridges since the 1940s has led to profound changes in the structure and shape of the deck, progressively moving to aerofoil box sections with tangible changes in the graphs of flutter derivatives that allow to understand this important evolution.

Figure 2-10 shows an example of flutter derivatives for different types of historic bridge decks as a function of reduced velocity U_r , already defined in the section 2.1 as:

$$U_r = \frac{U}{fB} = \frac{2\pi}{K} \quad (5-1)$$

Checking the flutter derivatives A_2^* and H_1^* , which govern the *torsional* and *vertical* components of the flutter, respectively, allows an initial assessment of the flutter behavior of the section.

Denoted by the number "1" in Figure 2-13, the Tacoma Narrows bridge, which collapsed in 1940, has values of H_1^* that remain positive even for high reduced velocities and thus enjoys negligible vertical instability. The value of A_2^* , initially negative, then takes on positive values instead, and as a result the



total damping $c_{\alpha, tot}$ becomes negative (dynamic self-excitation) and the torsional flutter phenomenon turns out to be the only oscillatory mode to occur. This phenomenon occurred for a very small U_r values. In general, it can be observed that for the most innovative suspension bridges, as in the case of the 1915Çanakkale Bridge, the flutter derivatives A_2^* and H_1^* are negative overall increasing the total damping $c_{\alpha, tot}$ and consequently providing high stability against flutter.

The next sections are aimed at presenting data obtained from the experimental and analytical studies conducted in *China* and *Denmark*.

5.1.1 Chinese study: Liao-Wang

The 1915Çanakkale Bridge's aerodynamic behavior was investigated by *Southwest Jiaotong University* and the *Wind Engineering Key Laboratory of Sichuan Province in Chengdu, China*. Modern long-span suspension bridges were taken into consideration as *H. Liao, Q. Wang* and their research team [78] addressed the issue of flutter. The nonlinear aerostatic effect is frequently ignored in conventional flutter analyses. They suggest a multimodal flutter analysis method and the investigation of the impact of the additional angle of attack brought on by the nonlinear aerostatic effect on the flutter derivatives in their experimental analysis.

The analysis of the *deck sectional model* and the *full bridge model* allowed for the identification of the *flutter derivatives* with various attack angles (Figure 5-1, Figure 5-2) and *critical wind speed*, respectively. The test on sectional model was conducted in the wind tunnels at the Wind Engineering Key Laboratory, and the model's scale ratio was set at 1:130. While the full bridge aeroelastic model wind tunnel test is conducted on a 1:190 scaled model (Figure 5-3) and allowed identification of the *flutter velocity* for different angles of attack. These include a *flutter velocity* close to 83 m/s under the 0° angle of attack. The results support the proposed discussion by showing that the critical flutter velocity is more consistent with the onset of flutter when the nonlinear aerostatic effect is considered.

The results of this study demonstrate that the critical wind speed of flutter, when considering the nonlinear aerostatic effect, is more in line with the onset speed determined from full model aeroelastic tests. The main span of the 1915Çanakkale Bridge is 2023 meters, which makes it extremely slender and more flexible than any previous bridge, and has a more pronounced nonlinear aerostatic effect. As a result, this nonlinear aerostatic effect should be considered in the flutter analysis of suspension bridges with exceptionally long spans.

The additional information on the bridge's *mechanical properties* (Table 5-1), such as the deck mass per unit length and the mass moment of inertia, as well as the data on *natural frequencies* (Table 5-2) discovered in the experimental studies provided by *Q. Wang* [76], then, made it possible to conduct an in-depth study of the bridge's characteristics and to calibrate the developed models effectively.

Flutter derivatives are shown in the graphs as a function of *reduced velocity* U_r on the horizontal axis.

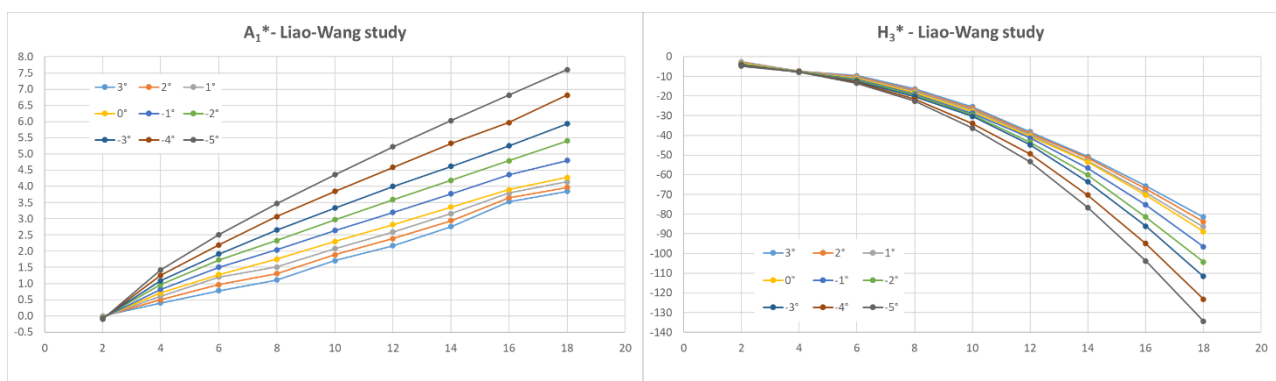


Figure 5-1: Flutter derivatives of Liao-Wang study in China (A_1^* , H_3^*) [78]

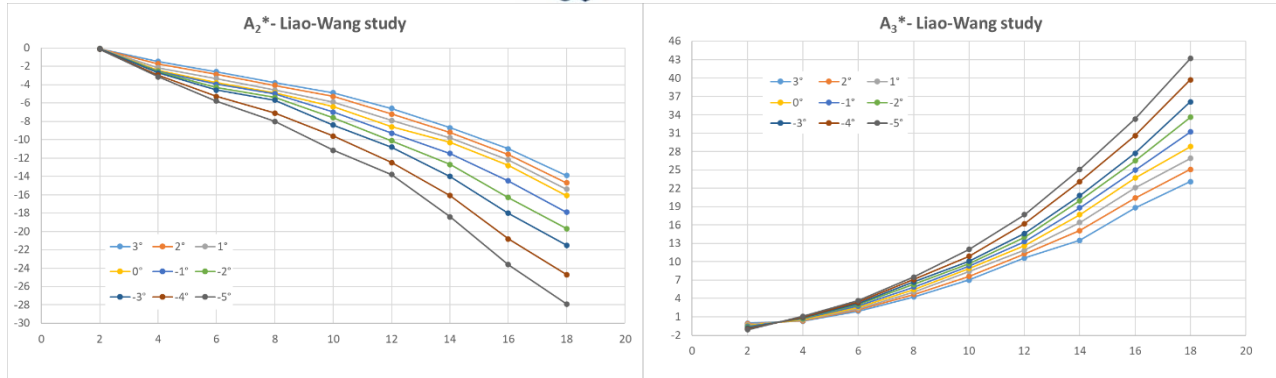
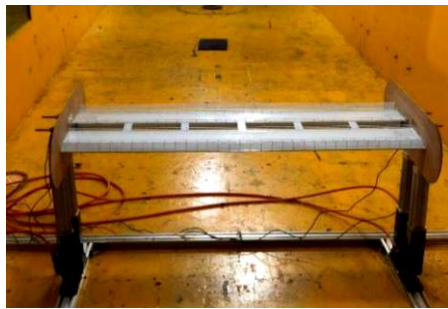
Figure 5-2: Flutter derivatives of Liao-Wang study in China (A_2^* , A_3^*) [78]

Figure 5-3: Deck sectional model (scale ratio at 1:130) (left); Full-bridge model (scale ratio at 1:190) (right) [78]

Item	Prototype	Model (required value)	Model (measured value)	Error (%)
Vertical Frequency (Hz)	0.072	0.992	0.969	-2.37
Torsional Frequency (Hz)	0.146	2.012	2.029	0.82
Mass (kg/m)	28853	799.25×10^{-3}	799.25×10^{-3}	/
Mass Moment of Inertia ($\text{kg} \times \text{m}^2/\text{m}$)	6.215×10^6	4.77×10^{-3}	4.77×10^{-3}	/
Vertical Damping Ratio	/	/	0.40%	/
Torsional Damping Ratio	/	/	0.52%	/

Table 5-1: Mechanical properties provided by Liao-Wang study [76]

Mode	frequency [Hz]	Mode description	Mode type
1	0.0456	Symmetric LATERAL BENDING mode	LAT-SYM
2	0.0724	Symmetric VERTICAL BENDING mode	VERT-SYM
3	0.0823	Asymmetric VERTICAL BENDING mode	VERT-ASYM
4	0.1004	Asymmetric LATERAL BENDING mode	LAT-ASYM
5	0.1120	2 nd order Symmetric VERTICAL BENDING mode	VERT-SYM-II
6	0.1472	Symmetric TORSIONAL mode	TORS-SYM

Table 5-2: Natural frequencies of 1915Çanakkale Bridge provided by Liao-Wang study [76]



5.1.2 Danish study: Rønne-Larsen

A close collaboration between COWI's Department of Bridges International and the Department of Mechanical Engineering at Technical University of Denmark has produced important results on the study of dynamic wind-structure interaction.

These researchers' study looked into how applying *wind screens* to suspension bridges changed their behavior and boosted their performance. A 2000 m class *twin-box section* suspension bridge's wind tunnel tests showed how wind screens make it possible to achieve higher critical wind speeds than a deck with similar characteristics but no wind screens. This positive effect contributed by windscreens is in contrast to what A. Larsen [79] pointed out in 1993 regarding streamlined *trapezoidal single box deck sections*: in fact, the placement of screens along the edges of the beam showed results in a reduction in flutter wind speed compared to the deck without wind screens.

The Danish approach also demonstrated a *nose-up effect*: the dynamic interaction leading to the twisting of the deck with respect to the horizontal generates an increase in the critical flutter velocity for very high wind speeds, which gives good margins of structural safety. The research work conducted on the 1915Çanakkale Bridge aimed to study the results of wind tunnel tests on scaled models to better understand the nose-up effect phenomenon and to establish a theoretical model based on numerical simulations to predict the flutter for the two-box bridge girder.

The study conducted by M. Rønne and A. Larsen [64] on *flutter derivatives*, initially proposed by Scanlan and Tomko [47], sets forth a well-established formulation of the aerodynamic loads induced by wind bending and rotational motion (lift L_{ae} and moment M_{ae}) acting on a two-dimensional cross section.

The 8 total flutter derivatives are computed within the research work shown (Figure 5-4, Figure 5-5).

In the paper [64] it is described how, as a function of reduced velocity U_r and mean rotation angle θ , the flutter derivatives in small amplitude harmonic motion can be expressed as *polynomials*. The aerodynamic derivatives for $\theta = 0^\circ$ are assumed to be approximated by polynomials, whereas the aerodynamic derivatives for various angles are obtained by multiplying the same polynomial expression by the factor of $\frac{dC_L}{d\theta}\big|_\theta / \frac{dC_L}{d\theta}\big|_{\theta=0}$ or $\frac{dC_M}{d\theta}\big|_\theta / \frac{dC_M}{d\theta}\big|_{\theta=0}$.

In line with this concept, the expressions for the 1915Çanakkale twin-box suspension bridge's flutter derivatives, $A_i^*(U_r, \theta)$ and $H_i^*(U_r, \theta)$ ($i = 1, \dots, 4$), are expressed as functions of reduced velocity U_r and mean rotation θ :

$$\begin{aligned}
 H_1^*(U_r, \theta) &= \frac{\frac{dC_L}{d\theta}\big|_\theta}{\frac{dC_L}{d\theta}\big|_{\theta=0}} (a_{H_1^*} U_r^2 + b_{H_1^*} U_r) & H_2^*(U_r, \theta) &= \frac{\frac{dC_L}{d\theta}\big|_\theta}{\frac{dC_L}{d\theta}\big|_{\theta=0}} (a_{H_2^*} U_r^2 + b_{H_2^*} U_r) \\
 A_1^*(U_r, \theta) &= \frac{\frac{dC_M}{d\theta}\big|_\theta}{\frac{dC_M}{d\theta}\big|_{\theta=0}} (a_{A_1^*} U_r^2 + b_{A_1^*} U_r) & A_3^*(U_r, \theta) &= \frac{\frac{dC_M}{d\theta}\big|_\theta}{\frac{dC_M}{d\theta}\big|_{\theta=0}} (a_{A_3^*} U_r^2 + b_{A_3^*} U_r) \\
 H_2^*(U_r, \theta) &= \frac{\frac{dC_L}{d\theta}\big|_\theta}{\frac{dC_L}{d\theta}\big|_{\theta=0}} (a_{H_2^*} U_r^2 + b_{H_2^*} U_r) & H_4^*(U_r, \theta) &= \frac{\frac{dC_L}{d\theta}\big|_\theta}{\frac{dC_L}{d\theta}\big|_{\theta=0}} (a_{H_4^*} U_r^2 + b_{H_4^*} U_r) \\
 A_2^*(U_r, \theta) &= \frac{\frac{dC_M}{d\theta}\big|_\theta}{\frac{dC_M}{d\theta}\big|_{\theta=0}} (a_{A_2^*} U_r^2 + b_{A_2^*} U_r) & A_4^*(U_r, \theta) &= \frac{\frac{dC_M}{d\theta}\big|_\theta}{\frac{dC_M}{d\theta}\big|_{\theta=0}} (a_{A_4^*} U_r^2 + b_{A_4^*} U_r)
 \end{aligned} \tag{5-2}$$

Where $(a_j U_r^2 + b_j U_r)$ with $j = A_{1,\dots,4}^*, H_{1,\dots,4}^*$ are obtained from fitting of second order polynomials to the aerodynamic derivatives obtained from numerical simulations for deck section.



Flutter derivatives are displayed in the graphs as a function of reduced velocity U_r on the horizontal axis.

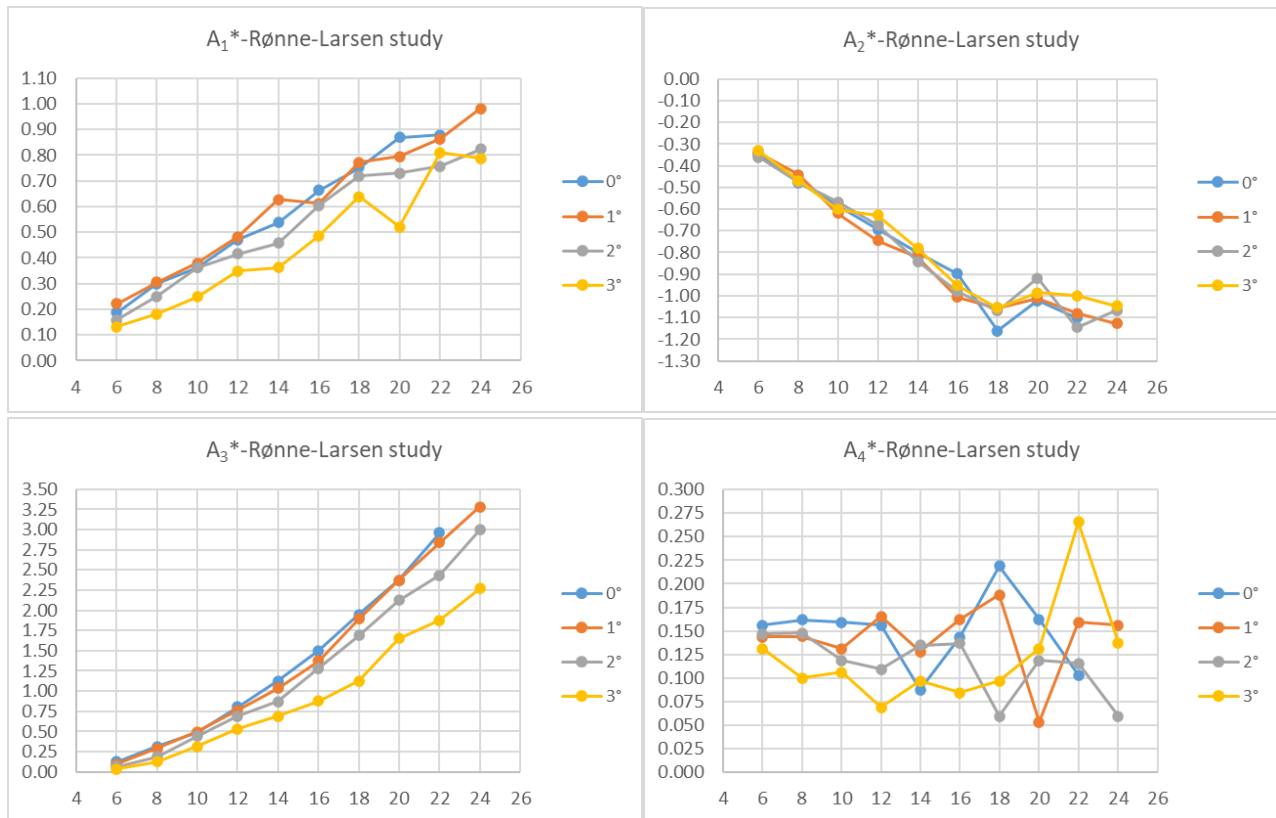


Figure 5-4: A_i^* flutter derivatives provided by Rønne-Larsen study in Denmark [64]

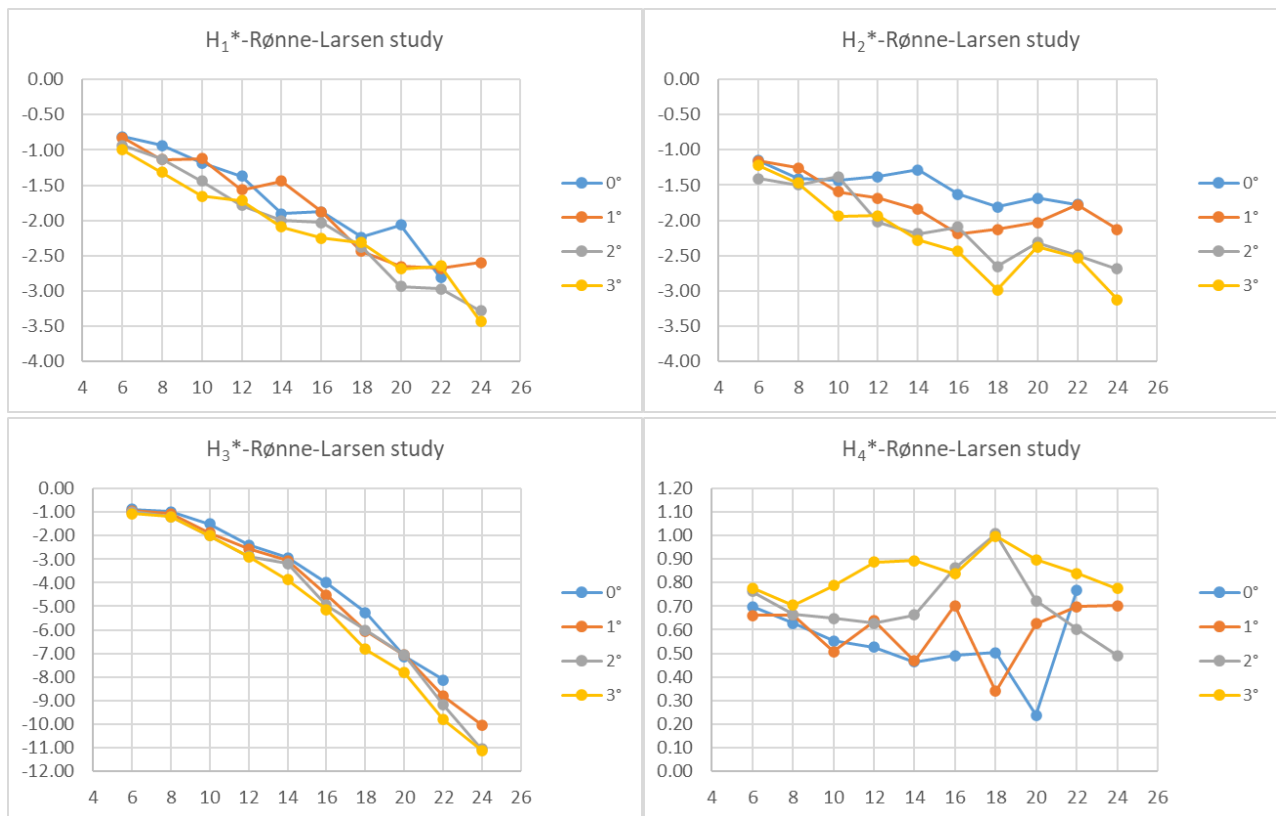


Figure 5-5: H_i^* flutter derivatives provided by Rønne-Larsen study in Denmark [64]



At the *Boundary Layer Wind Tunnel Laboratory of the University of Western Ontario (Canada)* static and dynamic wind tunnel tests of the bridge deck were used to examine the Dardanelles suspension bridge's behavior. Figure 5-6 shows a 2.286 m long section model built in 1:60 geometric scale: it was used for the tests, which were conducted in regular intensity flow. The scaled model is used to determine steady-state aerodynamic coefficients, also known as *static polars*, which are subsequently employed in the calculation of the *flutter derivatives* (Equations 5-2).

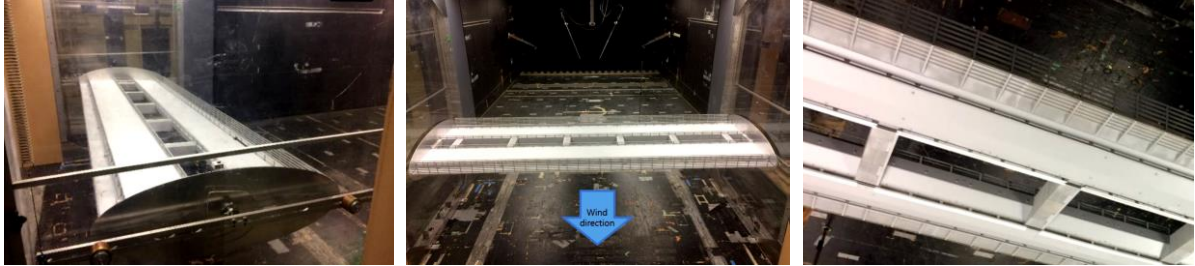


Figure 5-6: Sectional model including wind screens (scale ratio at 1:60) [64]

Regarding the estimation of the *critical flutter condition*, the authors give the estimated flutter velocity for some values of angle of attack, omitting the corresponding flutter frequencies. The knowledge of the estimated flutter velocity of 88 m/s under the 0° angle of attack is relevant for the research done in this thesis. The authors go into detail about how the *Air Material Command method (AMC)*, which *Scanlan* and *Rosenbaum* [80] introduced in 1962, can be used to determine this wind speed. The estimation of flutter velocity is shown in Figure 5-7, wherein critical flutter velocity is established using this calculation criterion by balancing the *apparent aerodynamic damping* g with twice the *structural damping* $2\zeta_s$ of the deck.

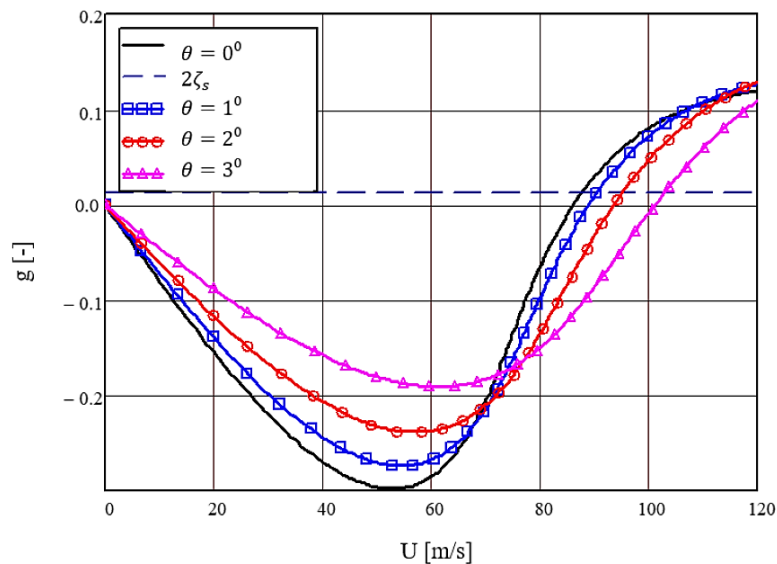


Figure 5-7: Flutter estimated velocities as function of attack angles [64]



5.2 Zero-wind Modal Analysis

As pointed out in Chapter 4, it is important to keep in mind what was said earlier about the method used to determine the mechanical properties of the deck section in order to fully comprehend the evaluations of the *zero-wind modal analysis*. Both models constructed from an initialization of the data underwent this *iterative procedure*, which was required at the final stage of the *calibration* of the models [76].

To determine the mass moment of inertia of the deck section, it was necessary to define the relationship between the torsional inertias of the model, the deck, the cable, and the mass point elements.

In the iterative procedure used for the overall determination of the inertial parameters of the deck section, i.e. $I_{\vartheta_{deck}} = I_{\vartheta_{deck}}(I_{yy}; I_{zz})$, the thicknesses of the equivalent rectangular elements forming the overall aerodynamic section of the deck are varied at each calculation step using the *SDC software*, and at the same time a variation of the main cable's "equivalent" elastic modulus E_{cable} is made.

This variation of the elastic modulus allows modeling of the central span only, considering the contribution of the lateral spans through a reduction of the elastic modulus itself. By carrying out the modal analysis iteratively, it was possible to highlight how the individual modes of vibration depend mainly on a single inertial parameter:

- I_{zz} : equivalent vertical moment of inertia;
- I_{yy} : equivalent lateral moment of inertia;
- J_t : equivalent torsion modulus;
- E_{cable} : equivalent cable Young modulus.

The convergence of the method made it possible to correctly adjust the *natural frequencies* of both models, thus reliably determining the mechanical characteristics of the bridge section (given in Table 4-1 and Table 4-2) and making the models "operational" for subsequent *flutter analyses*. The following are the numerical results for the *fish-bone deck model* and the *two-axis deck model*.

5.2.1 Numerical fish-bone deck model in ANSYS

Calibration of the fish-bone deck model in ANSYS revealed the dependence of the individual frequencies associated with the natural modes of vibration on the specific parameters used:

- An increase in I_{zz} causes an increase in the frequencies of LAT-SYM and LAT-ASYM modes.
- An increase in I_{yy} causes an increase in the frequencies of VERT-SYM and VERT-ASYM modes.
- An increase in J_t causes an increase in the frequency of TORS-SYM and TORS-ASYM modes.
- An increase in E_{cable} causes an increase in the frequencies of VERT-SYM, VERT-SYM-II and TORS-SYM modes.

Table 5-3 shows the results of the zero-wind modal analysis performed on ANSYS software. These natural frequency values are compared with reference values, i.e., the frequency data provided by the Liao-Wang study [78] and shown in Table 5-2. The comparison is limited to the first *six modes of vibration of the structure*.

Mode	Fish-bone freq. [Hz]	Liao-Wang freq. [Hz]	Δ Fish-bone [%]	Mode type
1	0.0416	0.0456	-8.77%	LAT-SYM
2	0.0728	0.0724	+0.55%	VERT-SYM
3	0.0792	0.0823	-3.77%	VERT-ASYM
4	0.1086	0.1004	+8.17%	LAT-ASYM
5	0.1157	0.1120	+3.30%	VERT-SYM-II
6	0.1474	0.1472	+0.14%	TORS-SYM

Table 5-3: Natural frequencies for the 1915Çanakkale Bridge fish-bone deck model



For the *fish-bone deck model*, the natural modes of vibration and associated frequencies are represented graphically in Figure 5-8, Figure 5-9 and Figure 5-10.

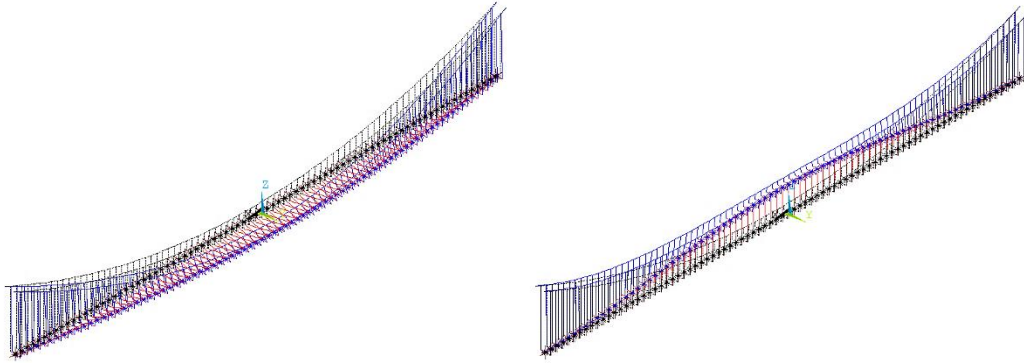


Figure 5-8: fish-bone deck model: Mode 1, LAT-SYM, $f=0.0416$ Hz (left); Mode 2, VERT-SYM, $f=0.0728$ Hz (right)

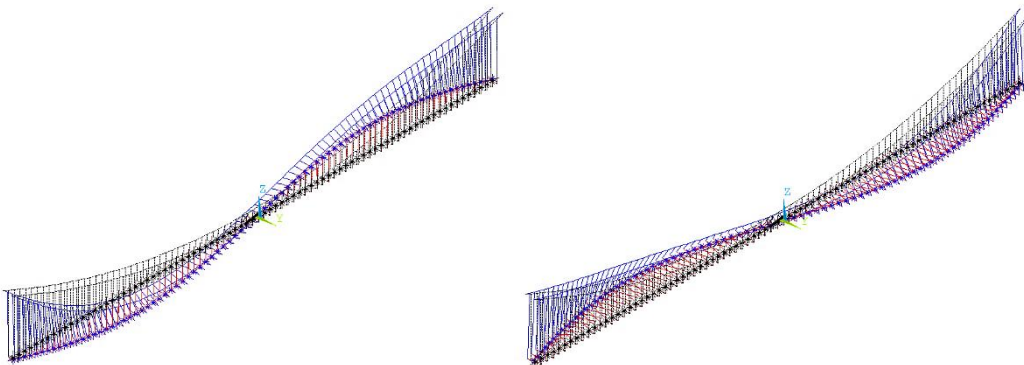


Figure 5-9: fish-bone deck model: Mode 3, VERT-ASYM, $f=0.0792$ Hz (left); Mode 4, LAT-ASYM, $f=0.1086$ Hz (right)

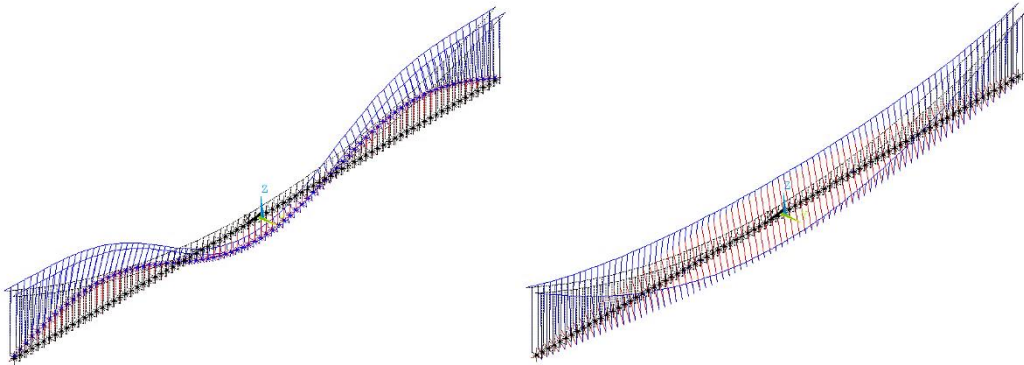


Figure 5-10: fish-bone deck model: Mode 5, VERT-SYM-II, $f=0.1157$ Hz (left); Mode 6, TORS-SYM, $f=0.1474$ Hz (right)

5.2.2 Numerical two-axis deck model in ANSYS

Also in the calibration of two-axis deck model in ANSYS the dependence of the individual frequencies associated with the natural modes of vibration on the specific parameters used is highlighted:

- An increase in I_{zz} causes an increase in the frequencies of LAT-SYM and LAT-ASYM modes.
- An increase in I_{yy} causes an increase in the frequencies of VERT-SYM, VERT-ASYM and TORS-SYM modes.
- An increase in J_t causes an increase in the frequency of TORS-SYM and TORS-ASYM modes.
- An increase in E_{cable} causes an increase in the frequencies of VERT-SYM, VERT-SYM-II and TORS-SYM modes.



Table 5-4 shows the results of the zero-wind modal analysis performed on ANSYS software. These natural frequency values are compared with reference values, i.e., the frequency data provided by the Liao-Wang study [78] and shown in Table 5-2. The comparison is limited to the first six *modes of vibration of the structure*.

Mode	Two-axis freq. [Hz]	Liao-Wang freq. [Hz]	Δ Two-axis [%]	Mode type
1	0.0489	0.0456	+7.24%	LAT-SYM
2	0.0698	0.0724	-3.59%	VERT-SYM
3	0.0782	0.0823	-4.98%	VERT-ASYM
4	0.1002	0.1004	-0.20%	LAT-ASYM
5	0.1141	0.1120	+1.87%	VERT-SYM-II
6	0.1477	0.1472	+0.34%	TORS-SYM

Table 5-4: Natural frequencies for the 1915Çanakkale Bridge two-axis deck model

For the *two-axis deck model*, the natural modes of vibration and associated frequencies are represented graphically in Figure 5-11, Figure 5-12 and Figure 5-13.

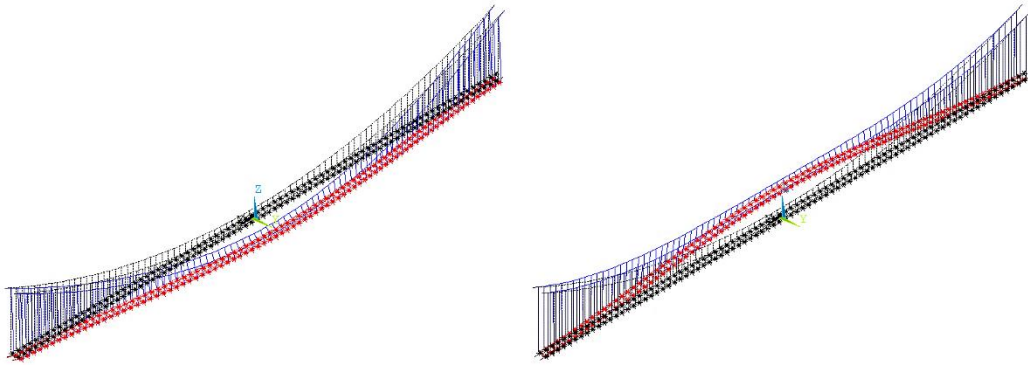


Figure 5-11: two-axis deck model: Mode 1, LAT-SYM, $f=0.0489$ Hz (left); Mode 2, VERT-SYM, $f=0.0698$ Hz (right)

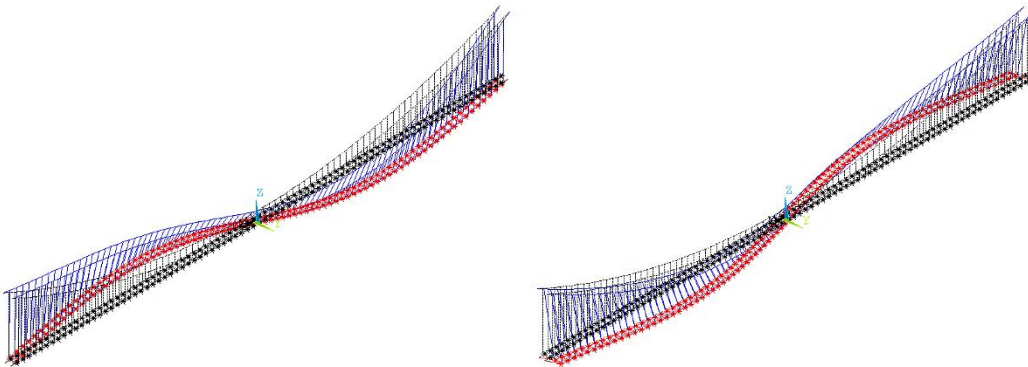


Figure 5-12: two-axis deck model: Mode 3, VERT-ASYM, $f=0.0782$ Hz (left); Mode 4, LAT-ASYM, $f=0.1002$ Hz (right)

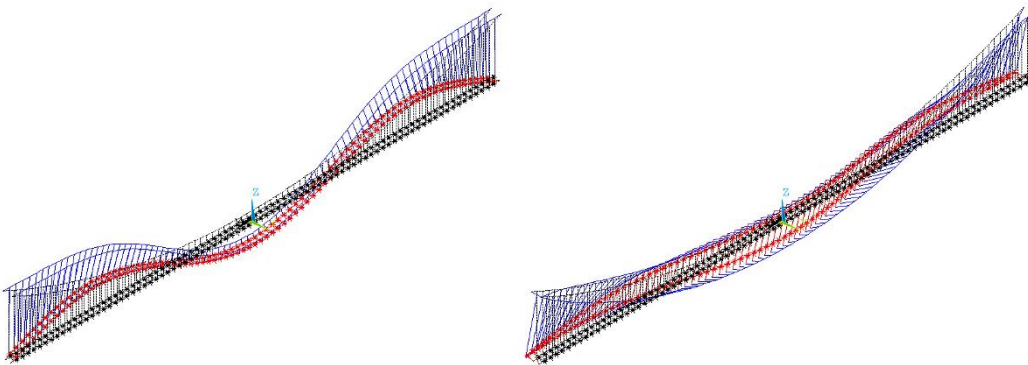


Figure 5-13: two-axis deck model: Mode 5, VERT-SYM-II, $f=0.1141$ Hz (left); Mode 6, TORS-SYM, $f=0.1477$ Hz (right)



5.2.3 Analytical model in MATLAB

The vertical and torsional displacement components are described by Equations 5-3 and 5-4, respectively, and eight sinusoidal functions were selected to describe them: $m = n = 8$, resulting in the extraction of sixteen modes [43].

$$V(x, t) = \sum_{r=1}^{2N} v_r(z) e^{\lambda_r t} \quad (5-3)$$

$$T(x, t) = \sum_{r=1}^{2N} \vartheta_r(z) e^{\lambda_r t} \quad (5-4)$$

Only the first eight modes, though, are described in this study.

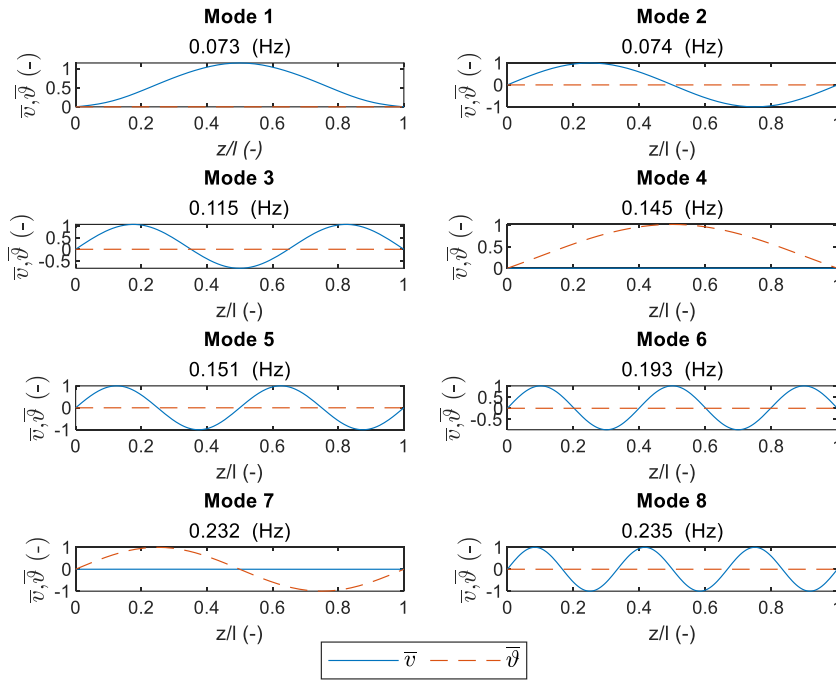


Figure 5-14: 1915Çanakkale Bridge's modal shapes in zero-wind condition (MATLAB)

Table 5-5 shows the results of the zero-wind modal analysis performed on MATLAB software. These natural frequency values are compared with reference values, i.e., the frequency data provided by the Liao-Wang study [78] and shown in Table 5-2. The comparison is limited to the first *ten modes of vibration of the structure*, excluding local modes.

Mode	MATLAB freq. [Hz]	Liao-Wang freq. [Hz]	Δ MATLAB [%]	Mode type
1	-	0.0456	-	LAT-SYM
2	0.0732	0.0724	+1.10%	VERT-SYM
3	0.0741	0.0823	-9.96%	VERT-ASYM
4	-	0.1004	-	LAT-ASYM
5	0.1151	0.1120	+2.77%	VERT-SYM-II
6	0.1453	0.1472	-1.29%	TORS-SYM
8	0.1509	-	-	VERT-ASYM-II
12	0.1932	-	-	VERT-SYM-III
15	0.2324	-	-	TORS-ASYM
16	0.2351	-	-	VERT-ASYM-III

Table 5-5: Natural frequencies for the 1915Çanakkale Bridge in MATLAB



5.3 Flutter analysis

Flutter instability phenomenon can be considered a rare but extremely dangerous event in which the bridge structure faces a dynamic instability situation by oscillating divergently and destructively at a critical wind speed. By experts in the field of structural and wind engineering, *flutter is considered the most dangerous among the various aeroelastic instabilities*.

As anticipated in section 2.4, flutter analysis aims to predict the *minimum critical wind speed* that causes the flutter instability, as well as the associated *flutter frequency*, effectively determining the known *flutter couple* that leads to structural collapse. The results of the zero-wind *modal analyses* performed on the two developed models, observed in section 5.2, showed higher modeling accuracy for the fish-bone deck model than for the two-axis one. The fish-bone model was therefore selected to be tested with aerodynamic forces, since the relative error found in natural frequencies respect to the reference data [76] was lower than the results obtained with the second model, especially in the torsion (TS) and vertical bending (VS) modes, since they are more representative of the *classical flutter*.

In addition, for this type of analysis several computational approaches are proposed using ANSYS and MATLAB as reference software.

5.3.1 Numerical flutter assessment in ANSYS

The calculation model, developed by Chinese researchers X.G. Hua and Z.Q. Chen in 2008 [52] and first presented in 2007 [53], proposes a method to analyze *coupled and uncoupled flutter of long-span bridges* by using *flutter derivatives* measured from wind tunnel tests on sectional bridge models.

As anticipated in Chapters 2 and 4 on theoretical aspects of the computational model in ANSYS and effective modeling on the software, respectively, the approach is based on the definition of aeroelastic loads using a specific user-defined element in ANSYS, namely *Matrix27*.

It is well to remember how the Matrix27 element is linked to the motion-dependent nature of aeroelastic forces: in this way the Matrix27 element must be used to represent the fundamental *stiffness* and *damping aeroelastic matrices*. To simulate the aeroelastic forces, two Matrix27 elements are attached to each node of a generic bridge deck *hybrid element model* (Figure 4-6).

The proposed flutter analysis is an *iterative method*, as already seen in the section "Algorithm implementation in ANSYS" in Chapter 2, based on a *Damped complex eigenvalue analysis*, i.e., a damped modal analysis, which aims to identify complex eigenvalues, whose *real* and *imaginary parts* represent the *damping factor* and *damped vibration frequency*, respectively.

These complex eigenvalues are studied in relation to wind speed, which allows the identification of the critical condition in which wind becomes the determining action in structural collapse.

In fact, it is found that at a certain *wind speed*, the system can exhibit a complex eigenvalue with a *real part that is zero or close to zero* and an imaginary part that is equal to the *flutter frequency* for the first signs of flutter instability. This wind speed therefore represents a critical dynamic load on the bridge, the so-called *critical flutter speed*.

It should be mentioned how the recursive method used at first presents the need to determine the *natural frequencies* of the structural system. For a specific chosen mode of vibration, following the assumption of a wind speed and a first-attempt frequency similar to the natural frequency (zero-wind condition), the *reduced speed U_r* and *reduced frequencies K* are calculated. The method implemented in this thesis allowed direct modification of flutter derivatives by *interpolation* of literature data for a calculated reduced velocity. The flutter derivatives modify the stiffness and aerodynamic damping of the system within the matrix27 elements. Semi-automatic updating of the matrix27 matrices via the RMODIF function in the ANSYS *Command Prompt* allows implementing the damped modal analysis of the system and studying the imaginary and real part of the eigenvalue corresponding to the mode of



vibration under analysis. The relative error between the imaginary part of the calculated eigenvalue and the assumed frequency is evaluated. Below a small tolerance value, *convergence* is achieved, and the real part of the eigenvalue is recorded. The iterative procedure involves developing the calculation for increasing wind speeds from 0 to 120 m/s with speed steps of 10 m/s, repeating the process for all vibration modes of interest in the research. Near the *flutter condition*, i.e. when the real part of an eigenvalue becomes close to zero, the analysis was thickened by applying velocity steps up to 0.5 m/s. In particular, the analysis focused on the study of:

- LAT-SYM and LAT-ASYM modes;
- VERT-SYM and VERT-ASYM modes;
- TORS-SYM and TORS-ASYM modes.

A structural damping equal to $\xi = 0.5\%$ have been assumed for all the modes extracted. Particularly for torsional modes, for which it is well suited, which are of relevant importance for the study of *stiffness-driven flutter*. The incorporation of mechanical damping is based on the introduction of the α and β parameters of the Rayleigh damping matrix. These values were determined graphically by extracting the *circular frequencies* of the first 10 natural modes of vibration of the 1915Çanakkale Bridge. Given the damping ratio, the values of α and β represent the *intercept* and *slope* of the graphical interpolation line, respectively.

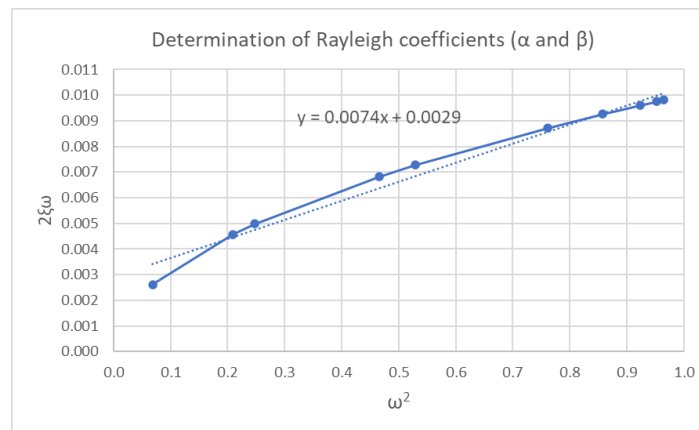


Figure 5-15: Rayleigh coefficients ($\alpha = 0.0029$; $\beta = 0.0074$ for $\xi = 0.5\%$)

Matrix27-1915ÇANAKKALE BRIDGE - FISH-BONE deck model - $\alpha=0.0029$; $\beta=0.0074$; $\xi=0.5\%$												
air mass density	Wind velocity	Frequency	Circular freq.	Reduced Circular freq.	element length	Bridge deck width	multiplier parameter in K_{ae1}^E	multiplier parameter in C_{ae1}^E	Reduced velocity	Rayleigh coeff. (mechanical damping)	Rayleigh coeff. (mechanical damping)	
$\rho_a [kg/m^3]$	$U [m/s]$	$f [Hz]$	$w [rad/sec]$	$K [rad]$	$L_e [m]$	Base [m]	a	b	U_{red}	α	β	
1.248	10	0.1474	0.926	4.17	24.083	45.06	26171.72	28258.88	1.5056	0.0029	0.0074	
					Kae				Cae			
					*a				*b			
A1	A2				c15	0.00	0.00	0.0	c15	0.00	0.00	0.00
-0.0556	-0.0094					0.00	0.00	0.0	c14	0.00	0.00	0.00
A3	A4				c16	0.00	0.00	0.0	c16	0.00	0.00	0.00
-0.0388	0.0784					0.00	0.00	0.0		0.00	0.00	0.00
A5	A6				c27	0.35	9168.07	-9168.1	c27	-0.41	-11520.24	11588.08
0	0				c28	-33.92	-887778.81	887778.8	c28	-26.03	-735548.79	728979.23
H1	H2					0.00	0.00	0.0		0.00	0.00	0.00
-0.4077	-0.5777				c39	3.53	92447.37	-92447.4	c39	-2.50	-70734.89	71419.00
H3	H4				c40	-78.81	-2062670.84	2062670.8	c40	-19.11	-539919.02	524655.25
-0.7528	0.3503				c93	0.00	0.00	0.0	c93	0.00	0.00	0.00
H5	H6					0.00	0.00	0.0		0.00	0.00	0.00
0	0				c94	0.00	0.00	0.0	c94	0.00	0.00	0.00
P1	P2					0.00	0.00	0.0		0.00	0.00	0.00
0	0				c105	0.35	9168.07	-9168.1	c105	-0.41	-11520.24	11588.08
P3	P4				c106	-33.92	-887778.81	887778.8	c106	-26.03	-735548.79	728979.23
0	0					0.00	0.00	0.0		0.00	0.00	0.00
P5	P6				c117	3.53	92447.37	-92447.4	c117	-2.50	-70734.89	71419.00
0	0				c118	-78.81	-2062670.84	2062670.8	c118	-19.11	-539919.02	524655.25

Figure 5-16: Example of Matrix27 compiling for ANSYS flutter analysis



Figure 5-15 and Figure 5-16 above show the graphical determination of Rayleigh coefficients contributing to the damping of the system and the procedure used in Microsoft EXCEL for semi-automatic compilation of aeroelastic force matrices in ANSYS, respectively.

Figure 5-17 and Figure 5-18 show the results of the flutter analyses for the vibration modes considered. The flutter analysis conducted led to the determination of a *critical flutter wind speed* of 84.5 m/s and a *flutter frequency* of 0.0938 Hz under 0° wind angle of attack, *probably associated with the first torsional branch*. This critical velocity corresponds to approximately 300 km/h, a very high wind speed value (belonging to the V degree of the Saffir-Simpson hurricane scale), which has not occurred historically and is difficult to achieve along the Dardanelles Strait and in the Marmara Sea.

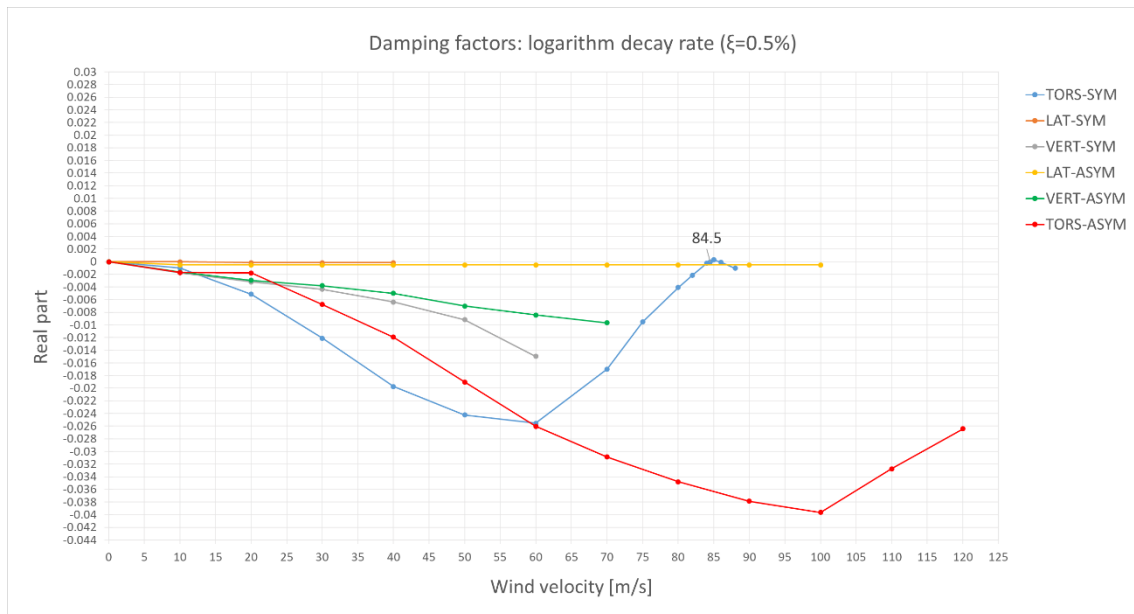


Figure 5-17: Variation of complex eigenvalues' Real part (damping factors) in ANSYS

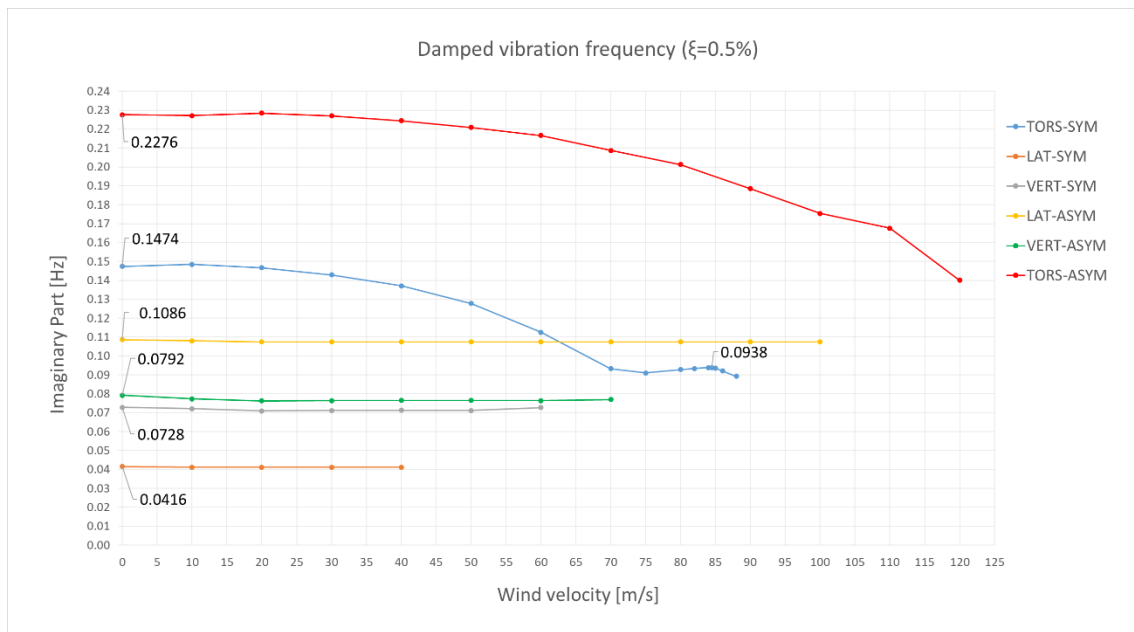


Figure 5-18: Variation of complex eigenvalues' Imaginary part (frequencies) in ANSYS



From the literature data provided in Section 5.1, it is evident that limiting to flutter derivatives under 0° angle of attack, the maximum value of reduced velocity that can be used for analysis is $U_r = 22$.

From Figure 5-17 and Figure 5-18, it is clear the range of analysis is distinct for each mode of vibration analyzed by virtue of the dependence of the reduced velocity on the wind speed U and frequency f .

As a result, graphs are obtained by *interpolation* of flutter derivatives in the experimental sampling interval of flutter derivatives.

Damping-driven flutter instability results only in appearance. In fact, contrary to what one might think by looking at graphs, the flutter phenomenon is not only activated by the torsional mode. As the wind speed increases, the modal shape changes along with the eigenvalues; in fact, the *interaction between vertical and torsional degrees of freedom* is what leads to flutter instability [59].

Flutter instability can be ascribed to the interaction between the first symmetric vertical (VERT-SYM) and torsional (TORS-SYM) modes: *extrapolation* of the flutter derivative data for reduced velocity of $U_r > 22$, i.e., beyond the sampling interval, allowed the interaction between the two vibration modes to be identified using ANSYS software. *A transfer of the instability in the vertical branch is seen as a particularly strong manifestation of the interaction.* The heaving mode branch flutter is physically consistent with the commonly observed torsional mode branch flutter, as discussed by X. Chen and A. Kareem [81]. However, in this instance, it results from a flutter derivative extrapolation procedure outside of its sampling interval, which may contain errors.

Figure 5-19 and Figure 5-20 show how the torsional branch's damping ratio starts growing at 60 m/s and becomes positive at *critical speed* of 78.8 m/s, after crossing the vertical branch's damping ratio, in correspondence to the heading of the pertinent modal frequencies. As the wind speed U increases, there is a growth of the vertical bending component, which progressively becomes comparable with the torsional one. The resulting flutter mode is flexural-torsional, as is usual for the *coupled-mode, stiffness-driven flutter instability*.

For sustained wind speeds close to 90 m/s, an increasing similarity between the torsional and vertical symmetrical modal components (TORS-SYM and VERT-SYM) is observed. In fact, these modal shapes and their associated frequencies, initially different, manifest a progressive approximation and a subsequent *frequency matching* with an effective *merging of the modal shapes* for high wind speeds.

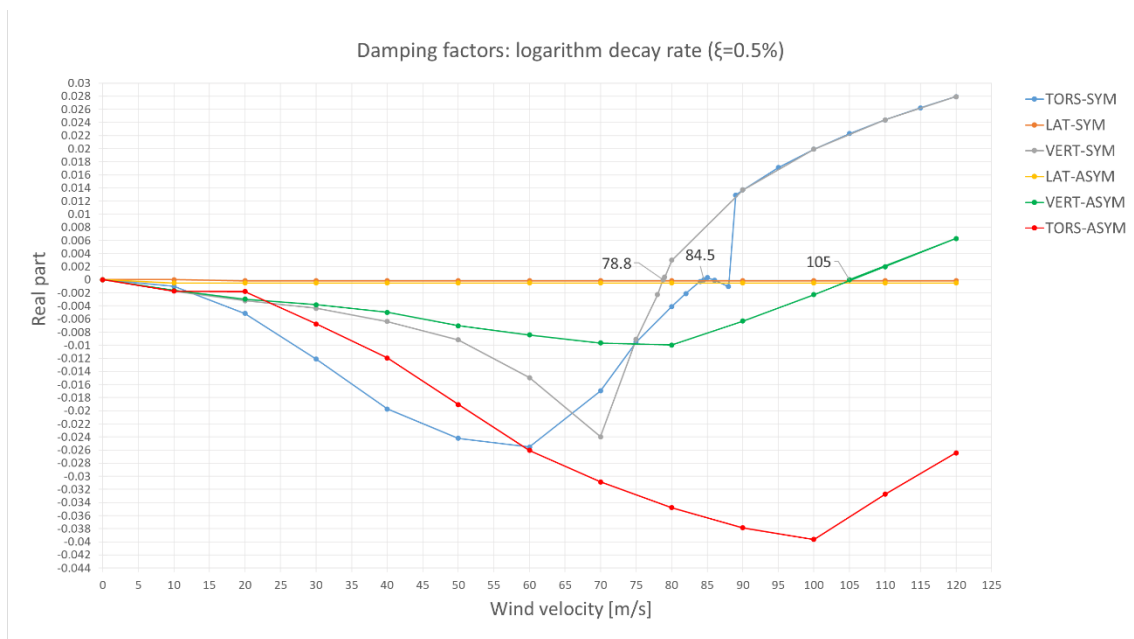


Figure 5-19: Variation of complex eigenvalues' Real part in ANSYS (extrapolation)

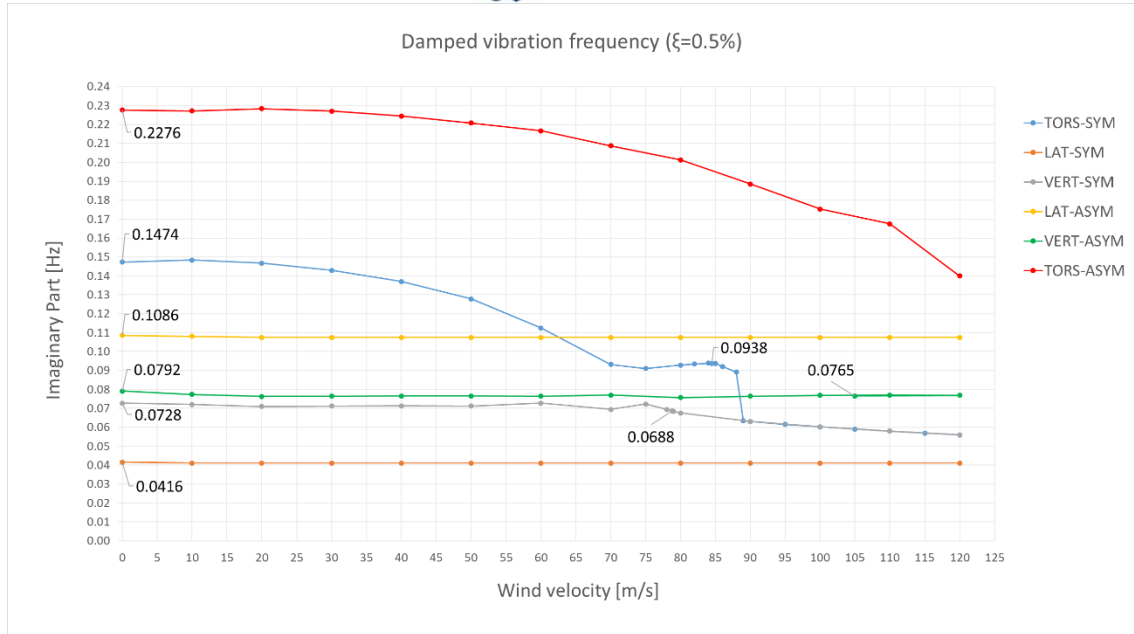


Figure 5-20: Variation of complex eigenvalues' Imaginary part in ANSYS (extrapolation)

A two-degree of freedom flutter is considered, which includes only *lift* and *moment aeroelastic forces*, while *drag forces* are not included at all. Only the flutter derivatives found in the literature studies were considered, which include only the flutter derivatives A_i^* and H_i^* whereas P_i^* do not appear and in fact are considered null in this thesis work. This did not allow to study a *possible influence of the lateral flutter derivatives* and any effects on the bridge flutter phenomenon.

In addition, the behavior of the system was studied for the two modal forms most relevant to the flutter phenomenon as the mechanical damping characteristics introduced in ANSYS were varied. Specifically, the structural mechanical damping was varied from 0 to 0.5% with steps of 0.1% (Figure 5-21). Under *flutter condition*, it is evident that the attainment of critical velocities for both modal forms is weakly dependent on the damping itself, highlighting how the flutter phenomenon is therefore not driven by damping, typical of one-degree of freedom flutter, but is instead *stiffness-driven*, confirming the point made above.

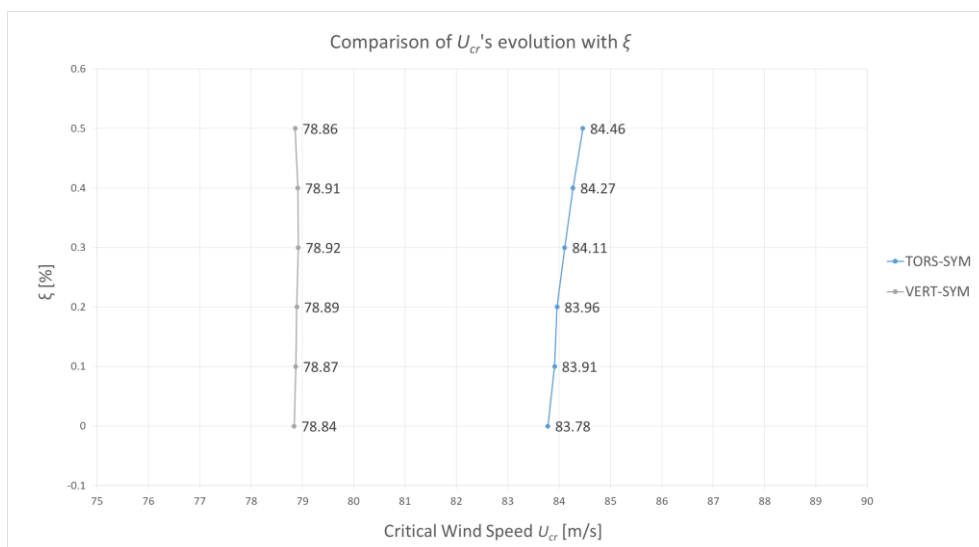


Figure 5-21: Study of the dependence of critical speed on mechanical damping ξ



In Figure 5-22, a confirmatory graphical analysis on the *evolution of torsional modal deformation as wind speed increases* is shown. Starting from the zero-wind condition (1), a modal shape is shown to be *pure torsional* (TORS-SYM) and unaffected by vertical components. As the wind speed increases, particularly at 60 m/s (2), there is an *initial interaction* between the torsional symmetrical mode and the vertical symmetrical mode. The flutter condition (3) and the analyzed maximum wind speed condition (4) are depicted next. In these cases, a gradual increase in the vertical component is shown, until they are comparable, and *matching* is observed: in fact, *modal shapes merge* and can no longer be distinguished, as seen in Figure 5-19.

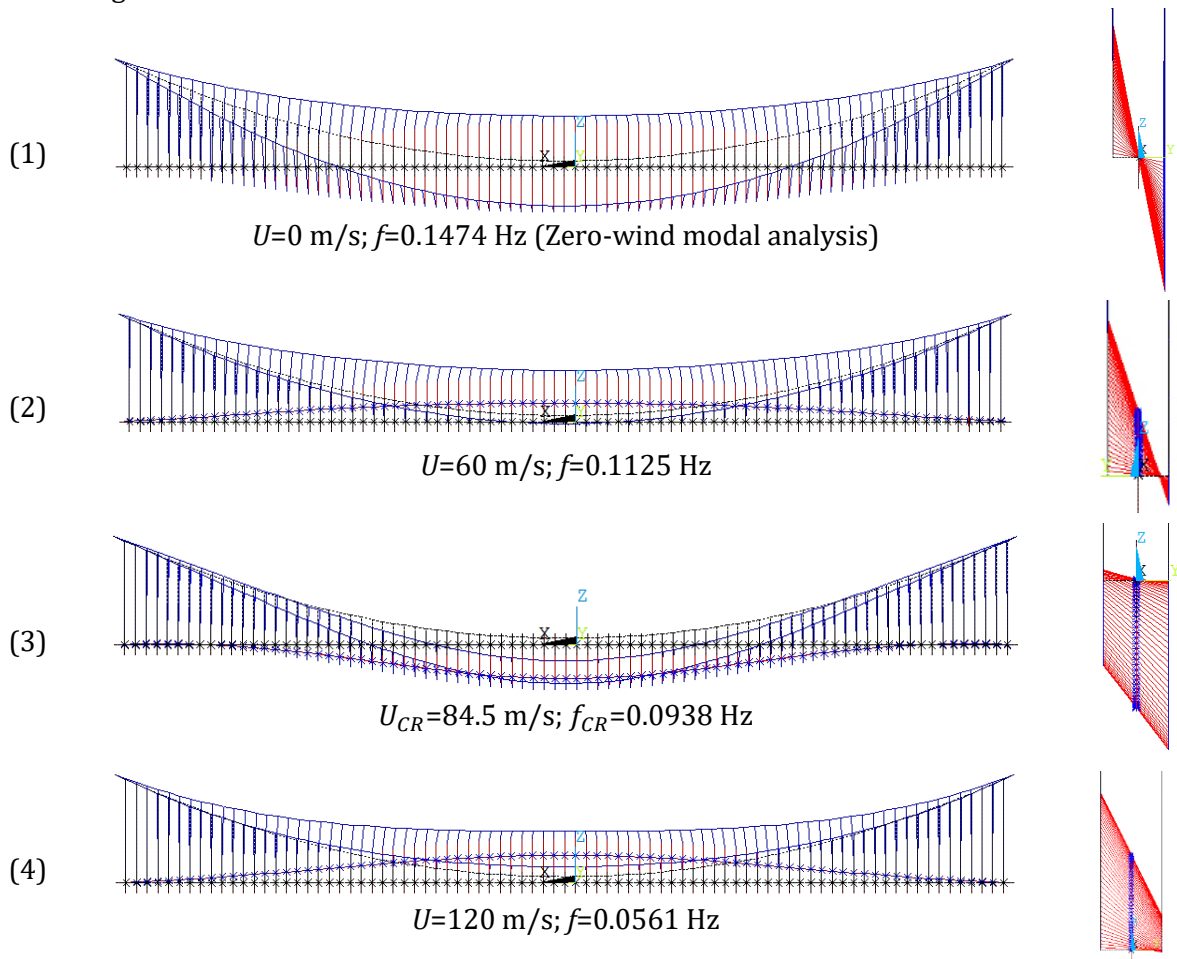


Figure 5-22: Evolution of torsional modal shape as a function of wind speed (ANSYS)



5.3.2 Analytical flutter assessment in MATLAB

Using MATLAB software, it was possible to address the analysis under flutter conditions, i.e., under the condition of the presence of critical dynamic wind-structure interaction effects in a range of investigation between 0 and 100 m/s. Figure 5-23 shows graphs concerning the damped modal analysis with the study of complex eigenvalues. Also, with the analysis in MATLAB, the flutter phenomenon could be evidenced: a *critical speed* of 84 m/s was obtained with a critical frequency of 0.0911 Hz under 0° wind angle of attack. As in the analyses performed in ANSYS, a "closeness" of the torsional and vertically symmetrical modes (mode 1 and 3, respectively) can also be seen in graphs below with a *first interaction in a speed range of 60 to 70 m/s*: Indeed, it is possible to see a phenomenon of *crossing* of the real parts of modes 1 and 3 and a phenomenon of *veering* [81] of their imaginary parts (frequencies) in the same velocity range. These phenomena characterize a *strong interaction* between the two modes, TORS-SYM and VERT-SYM.

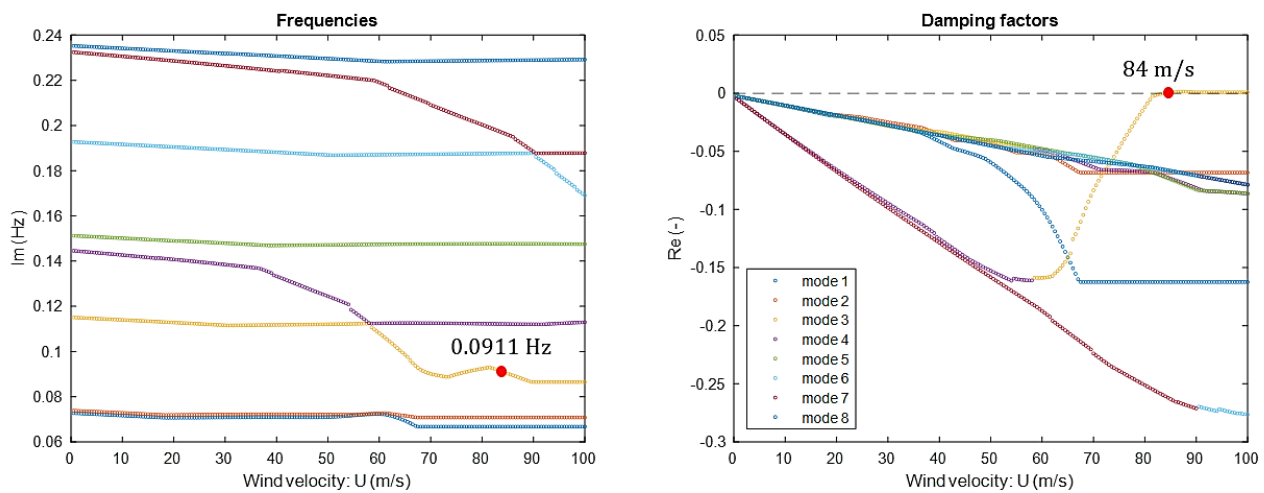


Figure 5-23: Variation of complex eigenvalues' Imaginary and Real part in MATLAB

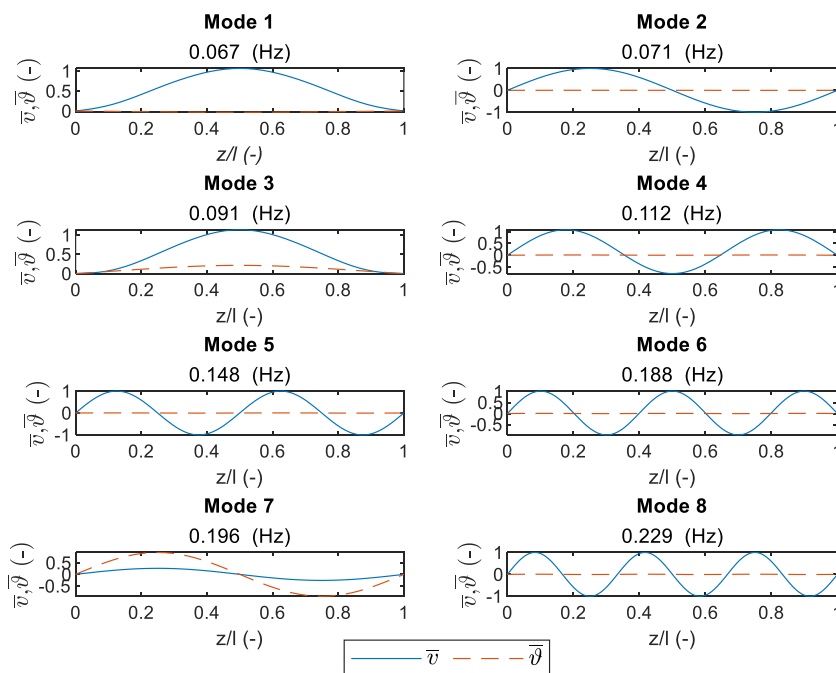


Figure 5-24: 1915Çanakkale Bridge's modal shapes in critical flutter condition (MATLAB)



It can be seen in Figure 5-24 that mode 3 and mode 7, which are representative of the *torsional symmetrical mode* (TORS-SYM) and the *torsional asymmetrical mode* (TORS-ASYM), respectively, presented themselves with different characteristics than the other modes shown in the figure.

For both modal shapes, vertical and torsional components are present to a greater or lesser extent, confirming the existence of the flexural-torsional interaction, which is typical of the *stiffness-driven flutter* [59]. In Figure 5-25, the torsional symmetrical mode (TORS-SYM) is studied individually for the zero-wind condition, with the natural frequency of the system, and for the critical flutter condition. In the former case, the presence of *pure torsion* is noted, while in the latter case the *coupling* between the vertical and torsional modal component results, analogous to what is expressed by Figure 5-22.

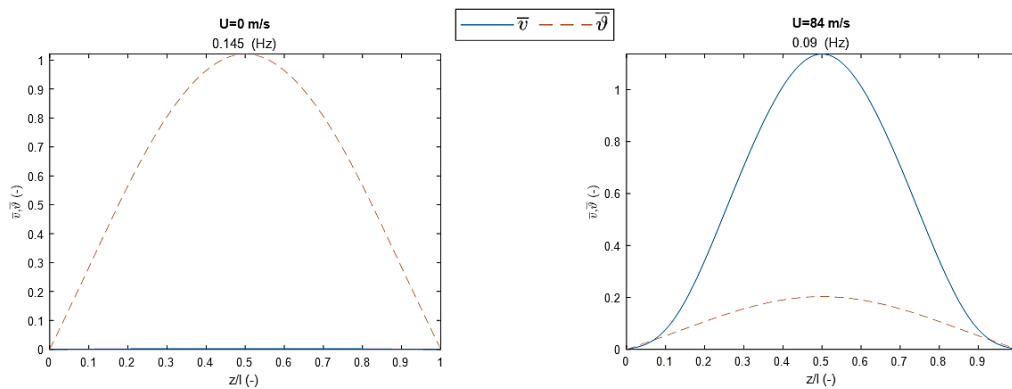


Figure 5-25: Torsional modal shape in zero-wind and critical flutter conditions (MATLAB)



5.3.3 Simplified analysis of 1-dof flutter

The analysis method reported in this section concerns a simplified solution of reducing a multi-degree-of-freedom system into a one-degree-of-freedom system. For this reason, it is often named as *single-mode criterion*. As anticipated in Chapter 2, Equation 2-26 can be solved efficiently using specialized numerical techniques, such as the *pK-F method* created by A. Namini and P. Albrecht [51].

Also demonstrated in the discussion by A. Carpinteri [45], the one-degree-of-freedom flutter method expressed by Equations 2-20 and 2-21 can also be used in the finite element framework.

The *uncoupled single-degree-of-freedom flutter* can be analyzed as follows, by pre and post multiplying Equation 2-26 by the eigenvector $\{\delta_{0,j}\}$ related to the j^{th} mode:

$$\{\delta_{0,j}\}^T \left(-\omega^2 [M] + i\omega \left([C] - \frac{1}{2} \rho U [C^*] \right) + [K] - \frac{1}{2} \rho U^2 [K^*] \right) \{\delta_{0,j}\} = \{0\} \quad (5-5)$$

Which, ignoring the cross-coupling aerodynamic terms, reduces to the following uncoupled equation for mode j to a scalar equation:

$$-\omega^2 m_j + i\omega \left(c_j - \frac{1}{2} \rho U c_j^* \right) + k_j - \frac{1}{2} \rho U^2 k_j^* = 0 \quad (5-6)$$

Equalizing the total damping to zero gives the *critical couple* for the j^{th} mode:

$$U_{F,j} = \frac{2c_j}{\rho c_j^*}; \quad \omega_{F,j}^2 = \frac{k_j - \frac{1}{2} \rho U_{F,j}^2 k_j^*}{m_j} \quad (5-7)$$

The *zero-damping condition* expressed by Equation 5-7 (a) can also be written as in R. H. Scanlan [77], R. H. Scanlan-N. P. Jones [82] and A. Namini-P. Albrecht treatments [51]:

$$H_1^*(\bar{K}) G_{hj} + P_1^*(\bar{K}) G_{pj} + A_2^*(\bar{K}) G_{\alpha j} \geq \frac{4\xi_j I_j \omega_j}{\rho B^4 L_d \bar{\omega}_j} \quad (5-8)$$

Equation 5-8 allows comparison between *mechanical damping* and *aeroelastic damping*. Where:

$$\bar{\omega}_j = \omega_j \left[\frac{1}{1 + \frac{\rho B^4}{2I_i} A_3^*(\bar{K}) G_{\alpha j}} \right]^{1/2} \quad (5-9)$$

And

$$\bar{K}_j = \frac{B \bar{\omega}_j}{U} \quad (5-10)$$

To solve Equation 5-8, it is necessary to define the following terms:

$$G_{hj} = \{u_z\}_j^T \{u_z\}_j \quad (5-11)$$

$$G_{pj} = \{u_y\}_j^T \{u_y\}_j \quad (5-12)$$

$$G_{\alpha j} = \{\vartheta_x\}_j^T \{\vartheta_x\}_j \quad (5-13)$$



Variables G_{hj} , G_{pj} and $G_{\alpha j}$ are the vectorial form of the *modal integrals* [82] in the *heave, sway and torsional directions*. u_z , u_y and ϑ_x are the deck's vertical and the transversal deflections, and the rotation around longitudinal axis of the bridge's deck, respectively. Moreover, ξ_j is the generalized damping ratio, L_d is the deck length and I_j is the generalized inertia, defined as:

$$I_j = \{\delta\}_j^T [M] \{\delta\}_j \quad (5-14)$$

Where:

- $\{\delta\}_j$ is a vector containing all the degree of freedom of the whole bridge.
- $[M]$ is the *mass matrix* of the bridge [83];

G_{hj} , G_{pj} , $G_{\alpha j}$, $\{\delta\}_j$ and $[M]$ are extracted by appropriate procedures from numerical model in the ANSYS software. A MATLAB code was implemented to provide a *graphical solution* for each mode considered, specifically the lateral symmetrical (LAT-SYM), vertical symmetrical (VERT-SYM) and torsional symmetrical (TORS-SYM) relative to a *single half-wave in the modal shape* and thus *fundamental modes* of the bridge structure. Thus, the *single-mode criterion* is studied graphically to understand its significance in terms of structural response.

Such analysis exploits the graphical comparison of the variation of aeroelastic damping with the mechanical damping of the system. *Single-mode flutter occurs at the lowest velocity where the aeroelastic damping term exceeds the value of mechanical damping.*

Figure 5-26 shows an example result of this type of analysis: one of the most significant collapses in modern structural engineering, the *1940 collapse of the Tacoma Narrows Bridge*, is presented.

It is a famous case of single-degree-of-freedom flutter instability occurred in relation to *the asymmetric torsional mode* (TORS-ASYM) and directly dependent on the flutter derivative A_2^* .

Torsional instability occurs at a wind speed between 10 and 11 m/s with a frequency close to 0.21 Hz at the time when the *aeroelastic damping branch overrides the mechanical damping value of the system*.

The *total damping then becomes negative* and causes torsional oscillation on the bridge deck progressively causing oscillatory divergence until structural collapse [43].

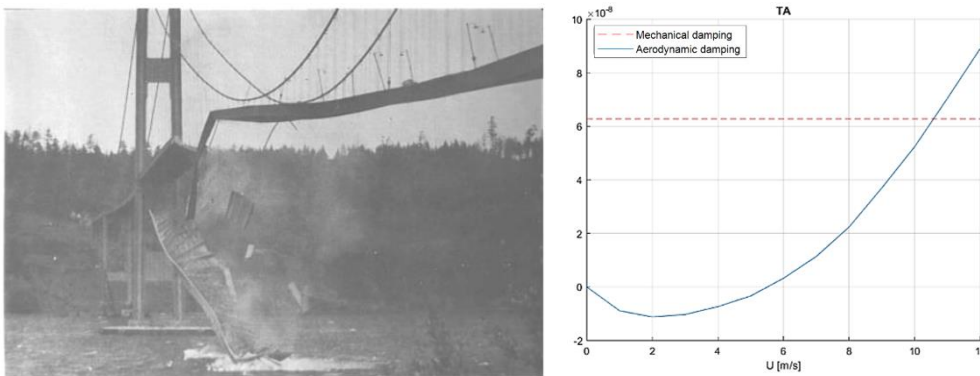


Figure 5-26: Tacoma Narrows bridge one-DOF flutter collapse [43]

This criterion was applied to the *1915Çanakkale Bridge* as part of this thesis. The graphs in Figure 5-27 show the results of the single-mode criterion on the analyzed modes, such as torsional symmetrical (TORS-SYM), vertical symmetrical (VERT-SYM) and lateral symmetrical (LAT-SYM) associated with the *fundamental* torsional, vertical bending and sway modal shapes, respectively.

From the observations held on the flutter derivatives H_1^* and A_2^* (P_1^* not present) shown in Figure 5-2, Figure 5-4 and Figure 5-5, it is evident that flutter derivatives functions remain *negative* for any value of

reduced velocity U_r . Consequently, it can be expected that the calculation criterion adopted does not identify unstable situations for one-DOF flutter.

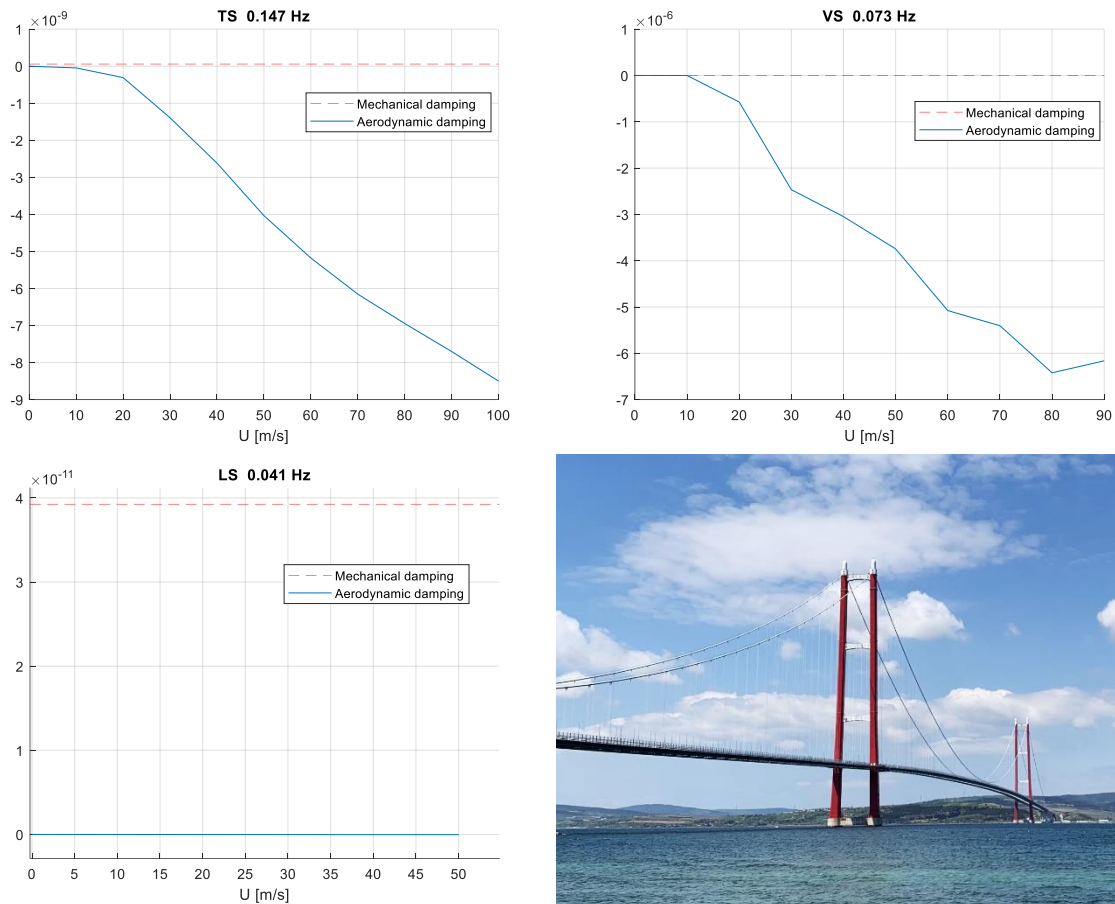


Figure 5-27: 1915Çanakkale Bridge single-DOF flutter analysis

The single-mode criterion applied to the case of the Dardanelles Strait bridge does not produce any critical wind speed because the flutter derivatives never become positive and therefore the mechanical damping, in this simplified model, is always greater than the *uncoupled aeroelastic damping* described by H_1^* , A_2^* and P_1^* flutter derivatives.

The analysis does not lead to the result of instability, but, on the contrary, the aeroelastic damping contributes positively on the total damping of the structural system.

The aerofoil twin-box section's shape, which is like an aircraft wing, gives the structure an exceptional level of stability against one-DOF flutter while favoring the appearance of aeroelastic instability phenomena when two or more modes of the structure's vibration are involved, known as *stiffness-driven flutter*. In fact, this specific type of aerodynamic deck, which cuts through the airflow, exhibits all-negative values of flutter derivatives for every reduced velocity studied of this phenomenon, also known as *damping-driven flutter*. The latter can be considered as a peculiar characteristic of this type of deck designed to resemble airfoils.



5.4 Summary comparison of results

In this final section of Chapter 5, it is necessary to summarize what has been confirmed by the analyses performed on the commercial software ANSYS and MATLAB regarding the *zero-wind modal analyses*, which are necessary for the calibration of the models used, the *flutter analyses* for the determination of the critical wind speed and corresponding flutter frequency, and the *single-mode criterion analysis*.

Zero-wind modal analysis results

Summary values are given in the Table 5-6 with respect to *zero-wind modal analysis*. The natural frequency values are compared with ANSYS values (Table 5-3 and Table 5-4) and reference values, i.e., the frequency data provided by the Liao-Wang study [78] shown in Table 5-2. The calculation of relative variances is referred to *MATLAB values* and the comparison is limited to the first *ten modes of vibration of the structure*, excluding local modes.

Mode	ANSYS Fish-bone freq. [Hz]	ANSYS Two-axis freq. [Hz]	Liao-Wang freq. [Hz]	MATLAB freq. [Hz]	Δ Fish-bone [%]	Δ Two-axis [%]	Δ Liao-Wang [%]	Mode type
1	0.0416	0.0489	0.0456	-	-	-	-	LAT-SYM
2	0.0728	0.0698	0.0724	0.0732	-0.55%	-4.64%	-1.09%	VERT-SYM
3	0.0792	0.0782	0.0823	0.0741	+6.88%	+5.53%	+11.07%	VERT-ASYM
4	0.1086	0.1002	0.1004	-	-	-	-	LAT-ASYM
5	0.1157	0.1141	0.1120	0.1151	+0.52%	-0.87%	-2.69%	VERT-SYM-II
6	0.1474	0.1477	0.1472	0.1453	+1.45%	+1.65%	+1.31%	TORS-SYM
8	0.1529	0.1521	-	0.1509	+1.33%	+0.80%	-	VERT-ASYM-II
12	0.1943	0.1927	-	0.1932	+0.57%	-0.26%	-	VERT-SYM-III
15	0.2276	0.2284	-	0.2324	-2.07%	-1.72%	-	TORS-ASYM
16	0.2367	0.2349	-	0.2351	+0.68%	-0.09%	-	VERT-ASYM-III

Table 5-6: Modal frequencies and modal shape comparison in zero-wind condition
(Percentage relative variances are calculated with respect to MATLAB values)

Flutter analysis results

Table 5-7 summarizes the result of the flutter analysis performed with both software used. Specifically, the relative variances on the flutter critical velocities U_{CR} are referred to the value identified in MATLAB. The comparison is made with literature data from *Chinese* [78] and *Danish* [64] research studies.

Method	U_{CR} [m/s]	U_{CR} [km/h]	f_{CR} [Hz]	$\% \Delta U_{CR-MATLAB}$
ANSYS	84.5	304.2	0.0938	+0.60%
MATLAB	84	302.4	0.0911	-
Rønne-Larsen	88	316.8	-	+4.76%
Liao-Wang	83	298.8	0.110	-1.19%

Table 5-7: Flutter analysis result comparison
(Percentage relative variances are calculated with respect to MATLAB values)

As shown in the flutter analyses developed in ANSYS, in the case of *extrapolation* of flutter derivatives beyond the experimental sampling interval, a flutter velocity of 78.8 m/s associated with a *vertical modal branch* was identified.

Single-mode criterion results

The single-mode criterion applied to the case of the 1915Çanakkale Bridge *does not produce any critical wind speed* because the flutter derivatives never become positive and therefore the mechanical damping, in this simplified model, is always greater than the aeroelastic damping.

CHAPTER 6 Conclusions

The process of designing and building the world record main span suspension bridge, the *1915Çanakkale Bridge*, involved countless analyses regarding the aerodynamic interaction between the bridge and the wind. The flutter phenomenon on the fully realized structure, studied in this thesis work, and wind-induced instability phenomena related to the construction phases, such as the positioning of the deck segments, the main cable and the hangers, were a complicated hurdle to overcome.

In particular, the aerodynamic stability verification analysis of the bridge was used to analyze specific critical situations in which uncontrolled oscillations of the bridge can lead to the catastrophic structural collapse of the suspension bridge.

Following several studies and design models of the Messina Strait Bridge [43], Turkey embarked on the design and construction of the 1915Çanakkale Bridge (2018-2022), mainly following the European design philosophy of suspension bridges, where large spans are bridged using aerodynamic deck shapes, similar to aircraft wings, and exploiting the twin-box deck air-gap, which improves stability and locally reduces turbulence. The 1915Çanakkale Bridge has been analyzed in this thesis using both numerical and analytical approaches, with particular emphasis on the problem of aeroelastic instability. The data obtained at the *IABSE Symposium Istanbul 2023* and identified in literature research studies allowed an accurate modelling of the bridge, focusing mainly on the study of the main span using *fish-bone* and *two-axis deck models*. The models were developed using the commercial software ANSYS, which allowed the effect of stiffening cables, mechanical damping and aerodynamic forces to be taken into account. Initially, a *zero-wind modal analysis* was performed on both models and the SDC software was used to study the torsional and flexural stiffness of the deck. The need to determine some design parameters that would allow *fitting of natural frequencies* and the use of a main span model instead of the full model, led to the use of an *iterative process of calibration*. For each model studied, the natural frequencies achieved were compared with the results from other studies and the fish-bone model was then selected to be tested with aerodynamic forces as the relative variance found in the natural frequencies was lower than the results obtained with the second model, especially in torsional (TORS-SYM) and vertical bending (VERT-SYM) mode. The adaptation of the model for flutter analysis involved the introduction of specific user-defined elements, called Matrix27, which allowed the modelling of the aerodynamic forces within the software-defined *stiffness* and *damping aeroelastic matrices* through the introduction of *flutter derivatives*. Following the studies proposed by Hua and Chen [52], the flutter analysis was carried out as a modal damped analysis in the presence of wind in an iterative form. The analysis was developed on the vibration modes of interest of the structure, ultimately obtaining the *critical flutter wind speed* and *flutter frequency*, i.e. the *critical flutter couple* that leads to structural collapse of the bridge. Then, using a MATLAB code [59] that was programmed to include aerostatic non-linearities, such as stiffening brought on by lift forces and Prandtl's second-order effects brought on by drag forces, the flutter analysis was carried out using a *semi-analytical approach*.

The outcomes of both analyses were compared with those of the research groups under consideration at the conclusion of the analyses in Chapter 5. The table below is also reported as Table 5-7 in Section 5.4 and expresses the results of flutter analysis with reference to the analytical *MATLAB values*.

<i>Method</i>	<i>U_{CR} [m/s]</i>	<i>U_{CR} [km/h]</i>	<i>f_{CR} [Hz]</i>	<i>$\% \Delta U_{CR-MATLAB}$</i>
ANSYS	84.5	304.2	0.0938	+0.60%
MATLAB	84	302.4	0.0911	-
Rønne-Larsen	88	316.8	-	+4.76%
Liao-Wang	83	298.8	0.110	-1.19%

(Percentage relative variances are calculated with respect to MATLAB values)



With reference to the table above, it is clear that both methods used produced accurate results in terms of flutter velocity, in line with the Danish results obtained by *Rønne* and *Larsen* at COWI [64] and the Chinese research study conducted by *Liao* and *Wang* [78]. Different approaches, numerical and analytical, showed a relative difference on flutter velocity of less than 5% compared to literature data. The model implemented on ANSYS software and the analytical approach on MATLAB made it possible to correctly study the torsional and vertical bending components of the flutter, showing coupled behavior of the flutter from velocities close to 60 m/s. *The relative percentage variance between the numerical and the analytical approach was less than 1%, which makes it clear that the analytical method is very valid*, involving a much more simplified model and thus a reduced calculation time. The presence of two-degree-of-freedom flutter prompted the analysis of the critical flutter velocity as the damping ratio varies, showing little dependence on mechanical damping and a consequent situation of *stiffness-driven flutter*. With the study of the variation of the torsional modal deformation as the wind speed increases, the influence of the vertical component on the torsional one during the two-degree-of-freedom flutter instability phenomenon was understood. The two modal components become comparable, resulting in a critical mode of coupled vertical and torsional flutter.

A further calculation approach is proposed in the final part of Chapter 5. This is the simplified 1-degree-of-freedom flutter analysis, also known as the single-mode criterion, originally proposed by Scanlan [77] and later extended by *A. Namini* and *P. Albrecht* [51] to a finite element framework. This approach, based on matrices and eigenvectors extracted from ANSYS APDL and implemented on MATLAB, allowed the specific nature of the bridge deck to be revealed. The analysis does not lead to the result of instability, but on the contrary the aeroelastic damping contributes positively on the structural system.

The aerofoil twin-box section's shape, which is like an aircraft wing, gives the structure an exceptional level of stability against one-degree-of-freedom flutter while favoring the appearance of aeroelastic instability phenomena when two or more modes of the structure's vibration are involved.

In fact, this specific type of deck, which cuts through the airflow "like a blade", exhibits values of flutter derivatives of this phenomenon, also known as damping-driven flutter, all of which are negative for every reduced velocity studied, which is a peculiar characteristic of this type of deck designed to resemble airfoils.

When compared to the long-span bridges of the latter half of the 20th century, the analysis performed using this method demonstrated this advancement in technology and design.

In conclusion, it was found that the numerical and analytical methods used confirm the efficient behavior of the 1915Çanakkale Bridge towards the critical flutter phenomenon. This phenomenon could occur for very high wind speeds, comparable to high class hurricanes, but hardly found along the Dardanelles Strait and in the Sea of Marmara.

The perfect combination of design and construction of this important structure laid the foundation for subsequent innovation and research in the field of long-span suspension bridges.



References

- [1] "Close-up Engineering - Daily building magazine," March 2023. [Online]. Available: <https://buildingcue.it/ponti-sospesi-come-studiarli/36937/>. [Accessed July 2023].
- [2] "Tecnolab-percorsi di didattica laboratoriale," [Online]. Available: <http://tecnolab2011.blogspot.com/p/strutture.html>. [Accessed June 2023].
- [3] Università degli studi di Napoli Federico II, "Problematiche aeroelastiche dei ponti di grande luce: stall flutter," [Online]. Available: <https://www.docenti.unina.it/webdocenti-be/allegati/materiale-didattico/400921>. [Accessed July 2023].
- [4] L. G. Guidi, *Long span bridges: the evolution of deck stiffened system and the case study on the seismic behaviour of a mailart-arch-type bridge: Viadotto Olivieri (SA) [PhD thesis]*, Napoli: Università degli studi di Napoli Federico II, 2017.
- [5] A. Carpinteri, *Didactic support materials for the course of "Static and Dynamic Instability of Structures" - Lecture 8 - Dynamic Instability with follower non conservative loads*, Torino: Politecnico di Torino, 2021.
- [6] National Museum of the American Indian - Education Office, "Q'eshwachaka - A living legacy of Inka Engineering," 2015. [Online]. Available: <https://americanindian.si.edu/nk360/inka/pdf/Inka-poster.pdf>. [Accessed September 2023].
- [7] Japan Guide, "Kazurabashi Bridge," [Online]. Available: <https://www.japan-guide.com/e/e7828.html>. [Accessed August 2023].
- [8] J. Finley, "Finley's Chain Bridge," *The Port Folio*, vol. III, no. 6, p. 441, 1810.
- [9] D. Denenberg, "Bridgemeister," [Online]. Available: <https://www.bridgemeister.com/pic.php?pid=1612>. [Accessed September 2023].
- [10] "Structurae - International Database and Gallery of Structures," February 2016. [Online]. Available: <https://structurae.net/en/structures/dryburgh-abbey-bridge-1872>. [Accessed July 2023].
- [11] "Show Me Wales - Cymru," [Online]. Available: <https://www.visitmidwales.co.uk/showmewales/information/product-catch-all/menai-bridge-p1730131>. [Accessed August 2023].
- [12] "Britannica - Menai Bridge," The Editors of Encyclopaedia, 20 May 2021. [Online]. Available: <https://www.britannica.com/topic/Menai-Bridge>. [Accessed August 2023].
- [13] "Napoli Turistica - Arte e Cultura," 15 October 2020. [Online]. Available: <https://www.napoli-turistica.com/ponte-real-ferdinando-sul-garigliano/>. [Accessed July 2023].
- [14] "Pontelandolfo News," 10 July 2019. [Online]. Available: <https://www.pontelandolfonews.com/cultura/il-ponte-real-ferdinando/>. [Accessed September 2023].
- [15] "Network Rail - Media centre," [Online]. Available: <https://www.networkrailmediacentre.co.uk/news/rail-improvement-for-britannia-bridge>. [Accessed August 2023].
- [16] F. Griggs, "Structure Magazine," *Structure*, June 2016. [Online]. Available: <https://www.structuremag.org/?p=9982>. [Accessed July 2023].



- [17] "Alchetron," [Online]. Available: <https://alchetron.com/Niagara-Falls-Suspension-Bridge#niagara-falls-suspension-bridge-7119cf12-4b59-4dd6-8079-ed68da68de9-resize-750.jpeg>. [Accessed July 2023].
- [18] F. Griggs, "Structure Magazine," May 2016. [Online]. Available: <https://www.structuremag.org/?p=9865>. [Accessed September 2023].
- [19] "New York City Department of Transportation," [Online]. Available: <https://www.nyc.gov/html/dot/html/infrastructure/brooklyn-bridge.shtml>. [Accessed July 2023].
- [20] J. Melan, *Theory of Arches and Suspension Bridges*, vol. 2, Myron Clark, London: Myron Clark Publ. Comp. London, 1913.
- [21] F. Gazzola and G. Sperone, "Thresholds for hanger slackening and cable shortening in the Melan equation for suspension bridges," *Nonlinear Analysis: Real World Applications*, vol. 39, pp. 520-536, 2018.
- [22] "The BoweryBoys," March 2018. [Online]. Available: <https://www.boweryboyshistory.com/2018/03/crossing-brooklyn-williamsburg-bridge-changed-new-york-city.html>. [Accessed July 2023].
- [23] F. Griggs, "Structure Magazine," April 2013. [Online]. Available: <https://www.structuremag.org/?p=736>. [Accessed July 2023].
- [24] "Britannica - Ammann," The Editors of Encyclopaedia, March 2023. [Online]. Available: <https://www.britannica.com/biography/Othmar-Herman-Ammann>. [Accessed August 2023].
- [25] D. Franklin, "AAA.com - Best Views of the Golden Gate Bridge," 16 May 2019. [Online]. Available: <https://mwg.aaa.com/via/places-visit/best-views-golden-gate-bridge>. [Accessed July 2023].
- [26] "Altervista - San Francisco - Golden Gate Bridge," [Online]. Available: <https://sf94101.altervista.org/golden-gate-bridge/>. [Accessed August 2023].
- [27] "MTA - Bronx-Whitestone Bridge," 10 July 2023. [Online]. Available: <https://new.mta.info/bridges-and-tunnels/about/bronx-whitestone-bridge>. [Accessed August 2023].
- [28] S. Chan, "The New York Times Archive - City Room," April 2009. [Online]. Available: <https://archive.nytimes.com/cityroom.blogs.nytimes.com/2009/04/29/70th-birthday-of-the-bronx-whitestone-bridge/>. [Accessed August 2023].
- [29] "Britannica - Tacoma Narrows Bridge," The Editors of Encyclopaedia, February 2021. [Online]. Available: <https://www.britannica.com/topic/Tacoma-Narrows-Bridge>. [Accessed July 2023].
- [30] "Britannica - Mackinac Bridge," The Editors of Encyclopaedia, March 2023. [Online]. Available: <https://www.britannica.com/topic/Mackinac-Bridge>. [Accessed August 2023].
- [31] N. Janberg, "Structurae - International Database and Galley of Structures," August 2019. [Online]. Available: <https://structurae.net/en/structures/verrazzano-narrows-bridge>. [Accessed July 2023].
- [32] "New Civil Engineer News," March 2016. [Online]. Available: <https://www.newcivilengineer.com/archive/severn-bridge-to-undergo-cable-inspections-08-03-2016/>. [Accessed July 2023].
- [33] "Advisor Travel," [Online]. Available: <https://en.advisor.travel/poi/Bosphorus-Bridge-4421>. [Accessed August 2023].



- [34] "Humber Bridge - Our History," [Online]. Available: <https://www.humberbridge.co.uk/our-history/>. [Accessed August 2023].
- [35] S. Kramarczik, "Structurae - International Database and Gallery of Structures," 29 June 2013. [Online]. Available: <https://structurae.net/en/structures/great-belt-east-bridge>. [Accessed July 2023].
- [36] "Structurae - International Database and Gallery of Structures," September 2021. [Online]. Available: <https://structurae.net/en/structures/jiangyin-yangtze-river-bridge>. [Accessed August 2023].
- [37] "Structurae - International Database and Gallery of Structures," December 2009. [Online]. Available: <https://structurae.net/en/structures/runyang-yangtze-river-south-bridge>. [Accessed August 2023].
- [38] J. Guo, C.-J. Hu, M.-J. Zhu and Y.-Q. Ni, "Monitoring-based evolution of dynamic characteristics of a long span suspension bridge under typhoons," *Journal of Civil Structural Health Monitoring*, vol. 11, no. 10, pp. 397-410, April 2021.
- [39] N. M. Apaydin and S. Bas, "Long-span Orthotropic Steel Deck Bridges of Turkey," *IOP Conference: Materials science and Engineering - 9th International Symposium on Steel Bridges*, vol. 419, September 2018.
- [40] "WeBuild - Northern Marmara Motorway and Yavuz Sultan Selim Bridge (Third Bosphorus Bridge)," [Online]. Available: <https://www.webuildgroup.com/en/projects/motorways-roads/northern-marmara-motorway-and-yavuz-sultan-selim-bridge-third-bosphorus-bridge/>. [Accessed August 2023].
- [41] "Cimtas - Signature Projects: Structural Steel," [Online]. Available: <https://www.cimtas.com/en/signature-projects/structural-steel-signature-projects/osmangazi-bridge/>. [Accessed August 2023].
- [42] "1915Canakkale.com," 2022. [Online]. Available: <https://www.1915canakkale.com/en-us/press-room/images>. [Accessed May 2023].
- [43] S. Huang, *Flutter analysis of long-span bridges: the case-study of Messina Strait Project [Master thesis]*, Torino: Politecnico di Torino, a.a. 2022/2023.
- [44] F. Di Agabito, *Flutter Analysis of suspension bridges in Ansys: the Akashi Kaikyo bridge case-study [Master thesis]*, Torino: Politecnico di Torino, a.a. 2017/2018.
- [45] A. Carpinteri, "Long-span structures: Dynamics and buckling," in *Advanced Structural Mechanics*, Boca Raton, FL, CRC Press Taylor & Francis Group, 2017, pp. 253-291.
- [46] G. Piana and A. Carpinteri, *Course of "Static and Dynamic Instability of Structures" - Practice lecture - Examples of calculation for suspension bridges (aeroelastic instability)*, Torino: Politecnico di Torino, 2022.
- [47] R. H. Scanlan and J. J. Tomko, "Airfoil and bridge deck flutter derivatives," *Journal of the Engineering Mechanics Division*, vol. 97, no. 6, pp. 1717-1737, 1971.
- [48] R. H. Scanlan, "Aerodynamics of cable-supported bridges," *Journal of Constructional Steel Research*, vol. 39, no. 1, pp. 51-68, 1996.
- [49] A. Carpinteri, "Buckling instability in slender, thin and shallow structures," in *Advanced Structural Mechanics*, Boca Raton, FL, CRC Press Taylor & Francis Group, 2017, pp. 231-233.
- [50] Sorbonne Université, "Dynamical analysis of the so-called Ziegler column," 2022.



- [51] A. Namini, P. Albrecht and H. Bosch, "Finite Element-Based Flutter Analysis of Cable-Suspended Bridges," *Journal of Structural Engineering*, vol. 118, no. 6, pp. 1509-1526, 1992.
- [52] X. G. Hua and Z. Q. Chen, "Full-order and multimode flutter analysis using ANSYS," *Finite Elements in Analysis and Design*, vol. 44, no. 1, pp. 537-551, June 2008.
- [53] X. G. Hua, Z. Q. Chen, Y. Q. Ni and J. M. Ko, "Flutter analysis of long-span bridges using ANSYS," *Wind and Structures*, vol. 10, no. 1, pp. 61-82, January 2007.
- [54] S. Russo, G. Piana, L. Patruno and A. Carpinteri, "Preliminary flutter stability assessment of the double-deck George Washington Bridge," *Applied Sciences*, vol. 13, no. 11, p. 6389, 2023.
- [55] S. Russo, *Fluid-dynamic and flutter analysis of the George Washington suspension bridge [Master thesis]*, Torino: Politecnico di Torino, 2019.
- [56] Y. J. Ge and H. Tanaka, "Aerodynamic flutter analysis of cable-supported bridges by multi-mode and full-mode approaches," *Journal of Wind Engineering and Industrial Aerodynamics*, vol. 86, no. 2-3, pp. 123-153, 2000.
- [57] G. Piana and A. Carpinteri, "Long-span suspension bridge flutter analysis with drag force effects," *Journal of Applied and Computational Mechanics*, vol. 7(SI), pp. 1077-1089, 2021.
- [58] S. Russo, G. Piana and A. Carpinteri, "Linear aeroelastic analysis of suspension bridges with second-order effects," in *2nd International Conference on Computations for Science and Engineering (ICCSE2)*, Rimini Riviera, Italy, August 30-September 2, 2022.
- [59] S. Russo, G. Piana and A. Carpinteri, "Multimodal aeroelastic analysis of suspension bridges with aerostatic nonlinearities," in *XII International Conference on Structural Dynamics (EURODYN 2023)*, Delft, the Netherlands, July 2-5, 2023.
- [60] *1900/1915 - L'impero ottomano alla vigilia della grande guerra*. [Film]. Italia: Rai Storia - webdoc.
- [61] M. Ascaso Til, A. Sancho Santamaria and N. L. Lopez, "1915Çanakkale Bridge, Turkey: challenges and achievements of deck erection over the Dardanelles," *Proceedings of the Institution of Civil Engineers - Bridge engineering*, pp. 1-17, 2022.
- [62] V.-D. Boteanu, J. W. Sørensen, J. Park, S. R. Bjærre and H. Polk, "The 1915 Çanakkale Bridge: Designing a twin-box girder suitable for a world record span," in *IABSE2023 Symposium-Long span bridges*, Istanbul, Turkey, April 26-28, 2023.
- [63] G. Bartoli, P. D'asdia, S. Febo, C. Mannini, S. Pastò and L. Procino, "Proposta di impalcati innovativi per ponti sospesi di grande luce," in *10° Convegno nazionale di Ingegneria del Vento*, Cefalù (PA), Italy, 2009.
- [64] M. Rønne, A. Larsen and J. H. Walther, "The nose-up effect in twin-box bridge deck flutter: Experimental observation and theoretical model," *Wind and Structures*, vol. 32, no. 8, pp. 293-308, 2021.
- [65] H. Choi, J. Pihl, Y. Yamasaki, B. Jeong and K. Lyu, "Steel Deck Fabrication and Erection of the 1915 Çanakkale Bridge," in *IABSE2023 Symposium-Long span bridges*, Istanbul, Turkey, April 26-28, 2023.
- [66] V.-D. Boteanu, J. S. Steenfelt, M. Schunk and B. Zhao, "Innovative geotechnical solutions to meet the demands of the 1915 Çanakkale bridge," in *IABSE2023 Symposium-Long span bridges*, Istanbul, Turkey, April 26-28, 2023.
- [67] T. Löhning, U. G. Ravn, F. Pedersen and L. W. M. Christoffersen, "The 1915 Çanakkale Bridge - Concept development for substructure," in *IABSE2023 Symposium-Long span bridges*, Istanbul, Turkey, April 26-28, 2023.



- [68] P. Morrison, L. H. Kaasa, J. Go and H. Kim, "1915 Çanakkale Bridge, Tower foundations: Independent Design Verification," in *IABSE2023 Symposium-Long span bridges*, Istanbul, Turkey, April 26-28, 2023.
- [69] L. H. Kaasa, R. Hornby and K. Aas-Jakobsen, "Independent Design Verification of the 1915 Çanakkale Bridge: Global Analyses of Construction Stages," in *IABSE2023 Symposium-Long span bridges*, Istanbul, Turkey, April 26-28, 2023.
- [70] S. Park, H. Paik, S. Choi, G. Hwang and J. Kwak, "The 1915 Çanakkale Bridge: Geometry and vibration controls for steel tower under construction," in *IABSE2023 Symposium-Long span bridges*, Istanbul, Turkey, April 26-28, 2023.
- [71] M. N. Apaydin, A. C. Zulfikar and O. Cetindemir, "Structural health monitoring systems of long-span bridges in Turkey and lessons learned from experienced extreme events," *Journal of Civil Structural Health Monitoring*, vol. 12, no. 6, pp. 1375-1412, 2022.
- [72] J. Pihl and H. Choi, "1915 Çanakkale Bridge - Cable Structures," in *IABSE2023 Symposium-Long span bridges*, Istanbul, Turkey, April 26-28, 2023.
- [73] J. Kim, H. Choi and Y. Yamasaki, "PPWS fabrication and erection of the 1915 Çanakkale," in *IABSE2023 Symposium-Long span bridges*, Istanbul, Turkey, April 26-28, 2023.
- [74] G. Li Destri Nicosia, A. Sbitnev, Y. Zhang and M. Schunk, "Geotechnical earthquake engineering for the detailed design of the 1915 Çanakkale bridge," in *IABSE2023 Symposium-Long span bridges*, Istanbul, Turkey, April 26-28, 2023.
- [75] M. Virlogeux, J.-F. Klein, T. Delémont, L. Gaudry and E. Bellanger, "Hybrid solution for the 1915 Çanakkale Bridge," in *IABSE2023 Symposium-Long span bridges*, Istanbul, Turkey, April 26-28, 2023.
- [76] Q. Wang, *private communication*, 2022.
- [77] R. H. Scanlan, "Interpreting Aeroelastic Models of Cable-Stayed Bridges," *Journal of Engineering Mechanics*, vol. 113, no. 4, 1987.
- [78] H. Liao, Q. Wang, J. Zhu, T. Ren and C. Shao, "Flutter instability of 1915 Çanakkale Bridge Considering Nonlinear Aero-static Effect," in *8th European-African Conference on Wind Engineering (EACWE2022)*, Bucharest, Romania, September 20-23, 2022.
- [79] A. Larsen, "Aerodynamic aspects of the final design of the 1624 m suspension bridge across the Great Belt," *Journal of Wind Engineering and Industrial Aerodynamics*, vol. 48, no. 3, pp. 261-285, 1993.
- [80] R. H. Scanlan and R. Rosenbaum, *Introduction to the Study of Aircraft Vibration and Flutter*, New York, USA: The MacMillan Company, 1962.
- [81] X. Chen and A. Kareem, "Curve Veering of Eigenvalue Loci of Bridges with Aeroelastic Effects," *Journal of Engineering Mechanics*, vol. 129, no. 2, pp. 146-159, 2003.
- [82] R. H. Scanlan and N. P. Jones, "Aeroelastic Analysis of Cable-stayed Bridges," *Journal of Structural Engineering*, vol. 116, no. 2, 1990.
- [83] A. Leon, *Análisis aeroelástico de puentes soportados por cables en el dominio [PhD thesis]*, La Coruña: Universidade da Coruña, 2009.
- [84] T. Miyata, K. Tada, H. Sato, H. Katsuchi and T. Hikami, "New findings of coupled-flutter in full model wind tunnel tests on the Akashi Kaikyo Bridge," in *Proceedings of the International Conference on Cable-Stayed and Suspension Bridges*, vol. 2, Deauville, 1994.